June 2022

COLLECTIVE MOTION AND PHASE DIAGRAM OF SELF-PROPELLED VIBRATED HARD SQUARES

Zhejun Shen
University of Massachusetts Amherst

COLLECTIVE MOTION AND PHASE DIAGRAM OF SELF-PROPELLED VIBRATED HARD SQUARES

A Dissertation Presented

by

ZHEJUN SHEN

Submitted to the Graduate School of the
University of Massachusetts Amherst in partial fulfillment
of the requirements for the degree of

DOCTOR OF PHILOSOPHY

May 2022

Physics

COLLECTIVE MOTION AND PHASE DIAGRAM OF SELF-PROPELLED VIBRATED HARD SQUARES

A Dissertation Presented

by

ZHEJUN SHEN

Approved as to style and content by:

Narayanan Menon, Chair

Jon Machta, Member

Gregory Grason, Member

Manasa Kandula, Member

Anthony Dinsmore, Department Head
Physics

ACKNOWLEDGMENTS

First of all, I am really grateful to my advisor Professor Menon and his wife Professor Tewari. It's a very great experience to work in the research group. I really learned a lot from you: how to initiate a question for an unknown problem, method to solve a complicated question, summarize the most important information from messy data and how to make a good and clear representation. These are not specific to physics research but are scientific ways to solve any problem I will meet in my life. Besides that, your personality set a role model for me. You are open minded, welcome any question and are willing to listen any different opinions. You never blame me for my mistake, give me the most freedom to do anything I like and encourage me to explore any new area I am interested in. For me, you are not only my advisor but also my friend. When I had a baby, I needed to take care of my family. You were very supportive at all time. My Ph.D program is a really precious experience. I am so glad that you are my advisor and I am very proud to be your student.

I want to have special thanks to my wife, Shuang Li. We have known each other for seven years. Before your graduation from New York University, we always lived in different cities. Our trust with each other made us go through the hard time and made us decide to get married in 2017 without hesitation. I really appreciate your contribution to the family. You gave up your opportunities and modern life in big cities and moved to Amherst to support me. Your cook food almost everyday even you are busy with your own job. Without you on my back, I can't go through the difficult job searching period. You support all my decisions and try your best to help me to achieve my goals. I am so lucky to have you as my wife and I am really happy to have our cute daughter Morgan with you.

I want to thank all my family members. Morgan, you bring so much happiness to my life. When you smile, I feel my heart melt. I hope you grow up healthily and happily, find your own interest and enjoy the beautiful world. I will try my best to support your dream. Dad and Mom, thanks for your love. Whenever I asked for anything, you always support me both spiritually and economically. Your give me the confidence to try anything I am interested. I am really happy and lucky to be your son. I feel sorry that I cannot stay with you in recent years. I hope both of you healthy and take good care of yourselves.

I am a lucky person surrounded by love. I love all of you.

ABSTRACT

COLLECTIVE MOTION AND PHASE DIAGRAM OF SELF-PROPELLED VIBRATED HARD SQUARES

MAY 2022

ZHEJUN SHEN

B.Sc., TONGJI UNIVERSITY

M.Sc., FUDAN UNIVERSITY

Ph.D., UNIVERSITY OF MASSACHUSETTS AMHERST

Directed by: Professor Narayanan Menon

In equilibrium, matter condenses into ordered phases due to the combined effects of inter-particle interactions and entropy. In this dissertation we explore self-propulsion of particles as an additional nonequilibrium consideration in the mechanisms for ordering. Our experiments employ square-shaped hard particles; in equilibrium, when particle motions are randomly directed, squares form entropically-stabilized phases in which first their orientations, and then their positions, get locked in relative to each other, depending on the density of coverage. When the square tiles are modified to have a small propulsion along some body-fixed axis we find that their tendency to order is profoundly altered. Adding such 'activity'(quantified by the persistence length of motion along the mobility direction) to particles can produce new 'phases' and mechanisms for ordering not seen in equilibrium materials.

In the first study, we study a system of vibrated self-propelled granular particles with high persistence length on a horizontal plane within a circular boundary. The

particles are square and designed to have polar motion along one body diagonal. When they hit the boundary they align along the boundary but also 'walk' along the boundary. Given a large enough initial density in the plane, particles spontaneously migrate to the boundary, form a ring and perform a stable 1D rotational gear-like motion with a direction chosen by their net polarization. For a fully polarized single ring we find that the collective velocity surpasses the free single-particle velocity. This collective velocity increases as the density of particles in the ring increases, which is counterintuitive for a normal traffic problem. The spatial correlations of particle velocity fluctuations decay exponentially with a length scale that increases with density. There is thus increased cooperativity in the system. However, the temporal correlation shows that velocity fluctuations are very short-lived.

In a second project, we study the effect of varying the persistence length of individual particle motion in an ensemble of squares held at fixed density. We find that adding activity to the particles qualitatively modifies their phase diagram relative to that of passive squares. At large enough activity (just as in the previous study), particles always migrate to the boundary and form a high-density ordered state. At smaller values of activity, different phases are seen as a function of density. At low density, the particles form an isotropic fluid. As the density increased, particles separate into a high-density ordered region while the remaining particles remain in the fluid state. Above a finite density, the phase coexistence curve terminates and all particles freeze into an ordered state. The start and end density of the coexistence region is found to be a function of activity. The coexistence region emerges purely due to the effect of activity in the system. We also discuss dynamics within the dense, ordered state.

In the final project in this thesis, we studied by simulation the effect on collective behavior of changing the symmetry of single particle activity. In addition to passive squares (that is, squares with isotropic mobility), we study polar, bipolar and chiral

mobilities. For each of these choices of symmetry we also choose different axes for the activity relative to the particle shape. We thus have six different kinds of particle and compare their corresponding phase behavior. We find that different symmetries of activity have quite different phase states. For a fixed symmetry of activity, changing the direction of symmetry leads to much smaller changes in phase behavior.

TABLE OF CONTENTS

LIST OF TABLES

Table **Page**

LIST OF FIGURES

Figure **Page**

CHAPTER 1

INTRODUCTION

Active systems are made up of agents who are able to harvest energy from their environment and propel themselves along a preferred direction in a body-fixed frame. The direction of motion is decided by the orientation of the agent instead of external fields.

There are both living and non-living examples of active matter. Examples of active agents in biological system range from flocks of birds and schools of fish to the cytoskeleton of living cells.[1, 4, 5, 6, 7].This field was first motivated by collective effects such as flocking and swarming in living agents , but scientists have also worked on analogues of living system in condensed matter systems. Examples of nonliving active matter include layers of vibrated granular particles, collections of robots and colloidal or nanoscale particles propelled through a fluid by catalytic activity at their surface [8, 9, 10].

Researchers often categorize active systems by (i) mobility symmetry of the agent and (ii) momentum conservation as shown in table 1.1.

Momentum-conserving systems like colloids are called wet active system s. Viscosity damps the relative motion of agents and environment, but with the fluid and the agent taken together, momentum is dissipated only slowly and can be treated as a hydrodynamic variable. However, if the fluid can absorb momentum locally, agents can transfer momentum with no momentum conservation[1]. Systems that do not conserve momentum refers to dry active systems. In addition to the inert fluid example, another case is active agents contact with with substrate which serves as

	Nematic	Polar
Dry	Melanocytes[11] Vibrated granular rods[8]	Migrating animal herds[12] Migrating cell layers[13] Vibrated asymmetric granular particles Films of cytoskeletal extracts[14]
Wet	Suspension of catalytic colloids rods[10]	Cell cytoskeleton and cytoskeletal extracts in bulk suspensions[15] Swimming bacteria in bulk[16] Pt catalytic colloids[17]

Table 1.1: Example of how active matter systems are classified. The table is from a review article entitled *Hydrodynamics of Soft Active Matter* [1].

a momentum sink. In this thesis, we focus on 2D vibrated granular matter as an example of a dry active system. Here objects can collide and transfer momentum to each other, but they can also locally lose momentum to the substrate

In most of this thesis, we work with systems that have a polar symmetry of mobility. As we will explain, one advantage of working with a dry system is that we have greater freedom to control and design the activity and shape of the agent.

In this dissertation, we focus on a 2-dimensional vibrated granular system and the individual agents in our system are hard squares. Granular particles enable us to have more freedom to control the interaction between particles and the direction of mobility. Here, the steric interaction between particles have four-fold rotational symmetry due to the particle shape we chose, however, clearly other symmetries are possible to design. On the other hand, we select the activity of the particle by different means than its 2D contour. We are thus able to create hard squares with different symmetries of activity with no change in the four-fold interaction. Primarily, we worked with squares that have polar mobility. In most active-matter research, direction of activity aligns with the direction of interaction axis[8]. The ability to independently break two kinds of symmetry in a single particle: the steric interaction and direction of self-propulsion allows us to study the competing effects of these considerations in packing and ordering of system. The asymmetry caused by

self-propulsion could break or enhance the structure. The combination of these two could lead to interesting effects on the dynamics and nonequilibrium phases of active matter.

One important point is to clarify the terms: Brownian particle, passive particle and active matter that are commonly used in the thesis. Brownian particle refers to particles in thermal equilibrium. Therefore the particle is heated by a thermal bath, and all degrees of freedom get the same amount of energy due to Equipartition theorem. Active particles are subject to nonequilibrium bath with isotropic noise as well as preferential noise in the mobility direction. But not all nonequilibrium system is called active matter. A distinctive and defining feature of active system is that the energy input that drives the system out of equilibrium is local, for example, at the level of each particle[1]. Note that these active systems differ from other nonequilibrium systems that are driven at a large scale, such as driving at the boundaries as in a shear flow or by a uniform potential field. The driving direction of active particle may follow some locally defined field, which may range from simply the particle orientation to something more complex such as the connectivity among cells[18]. Particles with only isotropic noise but no self-propulsion will be referred to as passive particles, or isotropic particles; terms that will be used in this thesis interchangeably.

Most of the previous research work we refer to in this introductory chapter is directed towards studying the generic MIPS phenomenon i.e. clustering due to activity, in the absence of attractive interactions between particles. However, what my thesis studies is systems that even in the absence of activity have some ordering. The four-fold interactions symmetry of square leads to ordering in passive particles[3, 18]. Our contribution will be to show how the ordering can be changed by activity.

1.1 Outline

In this dissertation, we study the dynamics and collective structure formed by active hard particles in 2-dimensions. The example used in the thesis is that of granular hard squares that under vibration can have biased propulsion in desired directions to render them into an active system. Our goal is to test whether adding designed activity creates new phase behavior or new collective effects.

We manufacture the particles by 3D printing and drive them by placing them on a horizontal plane that is subjected to vertical vibration. We can artificially create mobility by designing in geometrical asymmetry. On a single particle level, we are able to change both the symmetry of the mobility and also change quantitative parameters of its dynamics and fluctuations. We then use the designed particle to investigate the effects on collective effects at finite densities.

I will describe the basic setups for the experiment in Chapter 2. My discussion includes experimental apparatus, vibration parameters, design of the granular hard squares, particle detection, tracking techniques and data analysis methods. Most of these techniques are shared by the experiments experiments described later in the thesis. Particles in two experiments have same design but with different size and corresponding detection methods. Details of each project will remain in the appropriate chapters.

In Chapter 3, I introduce a project that studies spontaneous one-dimensional collective motion of hard squares when they move along a circular boundary. I started my research from designing a square rigid particle with preferential velocity along one of the diagonal. Such particles in the long-term end up migrating to the boundary of an experimental system. This specific type of activity leads to interesting behavior when particles approach the boundary of a confining cell. We find that a particles form a single layer or 'ring' and perform a stable global rotation along the boundary. If the particle are oriented in a fully polarized manner, the collective velocity exceeds

the velocity of a single particle in the bulk. We further investigate the relation between collective velocity and density as well as the spatial and temporal correlation function. We also run the experiment at different vibrating amplitude and frequency. To study the interaction between rings, we study two rings of particles and their dynamics.

In Chapter 4, I describe work in which we present what we believe is the first experimental phase diagram of self-propelled particles, with hard squares. This project target is to study how non-equilibrium activity changes the ordering and structure of passive squares[3]. We explore two axes of the system: activity and density. For selected values of activity, we move along the density axis and investigate the phase formed by particles. Before proceed to the details of this work, I first describe the biggest challenge in dealing with an experimental active matter system – boundary clumping – and how we solve it by increasing the rotational diffusion, a different strategy than other researchers have used. With this method, we can also change the activity effectively. We find introducing non-equilibrium activity causes phase coexistence that is not observed in the equilibrium counterpart. The single-particle dynamics in each phase could be used to effectively distinguish the phases. We also study the local orientational molecular order and bond order in detail. As a complement to the experiment we also performed simulations with period boundary condition. The results quantitatively agree with the experiment. This indicate the phase coexistence observed in experiment is not caused by boundary effects but by the intrinsic properties of self-propelled particles. It also enriches our abilities to explore other non-equilibrium activity that are not easily achieved in experiment.

In Chapter 5, we further explore the symmetry of activity by simulation. Activities can have various symmetries and the symmetry need not be the same as that of the interaction potential. For the cases I study here, this amount to saying that the interaction potential has a four-fold symmetry, but the mobility may have different symmetry.Here we study particles with three different symmetries for their mobility:

polar, bipolar and chiral activity. For each symmetry, we also study two different choices for the orientation of activity relative to the orientation of the particles. We find that different symmetries of activity lead to substantially different phase behavior. However, for a given symmetry of activity, changing the direction of symmetry leads to much smaller changes in phase behavior.

In the last chapter, I summarize the results of all my three projects and propose ideas for exploration based on our system. Currently, we have both self-propelled hard squares as well as passive ones. One tempting experiment is studying a system of passive-active mixtures. In this system, we can control the ratio of active particle and thus further extend a third axis on the phase diagram. One potential challenge in this experiment is how to effectively control the dynamical fluctuation of two different particles within the same system so that they are comparable except for the activity. Another future project is to manufacture particles with different symmetry and study the phase diagram experimentally. Finally, we can greatly improve the simulation efficiency and increase the number of particles by GPU parallel computation.

CHAPTER 2

EXPERIMENTS AND METHODS

This chapter describes the experiment setup for creating and characterizing the motion of self-propelled granular particles in two dimensions, the technique to detect positions and orientations of particles as well as the methods to analyze the motion of particles. All of my research was conducted in the same setup but with different particle sizes, particle design and material.

2.1 Experiment Setup

The experimental system is composed of a circular cell that confines the particles to a horizontal plane(Fig 2.1). The circular cell has a radius of $101.6mm$ and is composed of an aluminium substrate and scratch-resistant acrylic top case. The upper plate is transparent so that we can set up a fast camera to record the motion of particles from a top view. The gap, ranging from 4.318mm to 6.35mm, between the cover and base is determined by quasi-two-dimensional spacers (details will be discussed in section 2.6). We attach the base, top case and spacers with twelve bolts that uniformly distributed around the rim of the cell. The uniformity of the gap is crucial to ensure spatially homogeneous dynamics; to prevent the gap from being unevenly squeezed by the bolts, we used a torque wrench that could controllably apply the same torque on the bolts.

Particle are confined to the horizontal substrate of the cell. The particles are energized by vibrating them in the vertical direction, and allowing them to move in the horizontal plane. As discussed later, they can be designed to have a preference

for any direction of motion. Some examples are squares that have isotropic motion [18, 3], and polar squares that move preferentially towards one of the edge[18, 19]. However, in most of what I discuss, the particles are designed to have polar activity – that is, a preferred direction of propulsion – along a body diagonal.

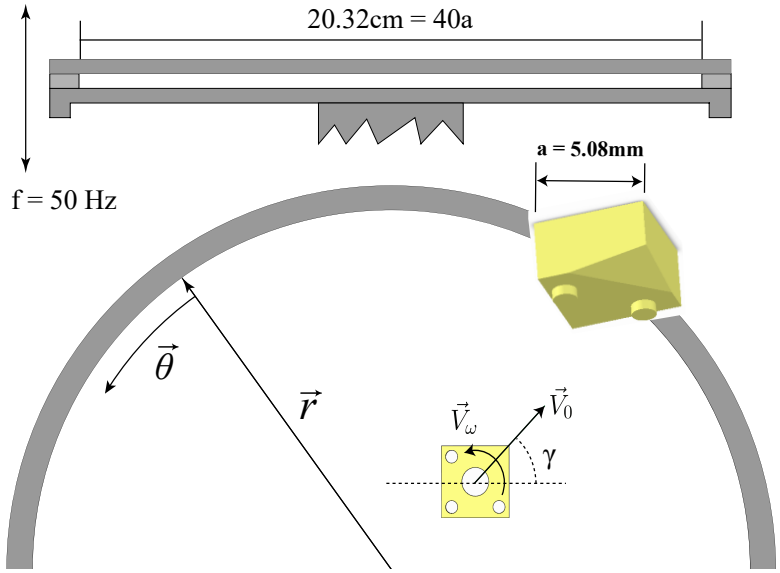

Figure 2.1: Experimental setup. (a) Side view of the vertically vibrated cell. (b) Top view of the cell defining lab-fixed coordinates(r, θ), as well as the particle body coordinates. The white dots help determine the $x - y$ location of the particle and the orientation angle, γ relative to a lab-fixed axis. The mobility direction is defined by the vector $\vec{V}_o$ along one of the diagonals of the square.

2.1.1 Vibration

Particles gain activity by interaction with the vibrating aluminium substrate as well as the acrylic upper plate. The cell oscillates sinusoidally in the vertical (y) direction:

$$y(t) = A\sin(\omega_0 t + \theta) \tag{2.1}$$

The displacement $y(t)$ of cell is controlled by amplifying the AC signal from a function generator (Agilent 33250A) to drive a permanent magnet electrodynamic shaker system (Ling Dynamic Systems V456 shaker and PA1000L amplifier). As in previous

work from our lab[18], the amplitude and frequency of oscillation are controlled by the amplitude V_{in} and frequency $f \to \omega_0 = 2\pi f$ of the AC signal from the function generator. As the gain on the power amplifier was not calibrated for intermediate values, this was set to the maximum value, and the amplitude was controlled purely at the function generator. The sinusoidal oscillation $y(t)$ gives peak acceleration $\Gamma = A\omega_0^2$ in unit of acceleration of gravity g.

The frequency affects the time-step of particle dynamics. We find that velocity and diffusion is proportional to vibration frequency[18]. Thus we report times in units of the vibration period 1/f. In this dissertation, I typically used frequency $f = 50\text{HZ}$ and signal amplitude $V_{in} = 100mV$. The response of PA1000L amplifier is linear with $A = 1.071 \times 10^{-6} V_{in}/mV$ and the relative uncertainty is 4%[18]. These parameters lead to an acceleration amplitude

$$\Gamma = A\omega_0^2 = 1.071 \times 10^{-4} \times 4\pi^2 \times 2500 \approx 10.57g \tag{2.2}$$

All the experiments are implemented under these parameters, unless otherwise noted.

In order to mitigate the undesired effects of off-vertical or asymmetric vibrations, a stiff linear air bearing (New Way Air Bearings S40-03050-025152) is used to rectify the motion of the shaker, transmitting only the vertical component of vibration to the substrate[18]. This setup is implemented by rigidly mounting the substrate to the linear air bearing, which is coupled via a flexible rod to the shaker. In detail, the particle dish is bolted directly to the upper end of the square rail of the bearing, which glides vertically through the bearing carriage. Pressurized air (lab supply) is filtered, dried, and regulated (SMC Pneumatics AWD30-N02DE-Z) and supplied to the carriage at 410 kPa. This allows only vertical motion to be transmitted through the bearing, while any transverse or rotational motion is dissipated through the flexing of the rod.

2.1.2 Vibration Testing

One big concern of the experiment is whether the cell oscillates as a rigid object. In other words, we determine whether all points on the plane vibrate with the same displacement amplitude and phase. In order to check that, I took a high speed video of the side-view of the vibrating cell. I painted half of the bolts to white and mounted on the circular cell. To determine the location of marked bolts from digital images, I convolved the image with a Gaussian kernel[20] using the same method that I will describe for particle detection Section 2.3. The kernel is similar to the Fig 2.3 but with negative pixel value since we want to find white location on dark background. The contrast of white painted bolts to the background enable us to identify the location of bolts. I determined the motion of the bolts in the y-direction with time(Fig 2.2). The curves are expected be to sinusoidal. I used the *curvefit* function from Scipy modules to fit the curve to get the amplitude A, frequency ω_0 and offset phase θ of the bolts. The results are illustrated in Table 2.1.

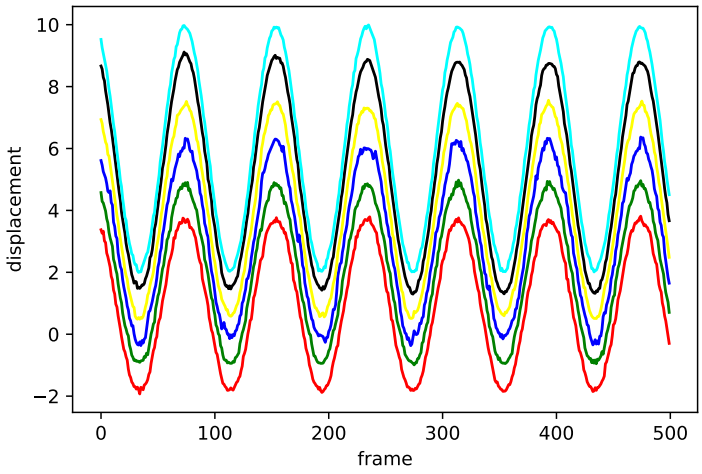

Figure 2.2: Displacement of 6 bolts in y-direction in 500 frames. I used the position to fit the parameters: A, ω_0, θ.

Since distances between all bolts to camera are different, the amplitude A is different. However, ω_0 and θ have the same time-dependence indicates that the cell plane vibrates in-phase as a rigid object.

	1	2	3	4	5	6
A	2.79921	2.90071	3.16954	3.41863	3.75766	3.92718
ω_0	79.99959	79.99909	79.99922	79.99905	79.99790	79.99952
θ	-1.06309	-1.06183	-1.07385	-1.06673	-1.07697	-1.07511

Table 2.1: Fitting parameters of 6 bolts. Amplitude is different due to depth of field. Frequency and offset phase are consist for all bolts.

2.2 Particles

I designed the particles within a CAD program called Solidworks and manufactured them by 3D printing. The particles are designed to have preferred motion along one of the diagonals, so they have a 14° wedge along that diagonal and rest on two short round legs on the wedge sides.

For the project on collective motion of self-propelled particles in one-dimensional ring (I will call them black large particles in the following sections) described in Chapter 3, particles are printed from ABS thermosetting resin by uPrint SE Plus 3D printer with a manufacturer-specified layer thickness of $0.254mm$. The particle has a square cross-section with side $a = 7.62mm$ and maximum height of $5.4mm$. We choose black ABS material as it gives good contrast with white markers for detection. It also has good resistance to stains brought by long term vibration. One big issue with the ABS material is that the printing resolution constrains our ability to have smaller particles. Based on the size of the particle, the maximum possible number of particles could be placed in the cell is 559. This number limits the area fraction choice for my second project on active phase diagrams, and therefore we developed smaller particles as well.

For phase diagram of granular self-propelled particles (white small particles) described in Chapter 4, the particles are 3D printed on a EOS Formiga P110 printer in white colored nylon-12 PA2200, with a square projection of side a= 5.08mm and maximum height of 3.6mm (2/3 size of the black particle). The most significant advantage of this printer is its 0.1mm layer resolution that enables us to have smaller particles. The maximum possible number in the cell with this particle size is 1256 (2.25 times more than the black larger ones). Since the marker size scales with particle size, smaller particles cause greater difficulty in detection. The other challenge is that particles are white in color, which was the only option when I manufactured them. The particles easily get stained as we keep repeating the experiments. The stains leads to larger detection noise in locating particle position and orientation. Therefore, we used two different kinds of detection method for black large particles and white small particles respectively.

2.3 Particle Detection and Tracking

To analyze the dynamic behavior of particles, we are required to get not only the position but also the orientation of particles. Since our polar particles are designed to move along one diagonal, we need to track this direction. We painted high contrast marks on the particles for detection. For large particles, I used Sakura 42180 Blister Card Pentouch Metallic Extra Fine ink white marker. For small particles, I painted with Uni-ball Signo Gel black ink Pen with width 0.38mm. We had one big central marker to get the positions and three small makers to get the orientations. To ensure the position of all markers is consistent, I designed four shallow circular holes on top of the particles when I printed them. After particles are manufactured, I simply located the holes and painted them with the appropriate marker pen.

As mentioned in the previous section, I used two different detection techniques for particles, and these are described below.

2.3.1 Mean Vectors Method

The first technique is identical to our previous work [18]. The idea is to find the positions of both the central marker and the three corner markers on each particle by standard methods which I describe in the next paragraph. We then calculated vectors from the central marker to each of the corner markers. We used the mean of these three vectors to indicate the orientation of that particle.

In order to determine positions of the markers, I constructed a Gaussian kernel to convolve with the output digital image of recorded videos[20]. The two-dimensional kernel is symmetric in all directions as shown in Fig 2.3. The integral over the kernel equals to zero. Therefore the convolution with background pixels of uniform intensity returns zero. If there exists contrast in pixel values due to a feature in the image, and the size of the feature is comparable to the Gaussian kernel, the convolution returns a local patch with a non-zero value. By filtering the eccentricity and the area of the nonzero region, we get the position of markers by calculating the center of mass(Fig 2.4(c) and (d)). We could detect both the central and corner markers by using Gaussian kernels of different width, to match the sizes of these two different features.

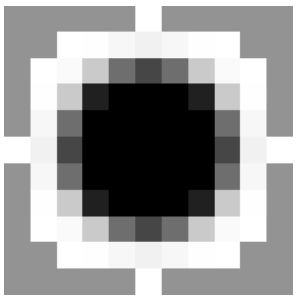

Figure 2.3: Gaussian kernel that is designed to convolve with black marker and white particle. The kernel is symmetric in all direction and the integral over the kernel equals to zero. The white pixel value is negative and close to -1. The highest pixel value or darkest is around 1.3

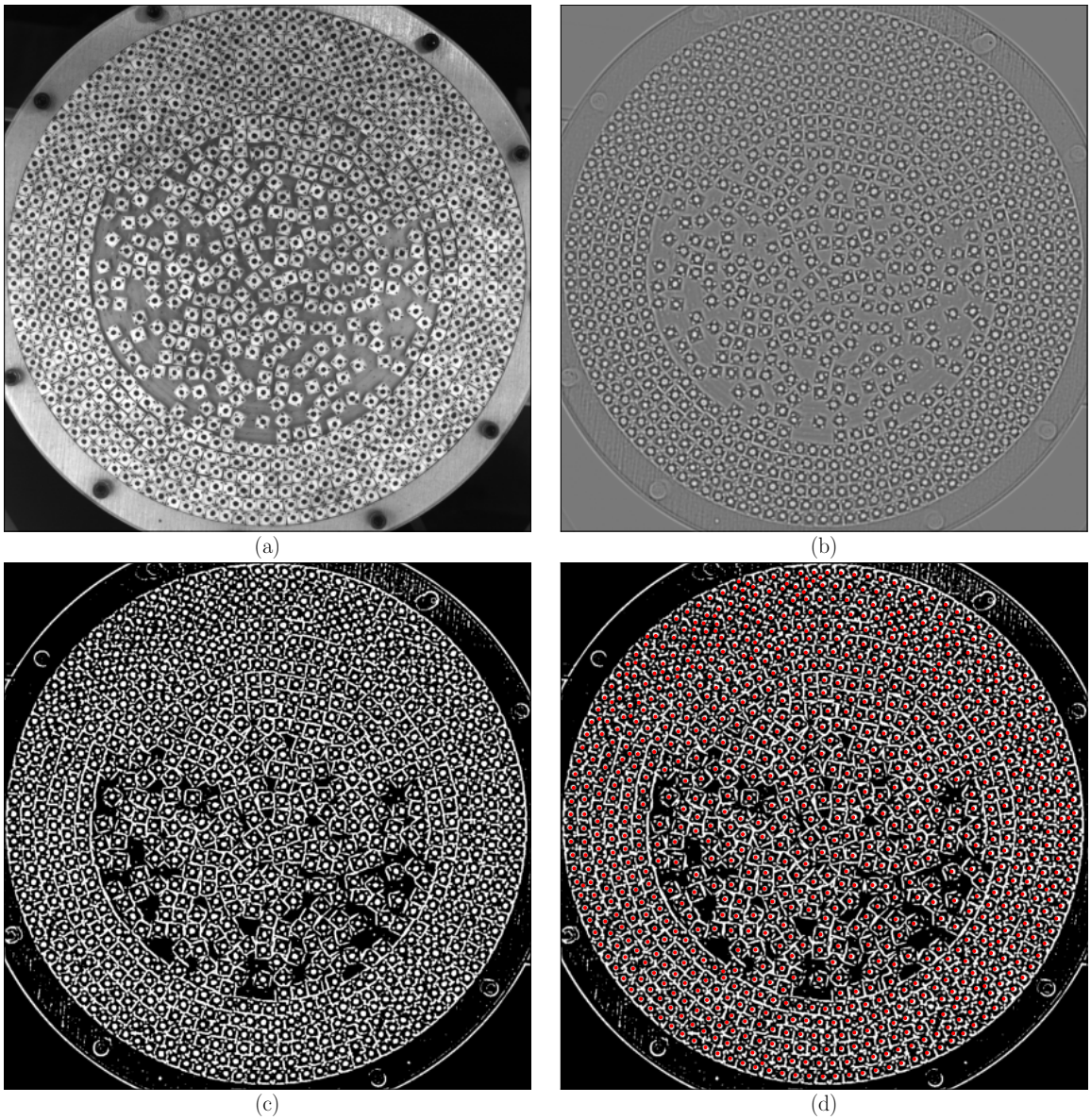

Figure 2.4: (a) An example frame consists of 950 particles in gray scale. (b) The output image after applying the Gaussian kernel(Fig 2.3) (c) I picked a threshold of normalized pixel intensity $\kappa = 0.52$, then I found all pixels in (b) that are larger in intensity than κ and set them to 1; other pixels were set to 0. (d) I checked all connected single-valued regions in (c), if the area of connected region is larger than 40, smaller than 180 and eccentricity is smaller than 0.9, I identified the center of mass of connected region as the position of central marker.

To detect the orientation of particle, we construct k-d tree[21] finding all corner markers within a certain radius (in pixel units) given the location of a central marker. We feed positions of both central and corner markers to k-dimensional tree package in scipy[22]. The k-d tree is a space-partitioning binary tree in which every leaf node is a K-dimensional point, in our case k equals to two. Every non-leaf node can be thought of as the splitting hyperplane that divides the space into two parts. Points to the left of this hyperplane are represented by the left subtree of that node and points to the right of the hyperplane are represented by the right subtree. The hyperplane direction is chosen in order of each k dimensions alternatively. In our case, we split the space based on the position of x-axis first then y-axis and then go back to x-axis. K-d tree is useful for its efficiency in nearest neighbor searches and range searches with time complexity $\mathcal{O}(\log(n))$ We make a range query on the tree based on position of central marker and pixel radius to locate the corner markers. We also add a minimum distance requirement. If the number of corners found by this algorithm does not equal to three, we drop the result of the central position, that is, we discard this as an identified particle.

This method works robustly on the large black particles. Both central and corner markers could be correctly detected with error rate $\lesssim 0.1\%$. If we miss position or orientation of a single particle in one frame, we can easily solve it interpolation of data from previous and next frame where the particle is detected.

However, this mean vector method returns a lot of errors when working on the small white particles due to their small size and their white color which degrades with time.Some drawbacks of the method are

1. The markers scale with the size of particles. Although the central markers can be detected, some of the corner markers are too small to be detected. Since markers are painted manually, it is hard to control the size of marker. Therefore, I cannot easily set a simple rule of area and eccentricity to filter out erroneous

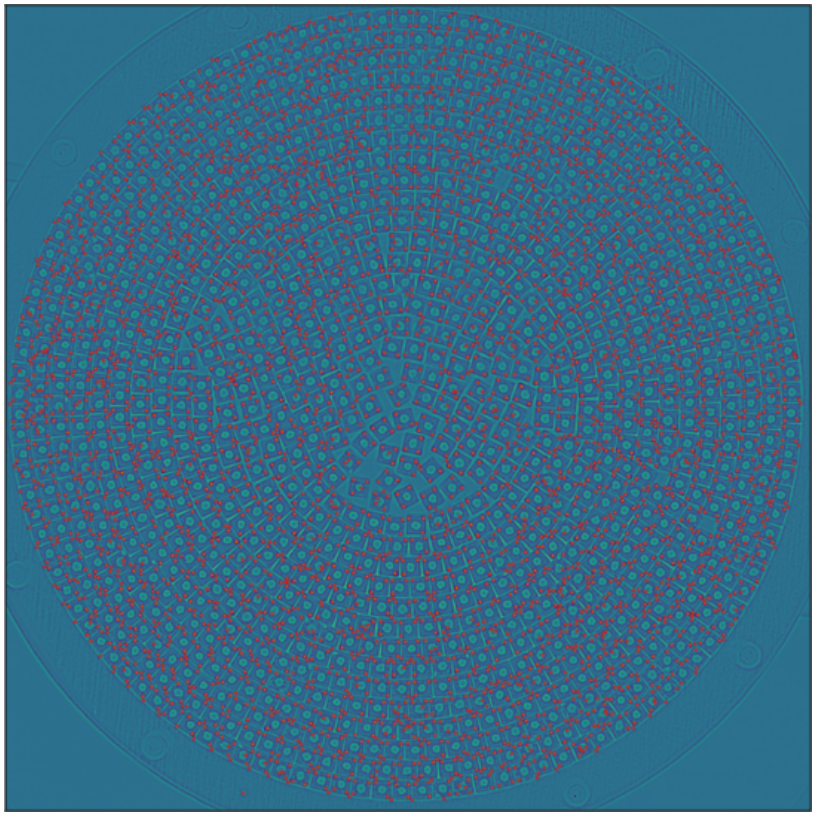

Figure 2.5: Small markers caused a lot trouble in detection when density is high. The stains on particles would be falsely identified as corner markers. If the kernel width is inappropriate, corner markers would merge with the background so that they were not detected.

detections and identify the corner marker correctly. As showed in Fig 2.5, the lower bound of area is set to 5 pixels to include as many as corners as possible. The side-effect is that many smudges are identified as corners as well.

2. Particle are white. As I keep doing the experiment, they become dirtier and stained. Some smudges are identified as corner markers. This introduces noise in the identification and caused trouble when trying to link corners to central marker.

3. At high area fraction ϕ, particles are closed packed with their neighbors(Fig 2.6). Some corners from different particles are very close to each other, if the width

of Gaussian kernel is set inappropriately, the convolved result would identify them as one big dot.

Figure 2.5 shows the errors. To summarize, with manually chosen area and eccentricity, we cannot effectively distinguish error and real markers when particle is small and white. The high error number also means the K-DTree is large so that the time complexity of the query function to group particles greatly increases.

2.3.2 Convolutional Neural Networks

In order to overcome the drawbacks of the direct detection method, I developed a hybrid method for detection: Gaussian kernel for positions, and deep learning networks for orientations.

I used Convolution Neural Networks(CNN) for their power in computer vision tasks[23]. For my purposes, I decided that accuracy of orientation of particles with 1° resolution is acceptable. Therefore we defined orientation detection as a classification problem instead of a regression problem. Given a particle, the network should return the orientation in unit of one degree. There are total 360 different classes(one category corresponds to one degree). The details of hybrid methods are listed as follow:

1. Used a Gaussian kernel to find positions of central marker.

2. Cropped a 32×32 pixel sized image that is centered at result of previous step.

3. Feed it into a one-layer CNN. This layer identifies whether this image contains type of particle. If it is not a particle, then the image is dropped from considerations. Otherwise, it is used as an input to the orientation classification networks. We find that the network has 100% prediction accuracy in this step.

4. Feed the correct images of particles to a three-layer CNN. The details of the networks is shown in Table 2.2. To understand the functionality of each layer(batch

normalization and dropout), please refer to Neural Network lecture note[24]. The final output is the predicted orientation.

Layer Structure
CNN {c:64, k:(3,3), s:(1,1), p:(1,1)}, BatchNormalization, Dropout, ReLU
CNN {c:64, k:(3,3), s:(1,1), p:(1,1)}, BatchNormalization, Dropout, ReLU
CNN {c:256, k:(3,3), s:(1,1), p:(1,1)}, BatchNormalization, Dropout, ReLU, MaxPooling

Table 2.2: Structure of three layer Convolutional Neural Networks. In each CNN, 'c' stands for channel size, 'k' stands for kernel size, 's' stands for stride and 'p' stands for padding size.

I wrote a script to build the training data of the CNN. First, I cropped 32×32 pixel size images based on all the detected central marker position (Fig 2.6) and then transformed them to 128×128 pixel so that I could achieve a higher orientation accuracy. Second, I assigned each image to either be a particle or an error. If it is a particle, I used a mouse to manually click two points on the image to calculate orientation. Finally, I rotated the cropped images and changed the corresponding orientation γ to $\gamma + 90°, \gamma + 180°$ and $\gamma + 270°$. Therefore I could quadruple the number of original training images. In this project, I used around 12000 training images in total.

In this method, we don't need to detect positions of corner markers. Instead, they are used as features for the network to find the orientation. Running the network on GPU Nvidia RTX 2080, the time efficiency of detection of 10000 frames of 1000 particles is 8 times faster than the previous method.

One example of our detection results is shown in Fig 2.7. If the predicted orientation is within the range of $\pm 2°$ of the real one γ, then we treat is as a correct prediction. The average accuracy is higher than 99%. The wrong prediction happened to predict orientation as $\gamma + 90°, \gamma - 90°, \gamma + 180°$. Based on this interesting

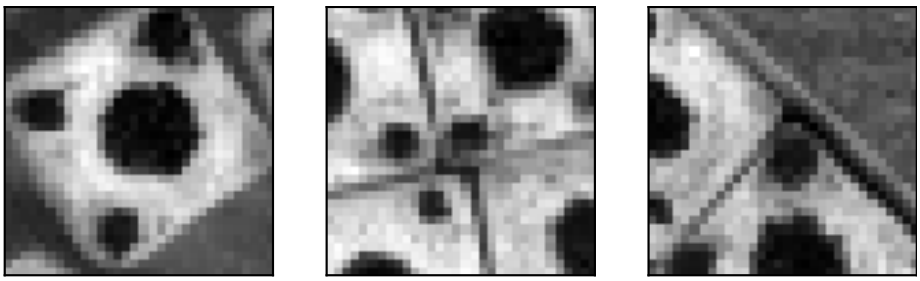

Figure 2.6: Cropped image centered at position detected by the convolution kernel. (a) Images of an actual particle. The orientation of the mobility axis of this particle is 348°. (b) and (c) are false positive identifications. The reason for the error in (b) is that particles are so tightly packed that the kernel width is larger than the distance between corners belong to different particles. The reason for the error in (c) is that the corner marker merges with the background so that it is mistakenly treated as an central marker.

observation, the results can be easily fixed at the tracking step that is described in the next section.

2.3.3 Particle Tracking

In one vibration period, the displacement of particle(normalized by particle size a) is limited($\leq 0.2a$). For each particle, we queried a K-DTree constructed by all particles in next frame, if there is only one possible position that is located within $0.2a$, then this would be the position of particle in next frame. With this linking method, we can quickly track the path of all particles due to the fact that we can get particle position in all frames with 100% accuracy. With these datasets, we could further analyze the dynamics of particles.

We could also effectively fix errors caused by the CNN method. If we plot the orientation of particle as a function of time, the curve looks like blue dots in Fig 2.8. In order to fix the errors, I first found the outliers . Then I check its neighbors value to figure out the offset value I should fix.

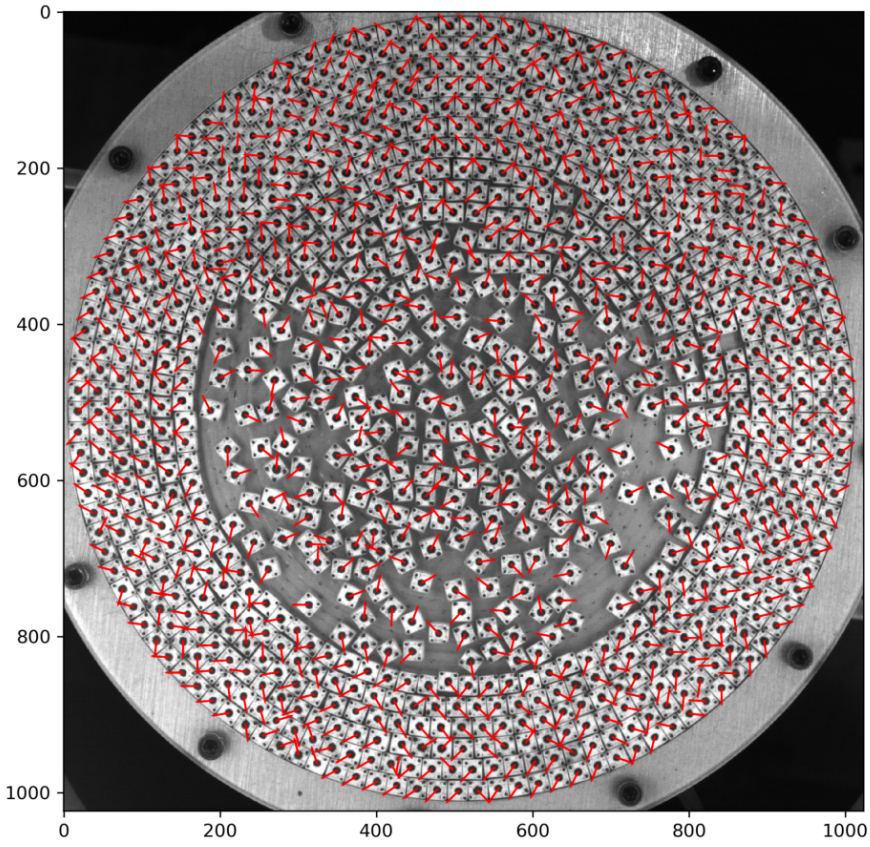

Figure 2.7: Example detection of Convolutional Neural Network method. All particles are correctly identified. The red arrows indicate orientation of each particle.

2.4 Particle Dynamics

From numerical derivatives of the observed position and orientation of particles(explained in Section 2.4.1), we calculate velocities v_l in the longitudinal direction (along the propulsion axis), v_τ, in the transverse direction along the other diagonal, and the rotational velocity v_ω about the body axis. Further, we can calculate persistence length l_p, a measurement of activity of particles in our research.

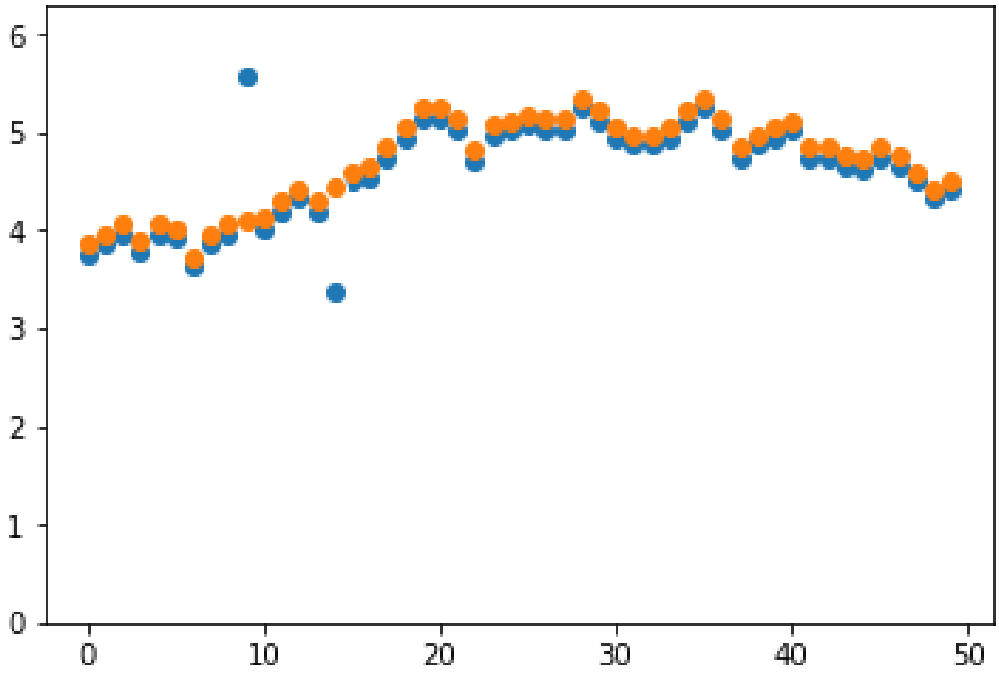

Figure 2.8: Example of orientation of particle as a function of time. y-axis is orientation in units of radians. x-axis represents time in units of video frames. The blue dots are results of predicted orientation. The orange dots are orientations after fixing the errors, as discussed in the text.

2.4.1 Dynamic calculation

In order to get velocities, we calculate the numerical time derivatives of observed quantities Q: positions or orientations. We get Q from a high-resolution video, or thousands of digital images. This indicates all Q are discrete. To smooth the result, we convolve Q with Gaussian kernel $g(t) = \frac{1}{\sqrt{2\pi}\sigma} e^{-t^2/2\sigma^2}$.

$$\frac{d}{dt}(Q * g) = \frac{dQ}{dt} * g = Q * \frac{dg}{dt} \tag{2.3}$$

This equation shows that smoothed time derivative of Q with kernel g equals to smoothing Q with time derivative of kernel g. This greatly simplified the complexity since the time derivative of dg/dt is straightforward and we can easily implement the convolution.

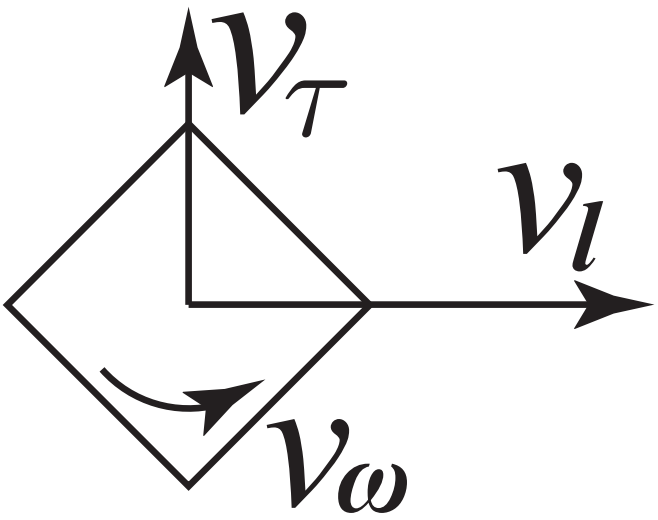

Figure 2.9: Definitions of velocity components: Longitudinal velocity v_l, transverse velocity v_τ and rotational velocity v_ω

To calculate velocities of particle along certain direction, we first get time derivative of position along x and y direction in unit of pixel. Then we project $\dot{x}, \dot{y}$ to our desired direction β

$$v_\beta = \dot{x}\sin(\beta) + \dot{y} \tag{2.4}$$

2.4.2 Persistence Length

In experimental systems as well as in simulations, activity is often quantified by the nondimensional Péclet number, defined as $Pe_T = v_o a/D_T$ or as $Pe_R = v_o/(a.D_R)$ where v_0 is a characteristic velocity along a body-fixed axis, a is the size of the active particle, and D_R, D_T are rotational and translational diffusion coefficients. In systems where the diffusion constants D_R and D_T stem from thermal noise, Pe_R and Pe_T are equivalent. However, in a granular system, the noise source is intrinsically nonthermal, and D_R and D_T are, in general, unrelated to each other and can vary independently. For the systems we discuss here, the latter definition, i.e. $l_P = Pe_R = v_o/(a.D_R)$ is more relevant[19]. The acronym for Péclet number also fortuitously stands for the persistence length, l_P, which represents the characteristic distance travelled along

a preferred direction before the body-fixed axis changes orientation, normalized by particle size a. We use l_P as a measure of single-particle polar activity.

We can get diffusion constant from the velocities due to the fact that they are equivalent to rotational and translational displacements of particles in units of particle size in one vibration period. From the velocity distribution, we extract the three parameters that characterize the dynamics in the Active Brownian Particle model [25, 26, 19]. The mean value of displacement along the diagonal propulsion axis, $\langle v_l \rangle$, is non-zero and gives the propulsion speed, v_o. The orientation displacements v_ω and translation in the transverse direction, v_τ, are zero-centered and are normally-distributed. The variances of the translational and rotational displacement histograms yield the diffusion constants, D_T and D_R, respectively.

In our experiment, we can vary persistence length l_p effectively by changing the ratio between particle height to gap height of the cell $\lambda = h_p/h$. Specifically, D_R increases with λ. We will explore the details of each parameter in the following chapters.

2.5 Dilute Behavior

In this section, we study behavior of dilute particles when $l_p = 2.29$ and $N = 12$ or $\phi = 0.01$ in two different region: dynamics in the bulk of system and diffusion near the boundary.

2.5.1 Dynamics In The Bulk

To get sing-particle dynamics in the bulk, we distribute a small number of particles randomly in the bulk of the system with random orientation(Fig 2.10). We exclude data when particles are close to the boundary to remove the interaction between walls and particles. When distance between center of particle to the wall is smaller than specific threshold $1.25a$(particle size), the corresponding data are dropped.

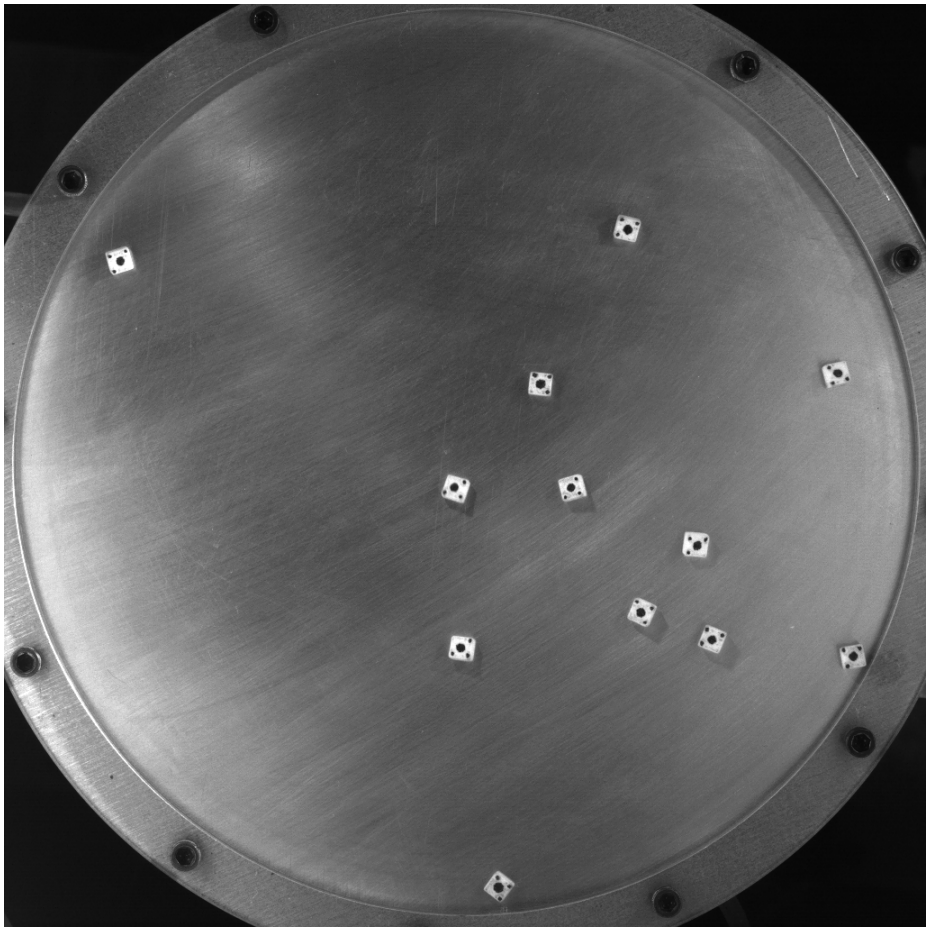

Figure 2.10: Snapshot of initial configuration of dilute particles when $N = 12$ and $\phi = 0.01$. Dynamics of single-particle motion are captured from video at 250 frames per sec (fps).

We compare our results to the Active Brownian Particle (ABP) model[27]. In the simplest version of ABP model, the center of mass velocity of particle is composed of two parts, a constant velocity v_0 along certain body-fixed direction $\vec{n_0}$, and a translational noise $\eta(\vec{t})$:

$$\dot{r}(t) = v_0\vec{n_0} + \eta(\vec{t}) \tag{2.5}$$

The rotational velocity of $\vec{n_0}$ is determined by a noise term $\zeta(t)$:

$$\dot{\theta}(t) = \zeta(t) \tag{2.6}$$

Within the ABP model, translational and rotational noise are normal distributed, zero-centered and with variance $2D_T$ and $2D_R$. There is no spatial or temporal correlation in the noise terms. The short-term dynamics are fully captured by v_0, D_R and D_T. As discussed earlier, these are not necessarily true in a system, such as ours, with nonequilibrium noise sources. Thus, these assumptions must be tested within experiment, as we have previously done in our research group[19].

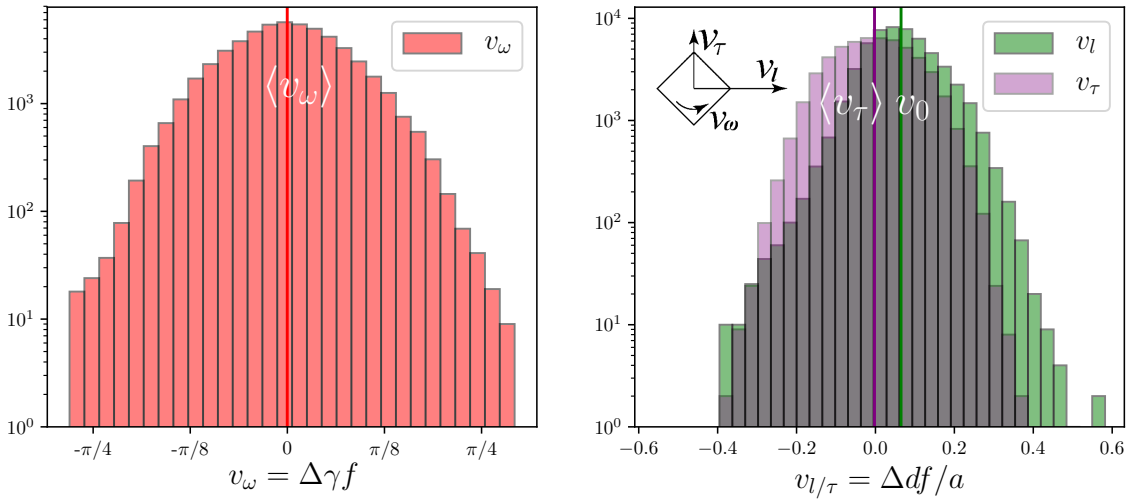

Figure 2.11: Single particle dynamics captured by imaging particles at low density, $\phi = 0.01$. Histograms of (a) orientational velocity v_ω , and (b) translational velocity, v_l, along the mobility direction, and v_τ, along the transverse direction. v_ω is computed from $\Delta\gamma.f$, the change in orientation angle in one vibration period, while the translational velocities are computed from the displacement components Δd in the two directions, normalized to the square side a.The solid vertical lines are the corresponding mean values, showing that v_ω and v_τ have zero-centred distributions while v_l has a positive mean value v_o.

Histograms of v_l, v_τ and v_ω are shown in Fig 2.11. v_ω and v_τ are zero-centered Gaussian distributions which match the basic ABP model. v_0 has a clear deviation from 0 which indicate the preferential velocity along the diagonal direction. The velocities are equivalent to rotational and translational displacements of particles in units of particle size in one vibration period. From these distributions, we extract the three parameters $v_0 = 0.063$, $D_T = 0.005$ and $D_R = 0.283$.

2.6 Controlling Activity

In this experiment, we are able to vary l_p most conveniently by tuning the vertical gap in the cell which affects D_R strongly, and v_o more weakly(Table 2.3). As we will show, with high enough D_R, we can effectively solve the problem of irreversible trapping of particles at the boundary that is often seen in similar experimental systems.

Table 2.3: Particles dynamic details of different experimental environments

h_p	h	Height Ratio $\lambda = h_p/h$	$v_0(a/s)$	$D_R(rad/s)$	l_p
3.725	5.143	0.724	0.114	0.184	0.75
3.725	5.00	0.782	0.124	0.129	1.25
3.725	4.318	0.863	0.066	0.041	2.29
5.588	6.35	0.88	0.134	0.026	5.70

To change the height we use three annular spacers with different heights (1.5875mm, 3.175mm and 6.35mm) at the boundary that confines the particles. We also have two washers (0.381mm and 0.762mm) to adjust cell gap h. With different combinations, we achieve persistence length l_p and height relation in Table 2.3. We report the dynamics and ordering in the system at four different values of activity: $l_p = 0.75, 1.25, 2.29, 5.70$, and at several values of area fraction ϕ.

CHAPTER 3

COLLECTIVE GEAR-LIKE MOTION IN AN ACTIVE GRANULAR SYSTEM

In this chapter, we report a system of vibrated self-propelled granular particles on a horizontal plate within a circular boundary. This is a simple model system in which to consider how transport of active particles is affected by interactions. Because the system is 1-dimensional, it forms an interesting parallel to traffic models. As with real traffic, nontrivial correlations develop in velocity fluctuations, even though the interactions here are hard-core, nearest neighbor interactions, and do not include the memory or long-range signalling that is built into traffic models.

The square particles in our experiment have a preferential velocity along the diagonal, so that when they hit a boundary in any confining geometry they align along the boundary but also "walk" along the boundary. In the experiments we show in this chapter, particles initially distributed in the entire 2D space end up migrating to a boundary, form part of a ring or a whole ring along the boundary, and perform a stable 1D rotational gear-like motion with a direction chosen by their net polarization. For a fully polarized single ring we find that the collective velocity surpasses the free single-particle velocity. This collective velocity increases as the density of particles in the ring increases, which is counterintuitive for a normal traffic problem. The spatial correlations of particle velocity decays exponentially . The temporal correlation shows that velocity fluctuations are anticorrelated in time.

3.1 Ring Motion

An example of the kind of collective motion observed in this system is shown in the figure below, where we start at an area fraction $\phi = 56\%$. The initial position and orientation of particles are randomly distributed(Fig.3.1a). After starting the shaker, particles quickly migrate to the boundary due to their high persistence length l_p and form rings of particles(Fig.3.1b) along the wall. If the polarity of motion was perpendicular to the boundary, the particle would be stuck at the wall and immobile. However, the mobility along the diagonal brings interesting behavior to the wall particles. Particles try to reorganize themselves until one edge component is along the r direction(Fig 2.1). The component of motion along the wall for a given particle is either clockwise or counterclockwise. A ring of particles has a global rotation along the wall and the overall direction of the motion(clockwise or counter-clockwise) depending on the net polarization of all the particles within the ring. The directions of global rotation of each of the rings is independently determined by the net polarization of each individual ring.

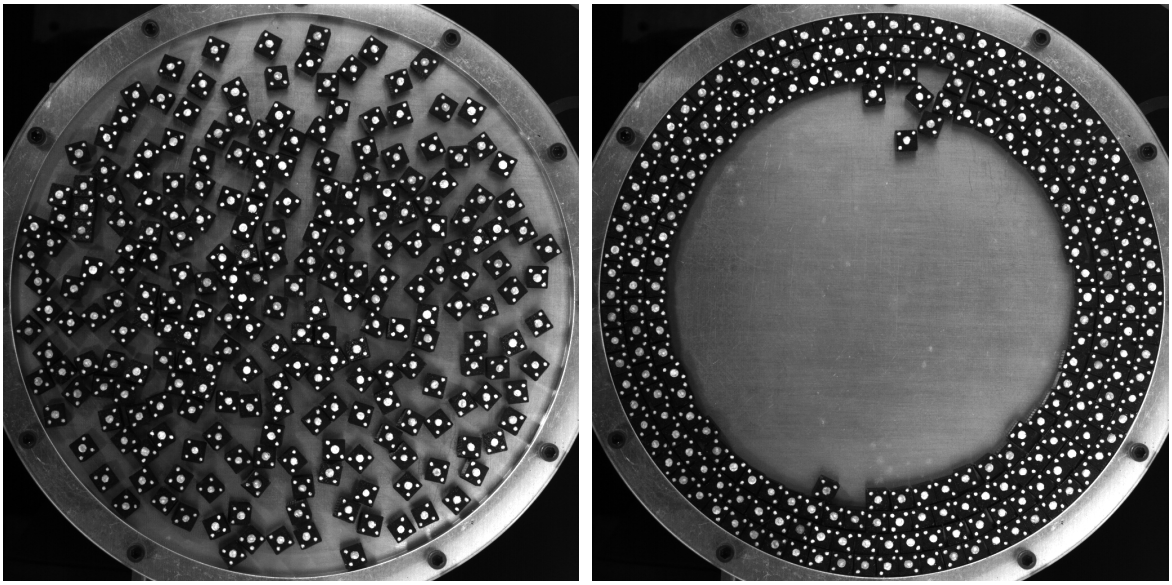

(a) (b)

Figure 3.1: (a) Random initial configuration when area fraction $\phi = 0.56$. Particles are initially distributed uniformly and oriented randomly. (b) All particles migrate to the boundary and form stable rings of particles. Each ring moves either clockwise or counter-clockwise depending on the polarization, that is, the net orientation of all the particles within a ring.

We then reduce the initial number of particles in the system to be just enough to form a single ring (75 particles in this case). Surprisingly, the ring that forms at the boundary undergoes stable motion along the wall. Particles rarely leave this single layer of particle. However, once the ring breaks due to an escaped particle, it is unlikely for it to find its way back to the vacancy in the ring.

3.2 One Dimensional Fully Polarized Ring

To explore the dynamics of the ring with a simpler initial condition than the one formed from random initial positions and orientations. Here we start with a fully

polarized configuration as shown in Fig3.2a to study the relation between the ring velocity and number of particles.

Our first observation is that the average ring velocity v_θ was larger than that of a single particle $\frac{\sqrt{2}}{2}v_0$. This counter-intuitive observation led us to further study the effects of particle number in the ring. We use vacancy fraction to quantify the empty space in the ring, which is defined as $\phi_V = (N_{max} - N)/N_{max}$. N is the number of particle and N_{max} is maximum number of particle that can be accommodated in the ring($N_{max} = 75$ in our case).

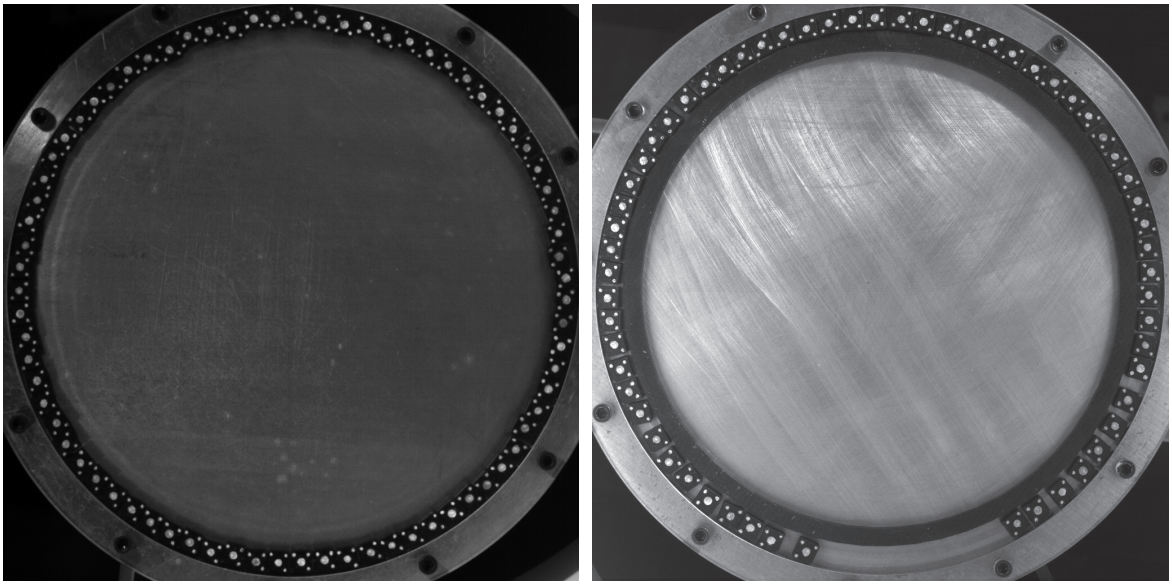

(a) (b)

Figure 3.2: (a) Snapshot of a fully polarized ring composed of maximum possible number of particles $N_{max} = 75$ that can fit along the boundary. This ring rotates clockwise and the motion is stable. Rotation velocity v_θ is larger than single particle $\frac{\sqrt{2}}{2}v_0$. (b) Snapshot of the ring when $\phi_V = 0.2$ and number of particle is 60. We add a inner wall to make the ring stable when ϕ_V is large. We start with the particles equally spaced initially but in steady state, the particles finally form one cluster. We further explore how dynamics of the ring change with ϕ_V.

We create a channel by an inner wall(Fig 3.2b) to prevent particles to escape the ring when ϕ_V is high. The ring is relatively stable, but the retaining wall allows us to study the ring indefinitely. The inner wall is 3D-printed with the same material as particle and fixed to the base with double-stick adhesive. The distance between inner wall and boundary, or channel width is set to $d = 1.3a < \sqrt{2}a$ to prevent the particle rotating in plane and changing its polarization. We also 3D-printed three supports to stabilize the inner wall and to make sure d is constant in all places.

We initially distribute particles uniformly with equal spacing in the one-dimensional channel. Though the particles are designed to be identical, there are small, random variations on the particles that cause their mobilities to be slightly different. When the particles are vibrated, this velocity difference makes particles form clusters. Faster particles can catch up to particles in front of them, while the slower particle obstruct those behind it. While the kinetics of cluster formation is an interesting process, in this thesis our focus is on the steady state, so that we take data only after particles have largely clustered, as shown in Fig 3.2b. Currently, my colleague Jacob McConley is working on the simulation of formation of clustering of one-dimensional points.

3.2.1 Velocity

Before changing ϕ_V We first investigate the dynamics of a single ring of particles. The activity of every particle can be decomposed in two components: one along $\vec{r}$ and one along $\vec{\theta}$ (Fig 2.1). We characterize how particles are aligned the wall by a parameter

$$\epsilon = \frac{\vec{r} \times \vec{v_l}}{\sin(\pi/2)|r||v_l|}. \tag{3.1}$$

When $\epsilon = 1$, the particle is perfectly aligned along the boundary. We take $N = 75$ for example. The distribution of ϵ is plotted in Fig 3.3(a). Individual particle velocity v_θ is normally distributed with nonzero mean as shown in Fig 3.3(b). The radial

velocity v_r has zero mean but is suppressed by the channel Fig 3.3(b). As expected, rotational velocity v_ω is normally distributed.

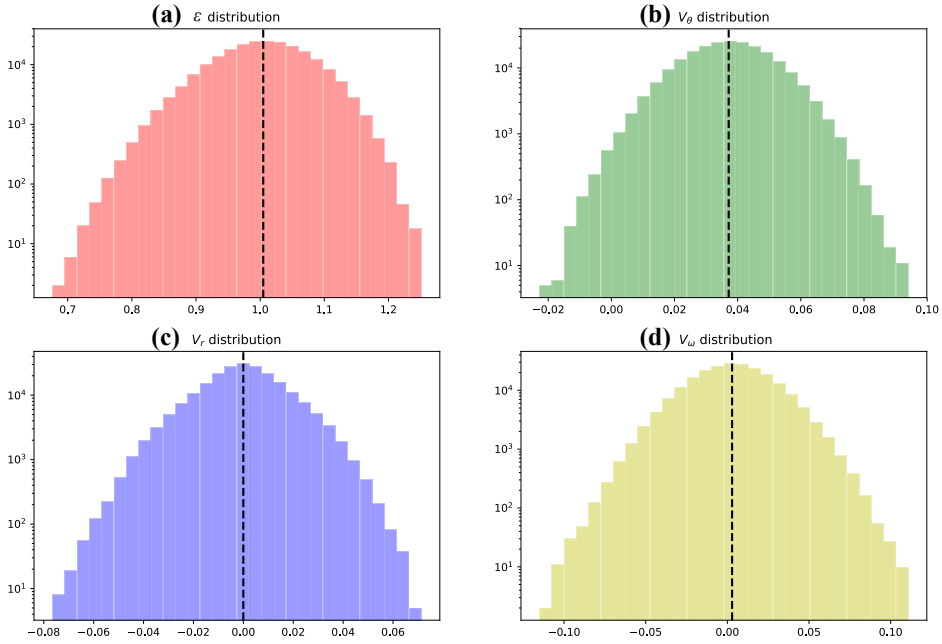

Figure 3.3: Velocity distributions of particles confined to a ring.

Our basic result is that the azimuthal velocity, v_θ, of the particles decreases as vacancy fraction ϕ_V increases as shown in Fig 3.4a. v_θ is normalized to velocity of a single particle $(v_\theta)_{single}$ moving in the channel. We first pack in as many particles as we can, and then perform experiments with varying N, first by removing particles out of the channel one by one until $\phi_V = 0.07$ or $N = 70$ and beyond that in larger increments. A fully filled ring has the largest velocity and the smallest fluctuation(Fig 3.4b) in velocity. As the vacancy fraction increases, the normalized velocity drops sharply, however the fluctuation increases quickly. At larger vacancy fraction, the normalized velocity and standard deviation change more slowly as we approach

the dilute limit. This counter-intuitive observation shows that contrary to traditional traffic problem, the particles move faster as the channel get more crowded.

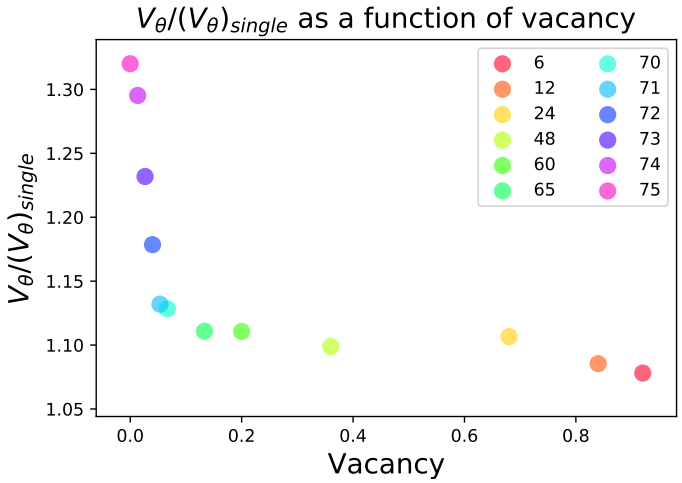

(a)

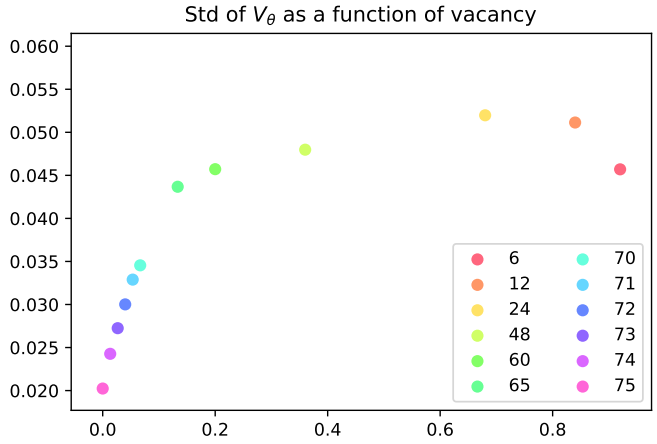

(b)

Figure 3.4: (a) Normalized velocity decreases with vacancy fraction ϕ_V. (b) Standard deviation of v_θ increases with ϕ_V.

3.2.2 Correlation Function

Our results indicate that our one-dimensional layer of particles show collective dynamics. We further explore the mechanism of the collective dynamics through the

correlation function. With the time-dependent data in the steady state, we can get both the spatial and temporal correlation function of particle velocities.

The equal-time spatial correlation function of v_θ is defined as:

$$f(j) = \frac{\langle\langle (v_i(t) - \langle v_i(t)\rangle)(v_{i+j}(t) - \langle v_{i+j}(t)\rangle)\rangle_i\rangle_t}{\langle\langle \sqrt{|v_i(t) - \langle v_i(t)\rangle||v_{i+j}(t) - \langle v_{i+j}(t)\rangle|}\rangle_i\rangle_t} \tag{3.2}$$

where i and j are particle indexes. The denominator normalizes $f(j)$ to 1. In order to get correlation at separation j, we average over $N/2$ particles for a maximum j of $N/2$ and then average over time. The spatial correlation $f(j)$ is shown in Fig 3.5 at a range of particle numbers.

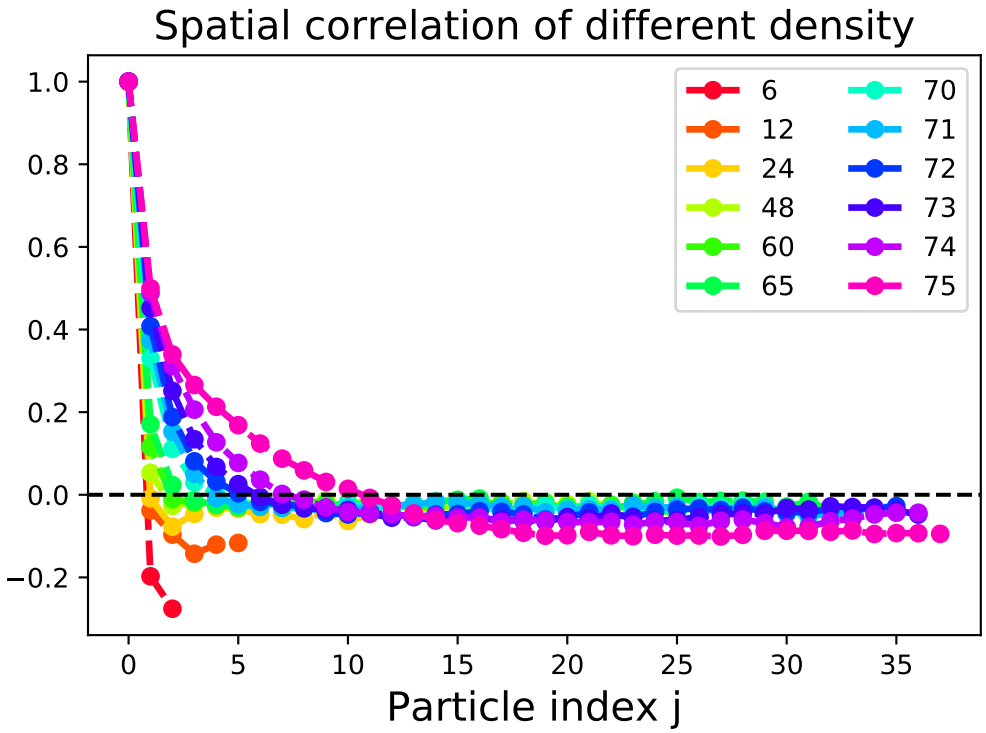

Figure 3.5: Spatial correlation function of particle velocities at different values of particle number, N, where maximum filling corresponds to N=75.

At $j = 0$, self-correlation equals to 1. $f(j)$ decays to zero and then converges to a constant negative value. The result shows that the correlations increase in spatial

range as more particles are added in the channel. The range of correlation is quantified by correlation length l_c. We choose two different definitions to quantify l_c. The first definition is based on the exponential decay ratio of correlation function $f(j)$. We fit the curves to function

$$f(j) = 1 - c + c\exp(-j/l_c) \tag{3.3}$$

where it starts from 1 and decay to $1 - c$ exponentially. Here l_c is the correlation length. We fit l_c for each density and plot them in Fig 3.6

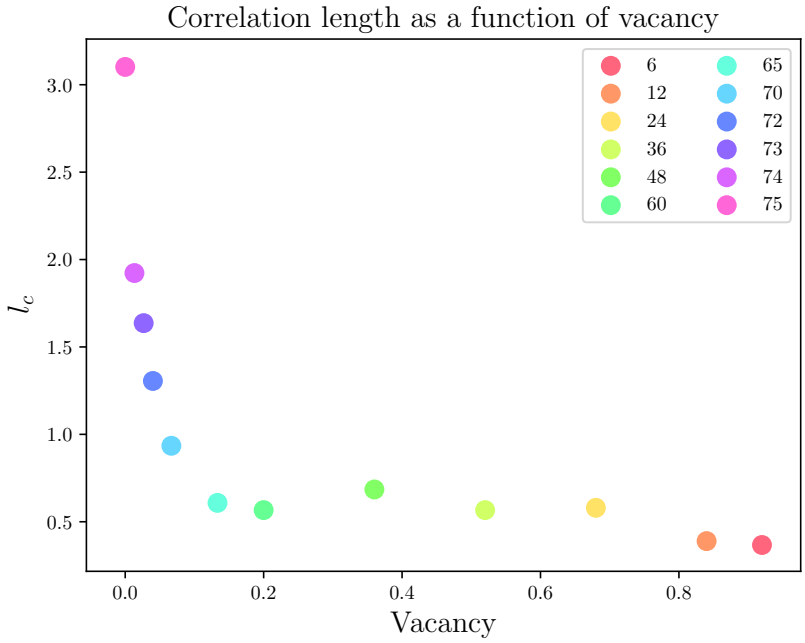

Figure 3.6: Correlation length l_c defined by exponential fit to two-point spatial velocity correlation function.

The second definition of l_c is the length at which $f(j)$ equals to zero. l_c can be extracted by interpolating each correlation curve. We plot the results in Fig 3.7. The correlation length l_c increases sharply towards maximum density. At a vacancy concentration $\phi_C = 0$, $l_c \approx 11$, which corresponds to nearly 1/3 of the particles. These two definitions qualitatively agree with each other. We also tested these results with a

smaller system size where $N_{max} = 29$ as shown in Fig 3.7.The result shows nontrivial dependence on system size.

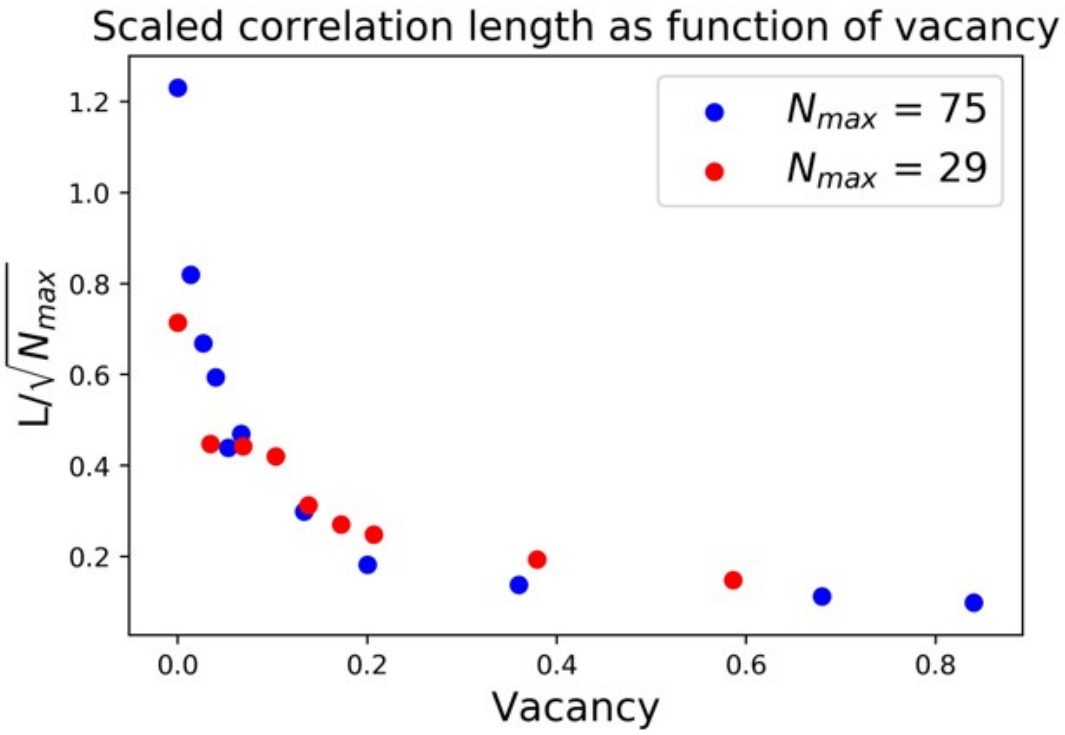

Figure 3.7: Correlation length defined by the distance at which the correlation drops to zero, i.e. $f_j = 0$. The figure shows two fully-filled rings of different size.

To understand whether these correlated spatial fluctuations are associated with slow dynamics, we also calculate the temporal correlation function $g(\tau)$ defined as:

$$g(\tau) = \frac{\langle\langle(v_i(t) - \langle v_i(t)\rangle)(v_i(t+\tau) - \langle v_i(t+\tau)\rangle)\rangle_i\rangle_t}{\langle\langle\sqrt{|v_i(t) - \langle v_i(t)\rangle||v_i(t+\tau) - \langle v_i(t+\tau)\rangle|}\rangle_i\rangle_t} \tag{3.4}$$

where time is in units of the inverse vibration frequency. The correlation at fixed time gap τ is averaged over all particle index i and then average over staring time t ranges from 0 to $t_{max} - \tau$. The curves(Fig 3.8) shows that the correlation is rapidly lost at the time scale corresponding to one shake. There is dip at two shakes corresponding to anti-correlated velocities. Then particles quickly converges to zero which indicates

that at all vacancy densities the particles lose their velocity memory within a short time scale.

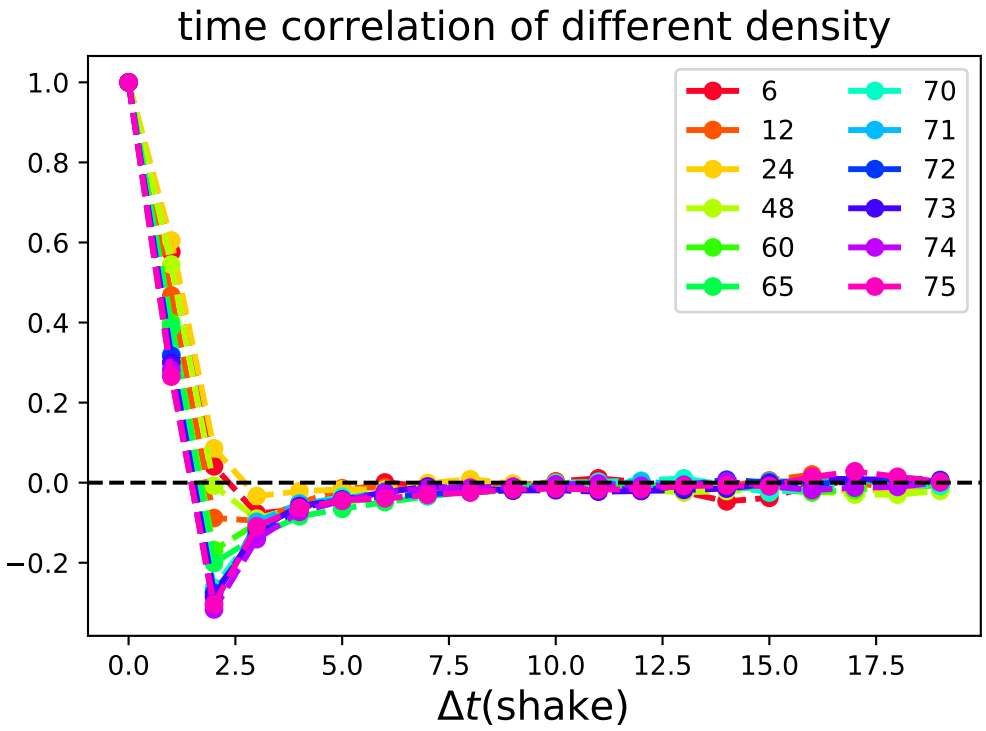

Figure 3.8: Average time correlation of velocity of single particle. The autocorrelation is shown for different levels of filling in a ring with maximum N=75.

We plot a velocity color-map at $\phi_V = 0$ or $N_{max} = 75$ to further investigate the spatial and temporal correlation (Fig 3.9). X-axis is particle index and Y-axis is time that goes to 200 shakes. Colors indicate the speed of particle as shown in legend. We also mark the color of single particle velocity $\frac{\sqrt{2}}{2}v_0$ when it 'walk' along the wall. Horizontal long lines with same color occupies around quarter of index axis shows the correlation length $l_c \approx 10$. The color map along the time axis (vertical direction) switches quickly proves the anti-correlation and absence of long-term memory along the time axis.

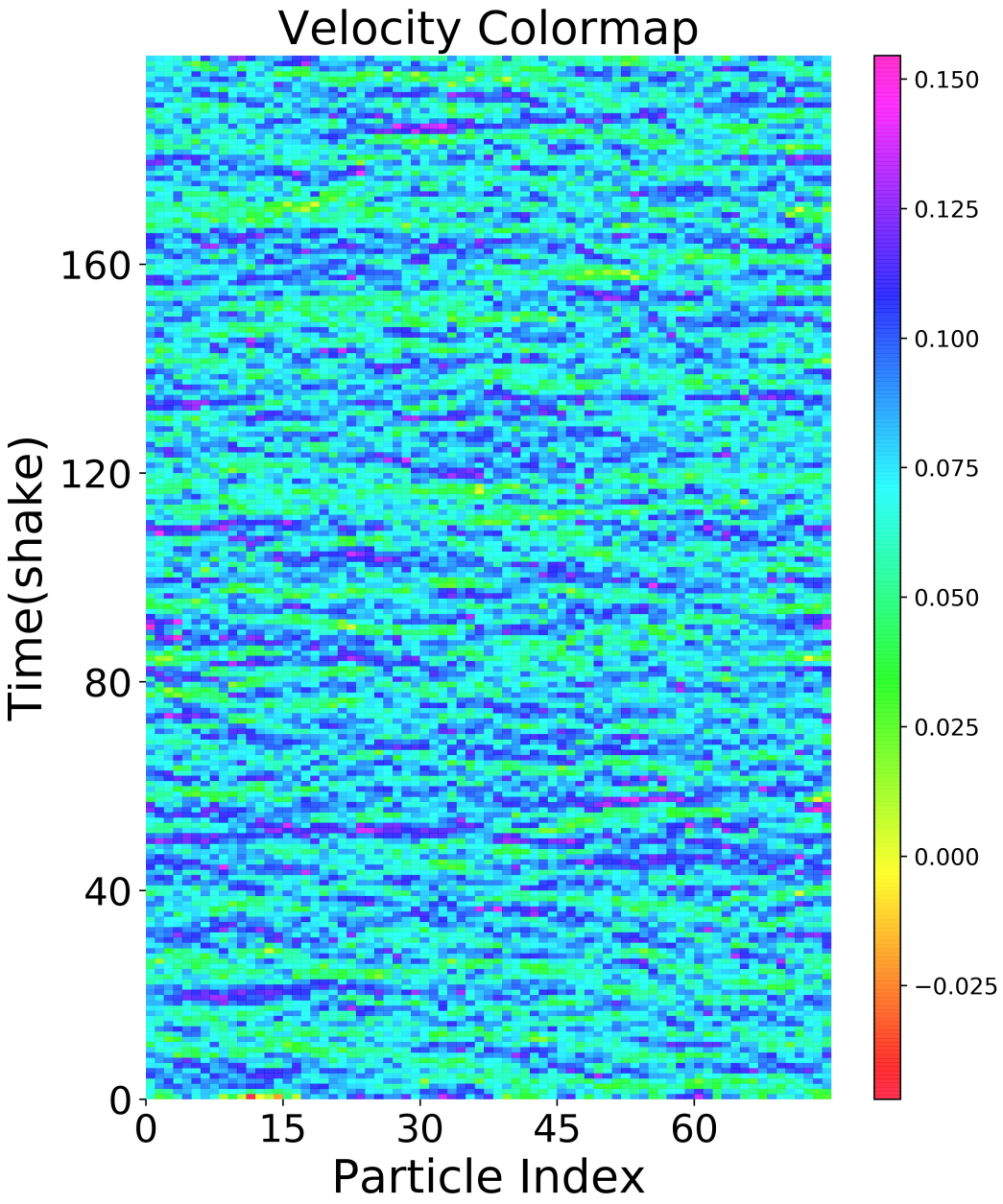

Figure 3.9: Velocity colormap when $N = N_{max} = 75$. The value of velocity is represented by the colorbar on the right. x-axis is particle index ranges from 0 to 75. y-axis is time in units of shaking frequency.

We have further results on the effects of varying vibration parameters such as frequency and amplitude, as well as results on the effect of two co-rotating or counter-rotating rings of particles which we will report in the thesis.

To summarize, the system develops long spatial correlations but not a long time scale. This is distinct from most traffic problems, and in general from other problems where slow kinetics develop due to interactions and disorder. The picture we have is of fluctuations arising from local noise in the shaking direction that get transmitted by long chains of collisions more or less within one collision period.

In addition, this is an illustrative toy example of activity and boundary-interactions being used to generate long-range transport from random initial conditions. One can easily imagine generalizations of this example where objects placed in a mechanically noisy environment are able to rectify this noise to move to a boundary or a guide structure, and spontaneously organize to move coherently along the boundary. One of the lessons learned from our example is that such a process might scale favorably. That is, a larger number of particles may indeed work more efficiently together.

CHAPTER 4

PHASE DIAGRAM OF SELF-PROPELLED SQUARES

In this chapter, we experimentally explore the 2-dimensional phase diagram of self-propelled hard squares by varying the activity of particles, l_P, and the occupied area fraction, ϕ, of the system. There is no other experimental phase diagram we are aware of. Therefore this is the first experiment to explore this field. The other significant feature of our work is that most work in active matter studies mobility induced phase separation[4] where clumping or condensation of particles occurs in regions of phase space where equilibrium particles do not condense. However, our work is focused on studying the effect of activity in regions of phase space where there is condensed matter even in equilibrium.

We first introduce one of the biggest challenges in experimental active matter system and how we solve it successfully by changing the dynamic behavior of particles. Then we report how we vary the persistence length l_p of our particles. At fixed l_p, we explore how the phase behavior of system changes with area fraction ϕ and how we characterize different phases.

By controlling the rotational noise of particles, we first solve a traditional hurdle in experimental probes of active phase diagrams, where particles that escape to boundaries are not able to return to the bulk. We find qualitatively new phenomena at finite l_P: a coexistence regime opens up between ordered state and fluid state; the phase boundaries of the coexistence regime evolve smoothly as a function of activity. Finally, at high enough l_P an ordered state appears at all area fractions. To supplement the experimental observations, and in particular, to assess the role of the

boundaries in the experimental geometry, we also perform simulations in the same parameter regime. The simulations agree qualitatively with the experiments, and further reveal new features of the ordered state.

4.1 Boundary Clumping

In experimental active matter research, one of the biggest challenge is boundary clumping. It is difficult to form a homogeneous long-term steady state with polar activity as polar particles approach the boundary of the system, and then get irreversibly trapped there. One example is the collective motion described in previous chapter where particles walking along the cell boundary. Similar observations have been found in other studies.

Kudrolli's work [14] found self-propelled polar rods with non-symmetrical mass distribution migrate and aggregate at the boundary of container. They found geometry of particles plays an important role. By changing the aspect ratio, system have a uniform distribution. My previous colleague Lee mainly focused on the noise and diffusion of dilute self-propelled particles[19] and melting process of well-ordered crystallite of granular particles[18]. The boundary limits the further exploration of steady state phase. Deblais [28] found inertial self-propelled robots have boundary clustering.

Researchers try to solve the boundary clumping by two strategies. The first is modifying the geometry of particles such aspect-ratio[29] and the other is by modifying the geometry of the boundary, Experiments [30, 31, 2, 32] have used flower-shaped walls[2] as a mechanism to inject wall-trapped particles back into the flow. When particles crawled along a 'petal' (Fig4.1), they are likely to be injected in the bulk when reaching the cusp point.

The flower-shaped walls successfully bring particles into the bulk. However, the cusp cause discontinuity in the boundary shape with possibly unknown effects on the

spatial heterogeneity of the system. Therefore, we are seeking another possible ways to avoid this kind of discontinuity. We achieve this effect by tuning the particle properties rather than the boundary conditions: in particular, we can tune the rotational diffusion constant so that D_R is large enough for particles arriving at the wall to have an appreciable probability of rotating and re-entering the bulk. (Another difference in our system is that the mobility axis of squares trapped at the boundary is not normal to the wall, as a result, the component of the mobility aligned with the wall enables particles to drift, rather than diffuse, along the wall.)

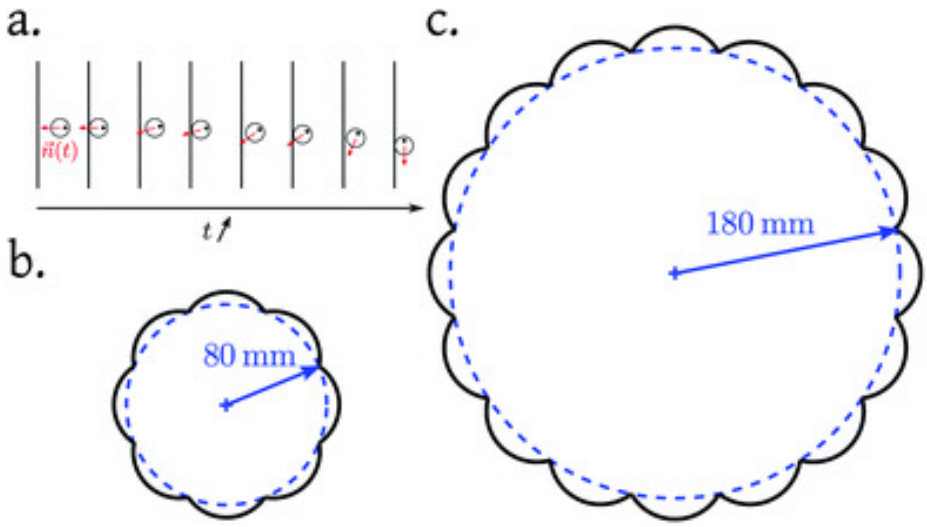

Figure 4.1: Flower-shaped boundary introduced in group of Dauchot[2]. The 'petals' enable particles to movebe injected back into the bulk of system.

4.2 Phases Of Isotropic Squares

Before we dive into how activity alter the order of particles, I present a brief review of work on hard square isotropic particles. There is a limited number of studies on the phases of squares and most of them are simulations.

Frenkel and Wojciechowski implemented Monte Carlo simulation on equilibrium hard squares suggesting a four fold tetratic orientational as well as translational order[33]. The orientational order shows a longer range than translational order.

Another simulation by Escobedo *et al.* indicate the importance of details of the particle shape[34]. They found with that squares with rounded-enough corners form hexagonal bond order, however sharper corners shows a tetratic order phase.

Experiments on square-shaped colloids shows isotropic liquid at low area fraction[9]. At higher ϕ the system assumes a "hexagonal rotator" phase where particles form hexagonal orientational bond order but no molecular order. This is caused by the rounded corners suggested by Escobedo *et al.* Beyond a threshold of ϕ, system forms a square lattice. This sensitivity to shape encourages us to use square shapes in our studies.

Experiments were performed to study phases of vibrated hard squares by my colleague Lee[18, 3]. The squares had cylindrical knobs on their top surface, which led to isotropic noise from collisions with the confining surface. The experiment shows a progression from an isotropic disordered fluid at low area fraction, to a fluid with orientational order, to a solid state with both translational and orientational order. At low ϕ, particles are positionally and orientationally isotropic. As ϕ increased, quasi-long-range four-fold tetratic orientational order and short-range translational order is observed in the fluid when $0.72 \lesssim \phi \lesssim 0.78$. When $\phi \gtrsim 0.77$, system turns to a quasi-long-range translational ordered solid state. This is consistent with the hard square phase diagram observed in the Monte Carlo simulations of Frenkel. NM]

4.3 Phase of Self-propelled Squares

In this section, we explore the phases of self-propelled particles as increasing ϕ. System develops from isotropic fluid to phase coexistence between fluid and ordered state and finally to a fully ordered state. The phase coexistence region is absent in the passive hard squares, which is caused by introducing non-equilibrium activity.

4.3.1 Isotropic Fluid

At low area fraction ϕ, particles form isotropic fluid due to high rotational diffusion D_R. One example of l_p is shown in Fig 4.2a . We calculated the radial distribution of center of particles in Fig 4.2b. Particles area fraction are uniform in all radius range which is a strong proof that high D_R successfully solve the boundary clumping problem.

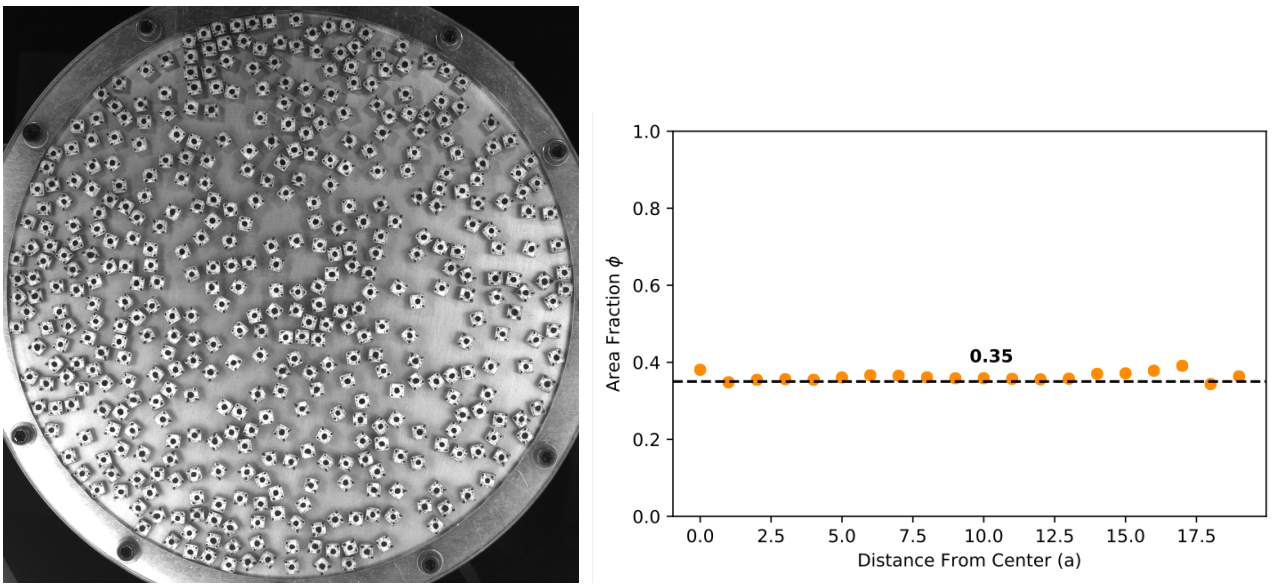

(a) (b)

Figure 4.2: (a) Snapshot of isotropic fluid when $l_p = 2.29$ and $N = 438$ or $\phi = 0.35$. (b) Particles spatial distribution along the radial direction. X-axis is the distance from center position. Y-axis is area fraction that particles fall in the radius range where $r_{in} = (x-1)a, r_{out} = xa$. Area fraction is averaged over time and normalized by the area of each channel $\pi(r_{out}^2 - r_{in}^2)$. The result shows that the fluid state is spatially homogeneous in the system.

4.3.2 Phase Coexistence

Beyond a threshold value of ϕ, some particles assemble into a high density region, usually nucleated at the boundary of the cell, while the rest of particles remain uniformly distributed in central area as shown in Fig 4.3. One of the most significant consequences of finite activity is the development of such a coexistence regime, where

none existed in the equilibrium phase diagram, as also observed in simulations of soft squares [35]. As the average area fraction, ϕ is increased, there are fewer and fewer particles in the low-density 'fluid' phase, until finally, the system is entirely in the ordered phase.

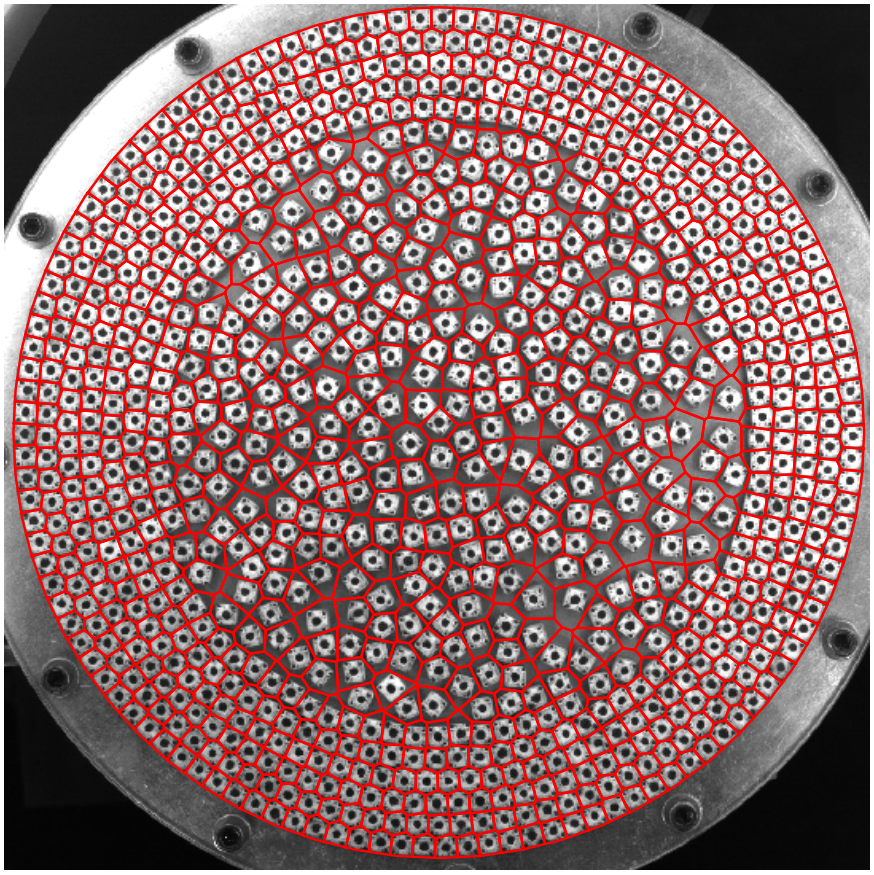

Figure 4.3: Phase coexistence between high-density ordered phase near the wall and isotropic liquid in the bulk when $N = 900$, $\phi = 0.72$. Red lines marks the Voronoi cell of each particle.

For the coexistence regime, we show in the lower panel of Fig 4.4 four measures of the contrast between the fluid phase and the ordered phase, via the rotational velocity, the radial velocity ,the local density, and the orientational molecular ordering, respectively. In Fig 4.4(a), we contrast the lower rotational mobility of particles in the ordered phase compared to those in fluid phase. We characterize this mobility

by plotting $v_\Omega = v_\omega - v_\theta/R$ where v_ω is the short-time rotational velocity described earlier, and the latter term removes the azimuthal linear velocity associated with slow global rotation of the ordered phase along the boundary wall (θ direction is defined in Fig 2.1). Fig 4.4(a) indicates that rotation in the high density region freezes, while particles in the fluid phase rotate freely. Fig 4.4(b) suggests that ordered particles not only has low rotational mobility but also low translational mobility. System is symmetric to the center of cell so that the average radial velocity of all particles is close to zero. The third figure, Fig 4.4(c), shows a measure of local density, with a Voronoi tessellation overlaid on the particles, colour-coded by the magnitude of the Voronoi cell area, normalized by the cell area of a close-packed set of particles. Here, the high-density region has a normalized local area fraction close to 1, and the other region remains homogeneous with a fraction close to 0.5. Finally, in Fig 4.4(d), we plot the local tetratic orientational order of the particles defined through Φ^4 (Fig 4.4(d)),

$$\Phi^4_k = | < e^{i4\gamma_j} >_j, j \in V_k \cup k| \tag{4.1}$$

where k is a particle index, and V_k is the set of its Voronoi neighbours. Once again, there is a large contrast in tetratic order, Φ^4, between the particles in the fluid and the ordered phases.

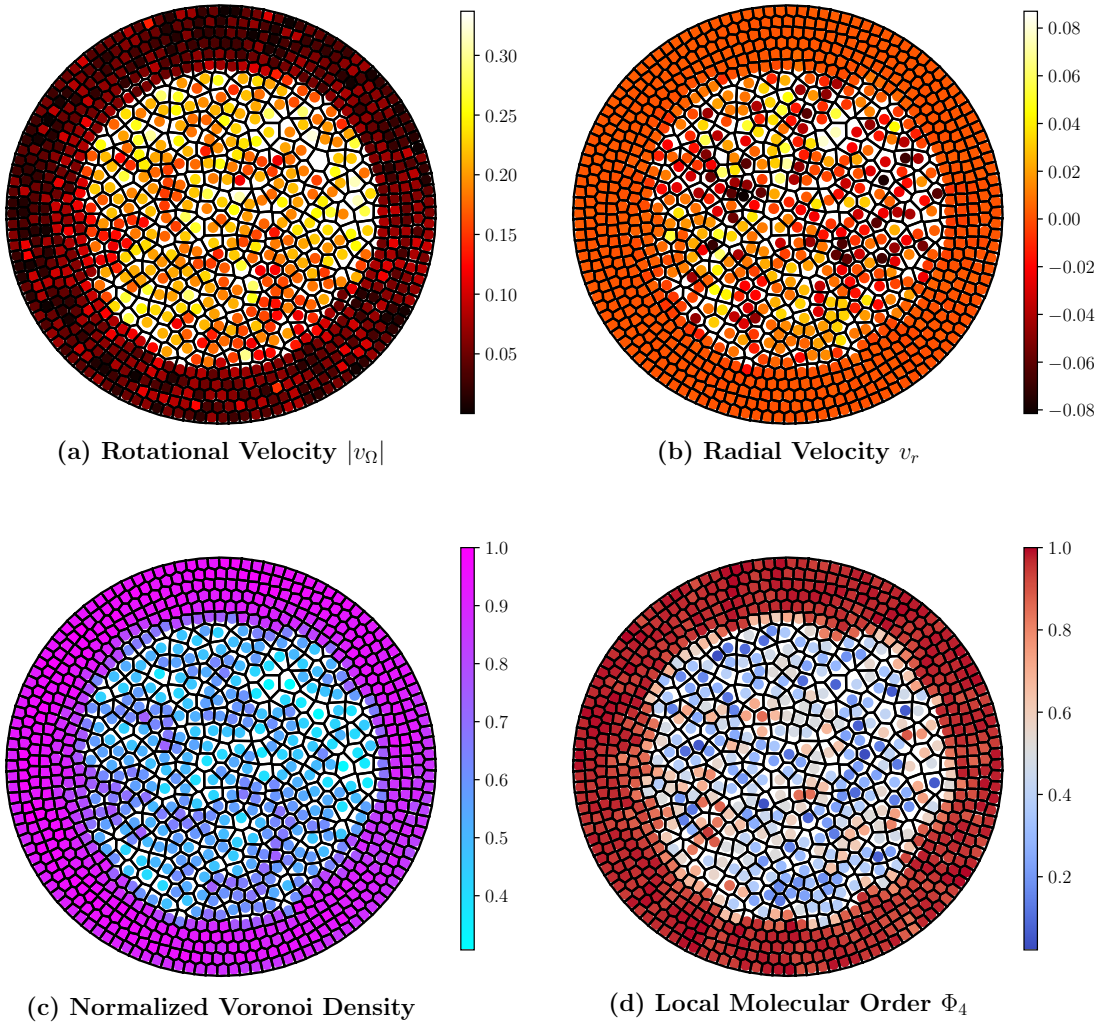

(a) Rotational Velocity $|v_\Omega|$

(b) Radial Velocity v_r

(c) Normalized Voronoi Density

(d) Local Molecular Order Φ_4

Figure 4.4: (a)-(d) Absolute value of rotational velocity, radial velocity, normalized Voronoi density and local tetratic orientational order of the configuration in Fig 4.3

4.3.3 Detection of Phase of Particles

From these data, we infer that local density, local tetratic orientational order, and single-particle mobility all serve to distinguish two phases. In what follows, we use single-particle mobility as a convenient criterion to identify particles that are fluid, ordered, or at the interface.

To get information on short-time dynamics of particles, we record the motion of particles at 125frames/s in bursts of 20 vibration periods. To get good statistical

averages of the steady-state behaviour, we take 200 statistically independent configurations of the system, by spacing these bursts of data with a gap of 250 vibration periods between each configuration.

We check the position and orientation series of each particle. Due to the fact that position of each particle is 100% correctly detected, if orientation of a single particle is missing in all the 20 vibration periods that particle would be discarded. In the next step, we calculate the mean value of $\langle v_r \rangle_t$ and absolute value of $\langle |v_\Omega| \rangle_t$ within 20 vibration periods in each configuration. To be in ordered states, particles need to satisfy the following criteria:

1. There are at least two neighbor particles within $1.5a$ radius.
2. $\langle |v_\Omega| \rangle_t$ must be smaller than a threshold where we choose $0.12 rad/shake$
3. $\langle v_r \rangle_t < 1.5 std(\langle v_r \rangle_t)$. System is symmetric so that average over all particles indicate $\sum_{i=1}^{N} (\langle v_r \rangle_t)_i \approx 0$.
4. Three of neighbor particles need to satisfy previous requirement.

The dynamical and structural requirements are sometimes too strict so that we manually introduce false negative examples. In order to fix the errors, we loop over non-ordered particles. If more than 5/6 nearest neighbor particle are ordered, we set it to ordered particles. We run this loop twice to eliminate consecutive false negative examples. The detected ordered particles are shown in .

We also identify interfacial particles between ordered and fluid particles. The interfacial particles are identified by studying neighbor particles: if more than a quarter the neighbours of a fluid particle are ordered particles, then it is relabelled as an interfacial particle, and if an ordered particle has more than 2 fluid neighbors, it is labelled as an interfacial particle. The detected phases are plotted in Fig 4.5. Green particles are in fluid state, brown ones are in solid state and yellow ones are interfacial particles.

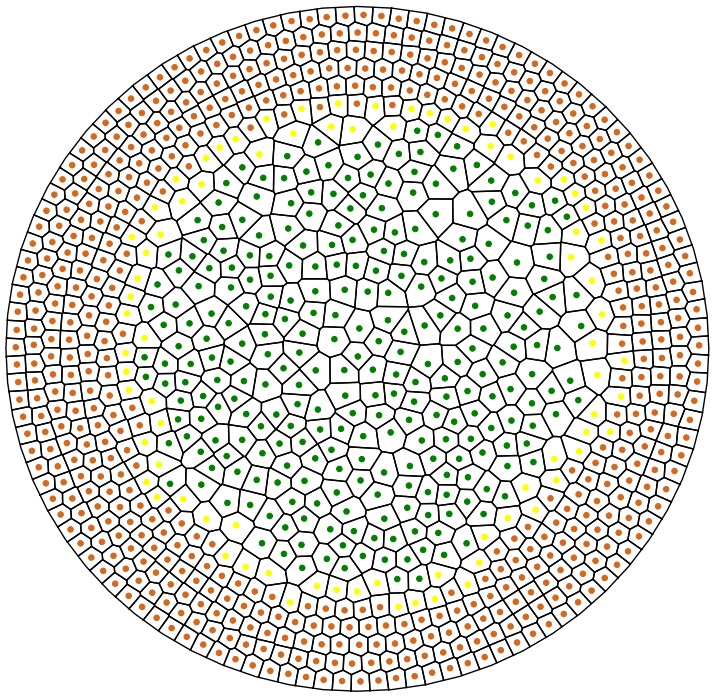

Figure 4.5: Detected phases in Fig 4.3 based on dynamic behavior and neighbor particles: green-fluid, yellow-interfacial particles, brown-ordered particles. The detected ordered state matches perfectly with the molecular order in Fig 4.4(d).

4.3.4 Fully Ordered State

As area fraction ϕ keeps increasing, more particles freeze into ordered state and less particles move freely. At certain ϕ, only few particle(< 0.01) could move in the limited open area. Those particles would be identified as interfacial particles(Fig 4.6(c)) due to our detection algorithm. One example of configuration and it's corresponding orientational tetratic order Φ_4 when $N = 1150, \phi = .92$ and $l_p = 1.25$ is plot in Fig 4.6. At high area fraction, there is defect in the ordered state due to limitation of free space. The tetratic orientational order correctly identified the defect in the ordered states.

The maximum ϕ we can reach is 0.92 due to constraints of geometry and size of particles as well as boundary. When $\phi \gtrsim 0.7$, we are no longer able to distribute

particles uniformly with random orientation. We have to manually make particles close packed so that we introduce certain order to the system. If there is enough space in the system($\phi \lesssim 0.85$), particles could reorganize both their positions and orientations. Otherwise, only some particles could fill defects in the ordered states.

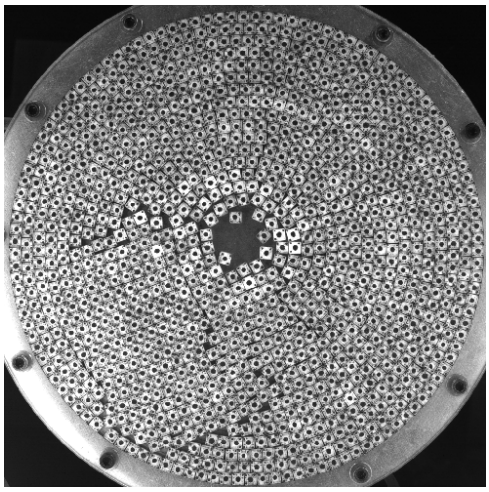

(a)Snapshot of Configuration

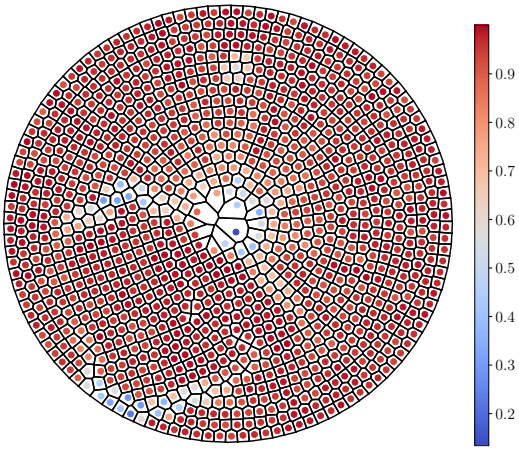

(b) Local Molecular Order Φ_4

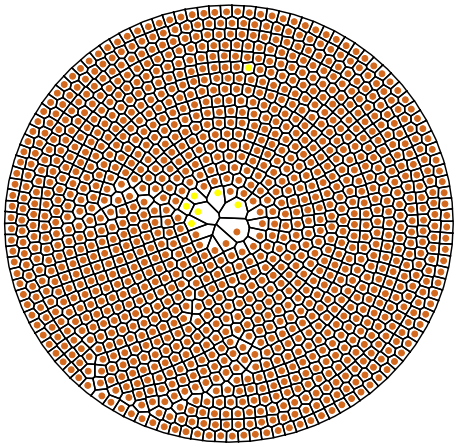

(c) Phase Detection

Figure 4.6: (a)Snapshot of stable fully ordered state when $N = 1150, \phi = 0.92$ and $l_p = 1.25$. There are defects in the ordered state at the left middle and bottom part. (b) Tetratic orientational order Φ_4 shows the defects and indicates the system has frozen into a fully ordered state. (c) Identification of particle phases. All but a few particles are identified as solid (brown) with a few interfacial particles (yellow), one of which There is one interfacial particle on the top area due to wrong orientation detection(as shown in (b) by Φ_4). Since this particle is identified as interfacial, it does not affect the computed statistical behavior of ordered particles.

4.4 Phase Diagram of Self-propelled Squares

Previous work on hard equilibrium squares [34, 33, 3], show fluid, orientationally ordered, and translationally ordered phases. Experiments [9] and simulations [34] indicate squares with sufficiently rounded corners additionally form a hexagonal rotator phase, whereas squares with sharper corners show indications of a tetratic-like phase before crystallization. However, the appearance of phase coexistence between a mobile, fluid phase and a dense, low-mobility, ordered phase is an effect purely due to nonequilibrium activity.

These nonequilibrium phase boundaries vary with l_p: in (Fig. 4.7), we construct a phase diagram by varying the activity of our self-propelled squares and the area fraction ϕ. Equilibrium squares [3] form an isotropic fluid when $\phi \leq 0.72$, then develop tetratic orientational order for $0.72 \leq \phi \leq 0.77$, and finally, make a transition to translational order for $\phi \geq 0.77$. We explore phase behaviour as a function of area fraction, for four different values of $l_p = 0.75, 1.25, 2.29$ and $5.7a$. Regions of phase space are identified as fully ordered (blue), or fluid (red), with an intermediate coexistence region (green) based on the number of particles in the ordered phase (N_O), as a fraction of the total particle number, N: $n_O = N_O/N$(Fig. 4.9(a)). We indicate a fluid state (red) when $n_O < 0.05$, and an ordered phase when $n_O > 0.95$. Realizing that this is a criterion-dependent definition, we leave the phase boundaries blurred. We note the tendency to order increases, as does the width of coexistence region, when activity increases. For our largest activity, $l_p = 5.7$, activity dominates the ordering and particles always condense into an ordered state at even the lowest density that we explore.

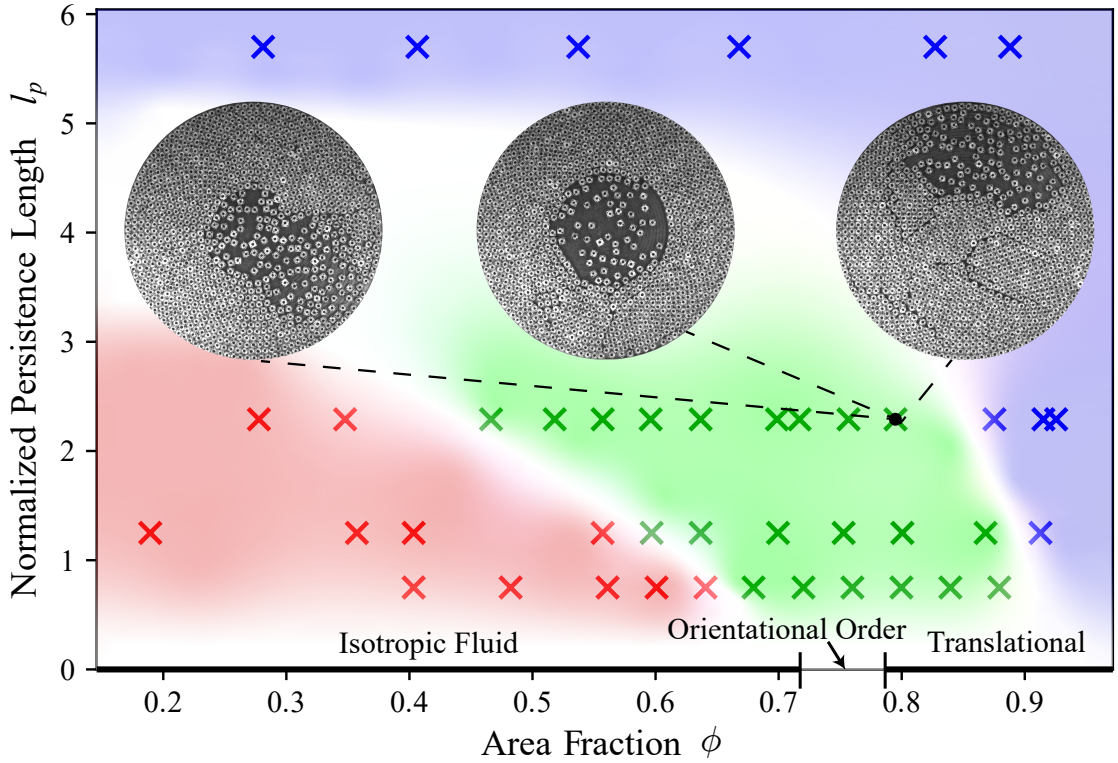

Figure 4.7: Phase diagram in the l_p vs ϕ plane. The phases at zero activity correspond to Ref. [3]. The crosses are our results with four different l_p. Red region indicates isotropic fluid, green region is the phase coexistence region and the blue region indicates fully ordered state. Three snapshots when $l_p = 2.29$ and $\phi = 0.79$ demonstrate that considerable global rearrangements can occur over time, and the pocket of fluid phase can migrate away from the centre of the system and approach the boundary.

We do not have sufficient statistics to study the nature of these transitions. But the number of particles in different phases may give some hints to further study when fluid turns into coexistence. We investigate the number variance of fluid particles normalized by total number as a function of ϕ in the 200 configurations(Fig 4.8). When phase coexistence starts, the fluctuation has a sharp increase. However, we do not have enough data to predict the exact transition point. When $l_p = 1.25$ and $\phi = 0.75$ the number fluctuation also has a peak. The data video shows the peak comes from the transition between ordered particles and fluid particles. This is clearly not a critical point but with a high fluctuation.

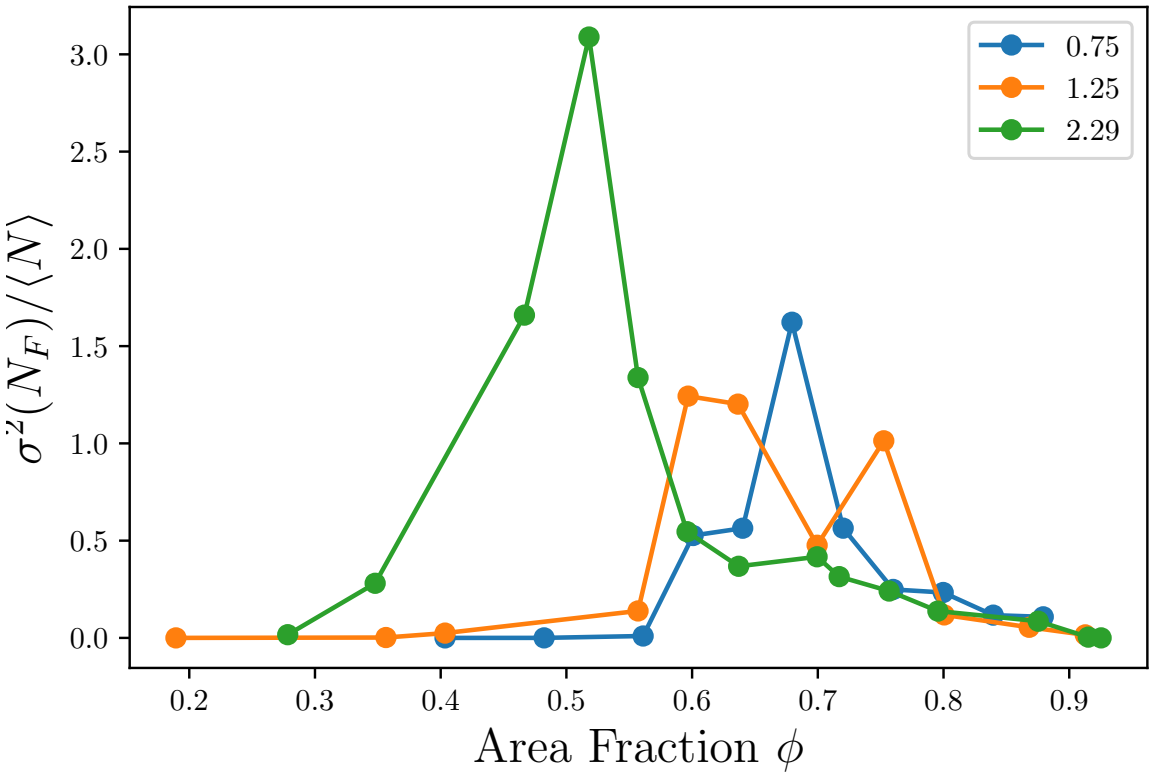

Figure 4.8: Normalized fluid number variance $\sigma^2(N_F)/N$ as a function of area fraction ϕ

Qualitatively, we find reasonable agreement with the simulations of Prymidis *etal.* [35]; their particles are soft squares with effectively rounded corners in the interaction and therefore may correspond to a different equilibrium phase [34]. And yet, they

discover coexistence in a system with four-fold interactions. The trends of the phase boundary are similar in our experiment though quantitative details are different: the density of our ordered phase is higher and the fluid phase lower, however, this is not surprising given the difference in the interaction potential. Perhaps because we are able to go to higher total volume fractions, we are additionally able to find the end of the coexistence region, where the entire system is in the ordered phase. Importantly, this suggests the high-l_p solid phase is smoothly connected to the equilibrium and low-l_p phase. The phenomenon of oscillation between the solid and fluid phases was not observed in our system, serving as a reminder that some nonequilibrium effects can be closely linked to the type of activity.

It is natural to ask whether the coexistence regime is due to the presence of boundaries. Indeed, it is true that the ordered state more easily nucleates near the boundary. However, we argue that phase coexistence phenomenon is not purely a boundary effect since it is not always true that the ordered state is at the walls and the fluid state is in the interior of the cell; this in illustrated in the insets of Fig 4.7, which show states of the system at different instants in time over a period of one hour. (We later revisit the role of the boundary via simulations.) The ordered state is not locked in time, and there are slow global drifts of radial layers of particles. These layers do not move in registry, so defects can collect or can escape, enabling the system to rearrange.

To map out the coexistence region, we track the fractions of particles in the fluid, n_F, and ordered states, n_O, as a function of ϕ (Fig. 4.9) (a). $n_F + n_O + n_I = 1$, where n_I is the fraction of interfacial particles. As is evident in Fig 4.9), the starting point of phase coexistence changes with activity: n_O becomes nonzero at $\phi \approx 0.4, 0.55, 0.65$ for $l_p = 2.29, 1.25, 0.75$, respectively. The terminal area fraction of the coexistence region varies with activity as well. At the highest activity of $l_p = 5.7$, particles always migrate to the wall and form layers of ordered particles so that $n_F \approx 1$ at all values

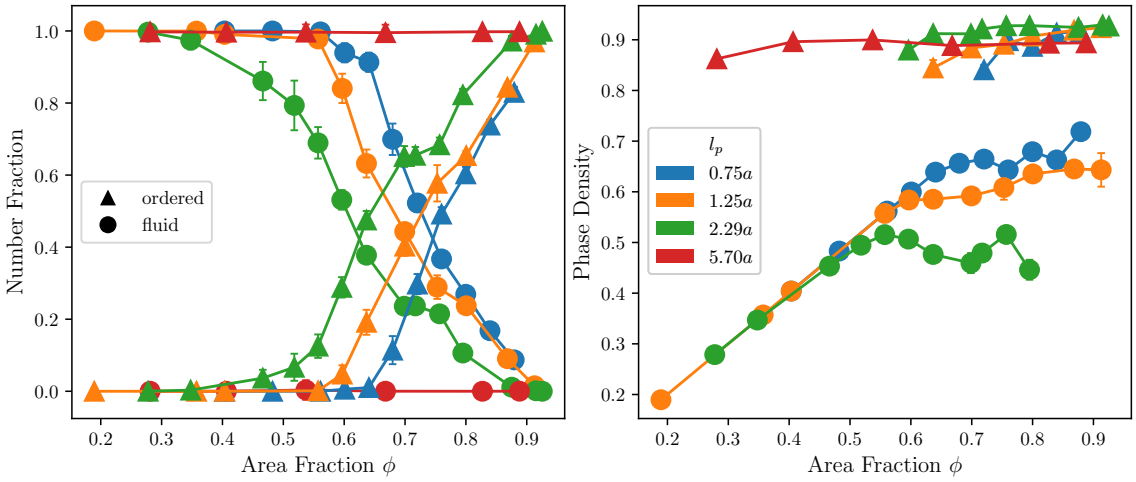

Figure 4.9: (a) Number fraction of ordered and fluid particles as function of area fraction ϕ. Phase coexistence starts where the ordered number fraction, n_O, becomes nonzero or the fluid number fraction, n_F, departs from one. The onset of phase coexistence moves steadily to lower density with increasing activity. (b) Phase densities of ordered and fluid states. The fluid density ϕ_F increases linearly with ϕ then fluctuates around a constant value when phase coexistence starts. Higher activity leads to lower coexistence ϕ_F.

of ϕ. We emphasize that all these data are taken in steady state, and n_F and n_O have been tracked for periods of thirty minutes (i.e. 1.5×10^4 vibration periods).

In Fig. 4.9 (b) we display the densities of the phases defined through $\phi_S = \sum_{i \in S} a^2 / \sum_{i \in S} A_{Voronoi}$, where the sum is over all particles in phase $S \in O$ or F, the ordered or fluid phases. Once the ordered state appears, the density of the phase remains high, with ($\phi_O \approx 0.9$). At a given activity, ϕ_O in the fully ordered state is slightly higher than ϕ_O in phase coexistence. The fluid density ϕ_F increases linearly with ϕ before phase coexistence, then becomes nearly constant. At fixed ϕ, increase in activity leads to a lower fluid density.

In Fig. **??** we display measures of orientational ordering. In addition to the tetratic orientational order, we also calculate a bond-orientational order

$$\Psi_k^m = | < e^{im\theta_{jk}} >_j |, j \in \mathcal{V}_k \tag{4.2}$$

where θ_{jk} is the bond angle between particles j and k, and $\mathcal{V}_k$ represent the m nearest Voronoi neighbours of particle k. In Fig. **??**(a) we show that the 'molecular' orientational order Φ^4 is well-developed at the onset of coexistence and remains high, with a slight decline at the very highest densities due to the appearance of defects when the cell is nearly filled with the ordered phase. In principle, bond-orientational order depends purely on translation degrees of freedom, and is insensitive to the orientations of particles, however, as previously observed in passive squares [3], molecular orientational order is accompanied by bond-orientational order at high densities, likely due to steric constraints. Both four-fold and six-fold bond order are appreciably large in the ordered state, but Ψ^4 increases with ϕ (Fig 4.10(a)) whereas Ψ^6 decreases with ϕ (Fig 4.10(b)). In general, Ψ^4 and Φ^4 follow the same trends as they do in passive squares, but show higher levels of ordering [3]. The influence of the circular boundary in causing layering of the ordered, high-density state, makes it difficult to ascertain whether the orientationally ordered state makes a transition to a translationally ordered state.

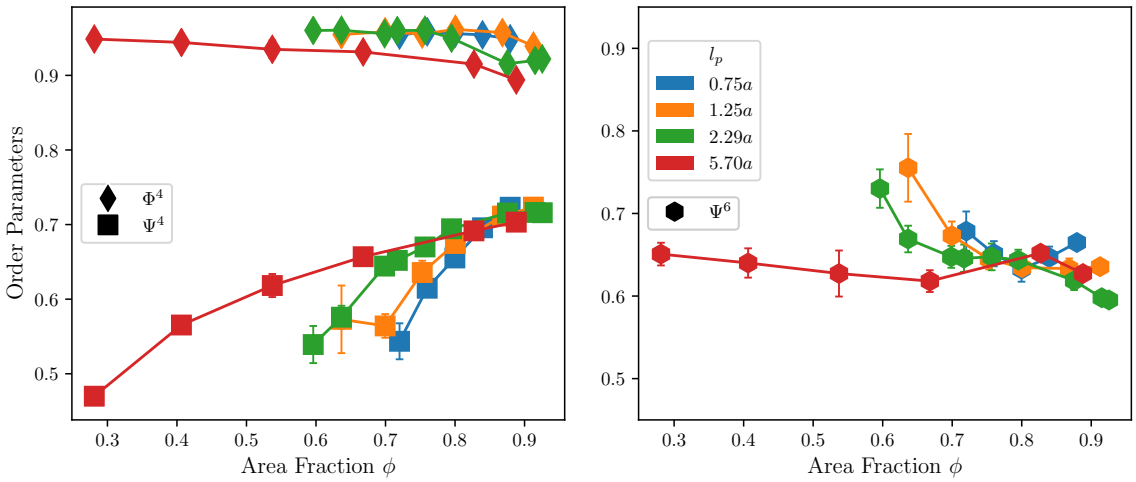

Figure 4.10: (a) Tetratic orientational order Φ^4 and tetratic bond order Ψ^4 of ordered state. Φ^4 decreases at high ϕ due the appearance of defect. Ψ^4 increases gradually with ϕ(b) Hexatic bond order Ψ^6 of ordered states. Ordered phase has both Ψ^4 and Ψ^6.

4.5 Kinetics of Phase Formation

In addition to the new phases caused by non-equilibrium activity, we find the process of formation of ordered state is interesting. When the area fraction ϕ is higher than 0.6, particles quickly (within 6000 vibrations or 2 minutes) migrate to the boundary and form ordered state characterized by high Φ_4 and Ψ_4. However, it takes relative long (from 45,000 vibrations/15 minutes to 180,000 vibrations/60 minutes) to form a final stable ordered state when ϕ is high. In this asymptotic state almost all particle within ordered state maintain their relative position and neighborhood. We show four snapshots of ordered particles Fig 4.11 to illustrate the kinetics of evolution when $l_p = 1.25$ and $\phi = 0.67$. Particles in the ordered phase that are polarized with a velocity component pointing toward the fluid interface, escape the solid and return to the fluid, while new particles from the fluid attach to the solid. This process of increasing polarization in the ordered phase is extremely slow, as incorrectly oriented particles in the solid phase cannot escape if they are surrounded by particles oriented away from the fluid.

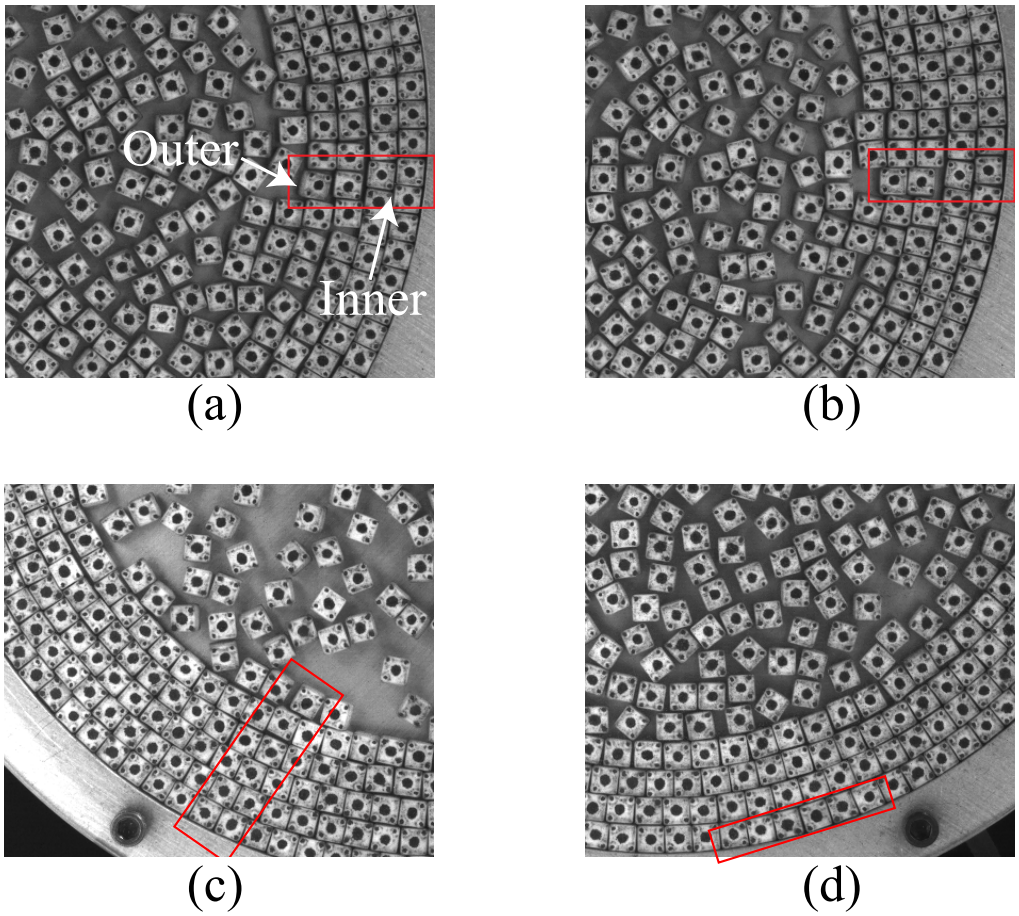

Figure 4.11: Evolution of ordered state. We label ordered particles close to the cell boundary 'inner' particles and the ordered particles in contact with the fluid as 'outer' particles. (a) The red box shows inner particles have polarization component along the $-\vec{r}$ direction when the ordered state is not stable. (b) After 10 vibration periods, misaligned outer particles tend to escape from the ordered state. The gap could be filled by correctly oriented fluid particles or enable the inner trapped ordered particles to leave. (c) The ordered state is stable if there are more particles aligned along $\vec{r}$ direction than along the $-\vec{r}$ direction. Particles in red box are likely to escape and reorganize themselves. (d) Snapshot of stable ordered state. Even if inner particles in red box try to escape, they are surrounded by particles aligned along $\vec{r}$ direction. Therefore the configuration is stable.

Therefore, we need another order parameter to quantify the polarization along radial direction in addition to Φ_4 and Ψ_4. We define p to quantify whether one component of particle's mobility is aligned with radial outward or inward direction:

$$p = \mathbf{sign}(\vec{r} \cdot \vec{v_l}) \tag{4.3}$$

$\vec{r}$ is position vector of particle, $\vec{v_l}$ is longitudinal velocity. We used the fraction of positive p (outward-pointing) among the ordered particles to evaluate how ordered particles are aligned.

$$\pi = \frac{\sum_{i=1}^{N_O} \delta_{p_i=1}}{N_O} \tag{4.4}$$

The evolution of pi and ordered fraction when $\phi = 0.69$ and $l_p = 2.29$ are plotted in Fig 4.12. Particles are uniformly distributed with random initial orientation. These curves indicate that the polarized fraction increases gradually while the ordered number fraction quickly converges and fluctuates. We cannot capture the saturation of polarization due to the limitation of memory size of camera.

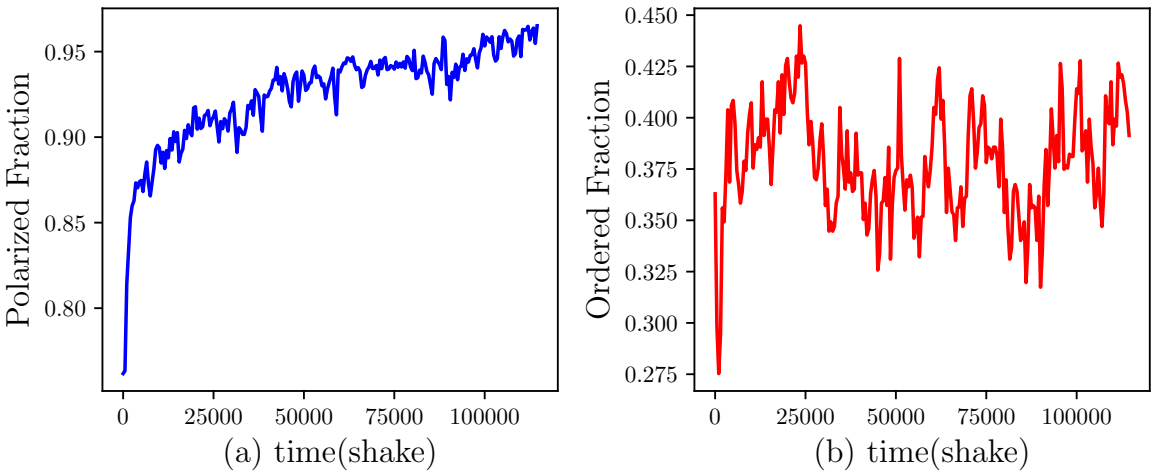

Figure 4.12: (a) Time evolution of polarized fraction when $\phi = 0.69$ and $l_p = 2.29$. The initial value is not close to 0.5 since data is taken a few seconds after vibration starts. It increases sharply in a short period then gradually until converges. (b) Time evolution of ordered particle fraction. It increases sharply when vibration starts then fluctuates. The results show that ordered state forms very quickly but internal ordered particles rearrange themselves to form a polarized ordered state.

The other interesting observation is there are some large, fully polarized clusters within the ordered state. These are only observed when $l_p >= 2.29$ as well as $\phi \geq 0.89$. Therefore, these observations were only accessible at two points in our experimental

phase diagram. However, a similar phenomenon is observed in simulation; the relevant details are explained section 4.6. Particles in fully polarized cluster are similarly oriented and are spatially connected as shown in Fig 4.13.

We used the depth-first search(DFS) algorithm [36] to identify the polarized clusters and group particles by their orientations. We first constructed a Voronoi neighbor dictionary where key is the index of particle and values are indexes of neighboring particles. The DFS algorithm starts from any unvisited particle (p_i) and checks whether its neighbor (p_j) is also unvisited and have similar orientation (absolute difference smaller than a threshold α_t). If this condition is satisfied, p_i and p_j belong to the same cluster and we repeat the previous process from p_j. Otherwise, we assign p_j to a new cluster. assigning all particles, we sort the clusters by thAftere number of contained within them and find the four largest clusters. (Our choice of four clusters matches the tetratic symmetry of square). As shown in Fig 4.13, the orientations of the largest four clusters match the four-fold symmetry.

However, the size of the detected cluster is criterion-dependent. In Fig 4.13, each column has different orientation threshold, $\alpha_t = 0.08$ and $\alpha_t = 0.12$. The result shows that same configuration has different cluster assignment with different α_t. In Fig 4.13(c), blue and red are two separate clusters when $\alpha_t = 0.08$ while they merge into one cluster when $\alpha_t = 0.12$. Therefore, the cluster size can depend strongly on α_t in some instances. Fluctuation of orientation of a single particle can lead to different cluster assignment especially if the particle joins two parts of a cluster connected by a thin region.

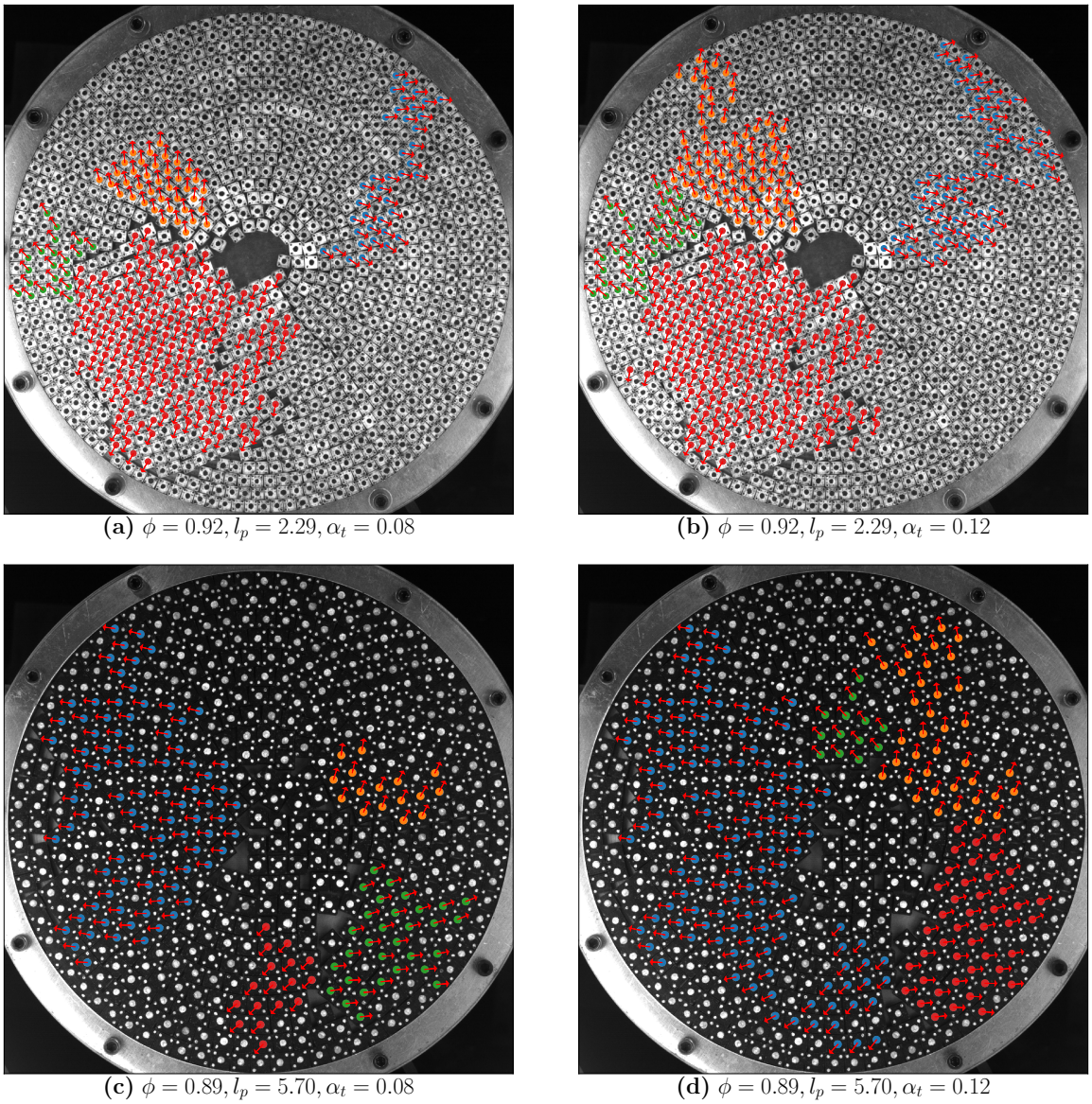

(a) $\phi = 0.92, l_p = 2.29, \alpha_t = 0.08$ **(b)** $\phi = 0.92, l_p = 2.29, \alpha_t = 0.12$

(c) $\phi = 0.89, l_p = 5.70, \alpha_t = 0.08$ **(d)** $\phi = 0.89, l_p = 5.70, \alpha_t = 0.12$

Figure 4.13: The four largest clusters observed in two different scenarios. (a) and (b) are identical snapshots when $\phi = 0.92$ and $l_p = 2.29$. The only difference between them are the orientation threshold α_t used to identify whether adjacent particles belong in the same cluster. Particles assigned in the same cluster are labelled by the same color. (a) and (b) show that cluster assignment depends on α_t. (c) and (d) are identical snapshots when $\phi = 0.89$ and $l_p = 5.70$.

4.6 Simulation

In order to test whether the phase coexistence observed in our experiments is purely due to the boundary and in order to more broadly complement our experi-

ments, we performed simulations on polar hard squares that share the same dynamical parameters as those in the experiment.

To eliminate potential effects of the wall, we worked with periodic boundary conditions. We place squares with unit side length in a virtual square box. The total number of particles in the simulation box is fixed at 2000. The side length of the box is adjusted to produce the desired area fraction $l = \sqrt{2000/\phi}$. The code is written in c++. Details of the simulation are described in the following subsections.

4.6.1 Initialization

At area fractions $\phi \leq 0.5$, we add particles sequentially in the simulation box with random positions and orientations, rejecting choices that overlap with squares already in the box. When the total number of particles reaches 2000, we stop the initialization.

When $\phi > 0.5$, this process becomes prohibitively slow. Therefore, we initialize particles on a square lattice. The number of particles on each column is $1/\sqrt{\phi}$. We add Gaussian noise to the positions of particles and impose a uniform random orientation on each particle. We iterate this process until we reach an initial condition with no overlap. With this method, though the orientations are random we introduce tetratic bond order in the initial condition. We find as long as the mean value of longitudinal displacement $v_0\delta t$ in a single step is smaller than average spacing between particles, the system will not locked by initial condition when $\phi \leq 0.7$. We haven't further explored it with $\phi > 0.7$.

4.6.2 Simulation Model

We define a loop as an iteration through all 2000 particles in the box, sampled in random order, in which we attempt a step of the stochastic dynamics described below. After initializing the system, we run $N_{sim} = 120,000 \sim 200,000$ loops. In each

loop, the dynamics of a single particle and the interaction between particles follow the rules described in this section.

We artificially make the model as if the trial particle has much smaller mass and momentum than any other particle. The momentum is not conserved in the interaction and there is momentum transfer between particles.

4.6.2.1 Dynamics

The time evolution of a single square located at $\vec{r}(t)$ with orientation $\gamma(t)$ at time t follows the Active Brownian Particle (ABP) model

$$\begin{cases} \dot{r}(t) & = v_0\hat{n} + \vec{\eta}(t) \\ \dot{\gamma}(t) & = \xi(t) \end{cases} \tag{4.5}$$

that we introduced in Chapter2. $\eta(t)$ and $\xi(t)$ are both Gaussian distributed random variables with zero mean, and no spatial or temporal correlations. We need to specify four dynamic parameters for the model: v_0, D_R, D_T and D_0. D_0 is the translational diffusion along longitudinal direction (i.e. the active diagonal along which v_0 is aligned) and D_T is the translational diffusion along transverse direction. $D_T = 0.005$ and $D_0 = 0.00424$ in the simulation, as in the experiment. The variance of $\xi(t)$ is $2D_R$, the variance of $\vec{\eta}(t)$ in the longitudinal direction is $2D_0$ and in the transverse direction is $2D_T$.

At time-step t, we first update the position along the orientation direction $\gamma(t)$ according to the ABP model: $r(t+1) = r(t)+\dot{r}(t)\hat{n}(t)$ and then update the orientation with $\gamma(t+1) = \gamma(t)+\dot{\gamma}(t)$. Whether this update is accepted depends on the interaction between particles.

4.6.2.2 Interaction

Since our system is composed of hard squares, the potential between two particles is

$$\begin{cases} \infty, & \text{if squares overlap} \\ 0, & \text{if there is no overlap} \end{cases} \tag{4.6}$$

Therefore, a square can move freely until it gets blocked by another particle. When we propose a move $(\dot{r}, \dot{\gamma})$ for a test particle, we check whether the new position and new orientation would cause overlap with other existing particles. If the attempted motion does not cause any overlap, we accept the move and update the corresponding position and orientation. If it leads to overlap, we do not reject the movement immediately but rather propose other two possibilities. In light of the fact that the particles in the experiment can slide past each other along their faces, if our model square is blocked in the first attempt we try to mimic the behavior in experiment. Therefore, we project the motion on $\gamma + \pi/4$ and $\gamma - \pi/4$ axis. The projected component is proposed with equal probability to prevent introducing chirality artificially. If the motion along the chosen component does not cause an overlap, we accept it and update the corresponding parameters. Otherwise, we try the other component. If all three possibilities are rejected, we give up the trial and leave the particle unchanged in this loop. One example of attempted motion is illustrated in Fig 4.14.

4.6.3 Implementation

In this section, we describe the engineering logic behind the physics of simulation. We define a square object to simplify the updating process, implement a computational geometry algorithm for overlap detection, and adopt Axis-Aligned Bounding Box tree to improve the efficiency of overlap query.

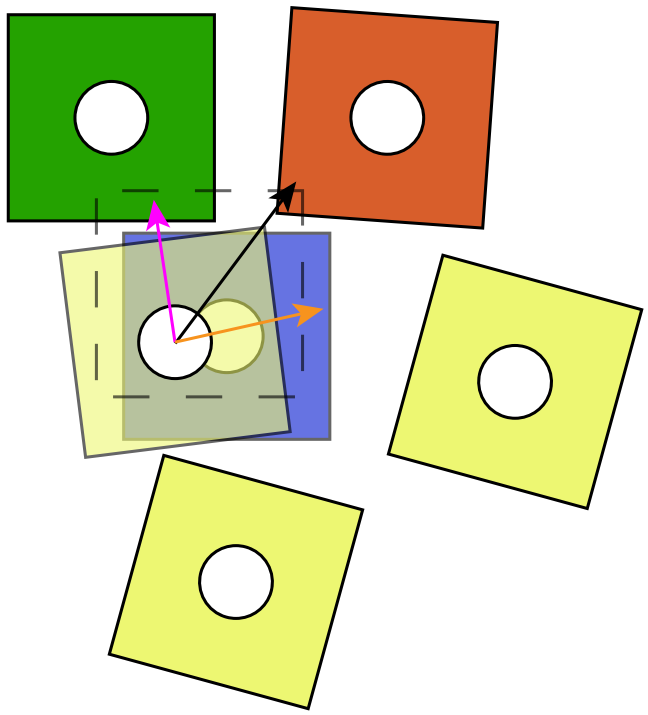

Figure 4.14: Example of attempted motion. The transparent yellow particle tries to move. The particle is located at x_o, y_o with orientation γ_o. The attempted motion is x_i, y_i and γ_i. We check the square located new position x_o+x_i, y_o+y_i with orientation $\gamma_o + \gamma_i$(dashed square). It overlaps with both the green and red particles so that we reject it. Then the particle try to move along the two edge components(pink arrow along $\gamma_o + \pi/4$ or orange arrow along $\gamma_o - \pi/4$) with equal probability. If we start with orange arrow, it does not overlap with any existing ones. Therefore we accept the motion along orange arrow with orientation $\gamma_o + \gamma_i$. If we start with pink arrow, this leads to overlap with green particle. Then the motion is rejected and has a final trial along orange arrow.

4.6.3.1 Define Square

We create a square class that describes a single square with unit side length by three parameters : position (x_0, y_0) and orientation θ_0 relative to the preferred mobility direction. When a particle moves or rotates, we simply update the corresponding parameters and do not need to change the vertices of each square. The square class has vertices vector and a method called *get_vertices*. We define two different types of square, one is diagonal-based and the other is edge-based. The vertices vector of diagonal based square vertices are $(1/\sqrt{2}, 0), (0, 1/\sqrt{2}), (-1/\sqrt{2}, 0)$ and $(0, -1/\sqrt{2})$. The

coordinate of edge based square vertices are $(0.5, 0.5), (-0.5, 0.5), (-0.5, -0.5)$ and $(0.5, -0.5)$. When we call *get_vertices* method, we rotate the vertices vector by the 2D rotational matrix: $\begin{pmatrix} \cos\theta_0 & -\sin\theta_0 \\ \sin\theta_0 & \cos\theta_0 \end{pmatrix}$ and add it to the center position (x_0, y_0). This method is only called for overlap detection.

4.6.3.2 Square Overlap

We used a general method to detect whether two squares overlap. FOr future studies, this method i very general and works for any two different types of polygon of variable size. In the present work, we limited ourselves to squares of one size. The idea and the detailed implementation of overlap detection is listed below:

1. Pick one of the two polygons, check whether each edge has any intersection with any edge of the other polygon. If any two edges has intersection, these two polygons overlap. Identification of intersection of two edges was simplified to a line-intersection problem in computational geometry. Specifically, we pick one line-segment (l_1 with end node a and b) and check whether the two nodes of the other line-segment (l_2 with end node c and d) are on different sides of l_1. Mathematically, if the cross product $\vec{ba} \times \vec{ac}$ has a different sign than $\vec{ba} \times \vec{ad}$, then node c and d are on two different sides of $l1$. We also need to check $\vec{dc} \times \vec{ca}$ and $\vec{dc} \times \vec{cb}$. If the end nodes of either line-segment are on different side of the other line, then the two lines intersect.

2. If no edge intersection is detected, we further check whether one polygon contains or is contained by the other. We pick every node of one polygon and check whether it is inside of other polygon. We do the same thing on the other polygon. If the node is inside of the other polygon, these two polygons overlap. This is a 2-dimensional computational geometry problem as well. Suppose we have a node with coordinate (x_0, y_0) and a polygon P, then we find the number

of intersection points (x_i^p, y_i^p) between P and line $y = y_0$ where $y_i^p < y_0$ or in other words, all the intersections on left side of the node. If the number of qualified intersections is odd, the node is inside of the polygon. More mathematical details are available at 'Point in polygon' in Wikipedia.

This is a general method for polygon overlap detection. In our specific case, all the squares are identical therefore we can skip the second enclosure test.

4.6.3.3 Overlap Query

Rather than testing whether a test particle overlaps all other particles, we use the Axis-Aligned Bounding Box Tree(AABB-Tree), a tree data structure that is efficient for overlap query[37].In our case, we used a 2-D AABB-Tree. As indicated by the name, axis-aligned bounding boxes are rectangles whose sides are parallel to the coordinate axes and enclose any complex shape within it. Specifically, the bounding box of a single square centered at (x, y) with unknown orientation is also a square centred at (x, y) but with side-length $\sqrt{2}$ and sides aligned with x-axis and y-axis. Every node of the tree is a bounding box that contains all particles or shapes in the daughter nodes. Therefore, the root of the AABB-Tree encompasses all the particles in the simulation box.

Given a bounding box of any shape, the AABB-Tree quickly returns the potential bounding box that may lead to overlap. Suppose the given box has intersection with a certain node, then we check whether it intersects with left or right sub-tree and further query with that sub-tree. Therefore, the best time-complexity of the query is $T(n) = 2T(n/2) + \mathcal{O}(1) \rightarrow T(n) = \mathcal{O}(\log n)$. It is possible that the given box intersects with both sub-trees. The worst case leads to $\mathcal{O}(n)$. Whether there is intersection between two axis-aligned rectangles can be easily checked by corner coordinates with time complexity $\mathcal{O}(1)$. Intersection between bounding boxes does not indicate the particles within them overlap. Once the potential intersecting bounding boxes are

identified, we apply the overlap algorithm described in the previous section to check whether particles have intersection. One example is illustrated in Fig 4.15.

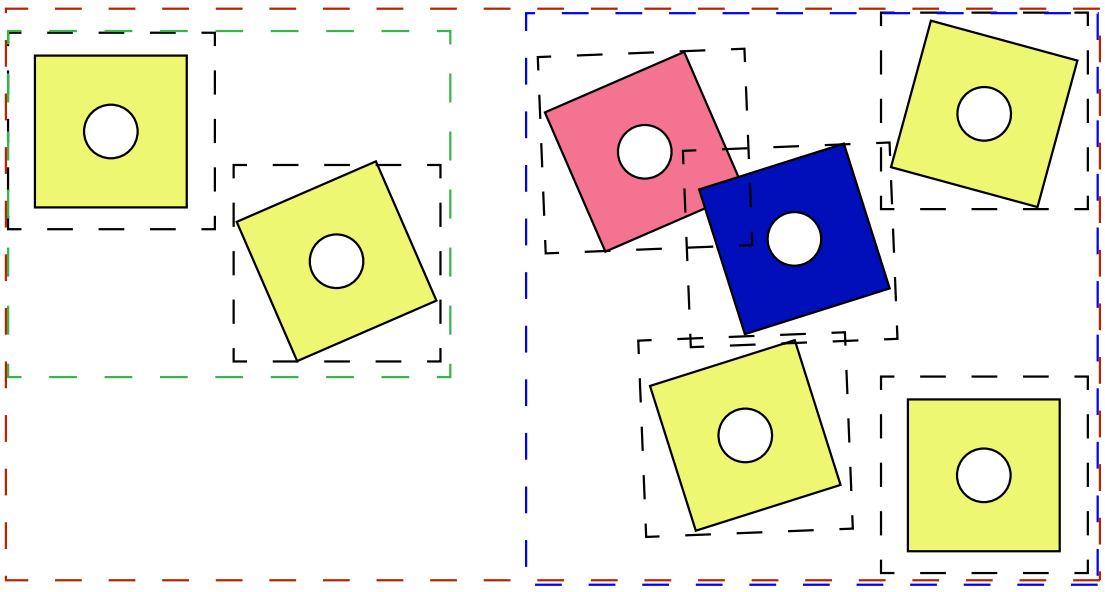

Figure 4.15: Example of AABB-Tree. All bounding boxes are plotted in dashed lines. We try to place the blue particle into the existing system. It's bounding box has overlap with the largest red bounding box so that we need to check both the left(green) and right(blue) subnodes. Since green bounding box has no overlap with the particle's bounding box, we only check the blue bounding box. We keep checking until the leaf of the tree. There are three bounding boxes having overlap with the blue particle. Then we apply the overlap algorithm on each particle, which would return the index of red particle that overlaps with the blue particle.

Another advantage of AABB-Tree is that it is efficient for particles with different size. However, it is not true in our case so that we don't have the most efficient algorithm. For fixed size system, cell list algorithm is a better option than the AABB-Tree method. We refer interested readers to Wikipedia.

To implement the 2D AABB-Tree we used code available at lohedge's Github. The detailed explanations of AABB-Tree are available at post[38] .

4.6.3.4 Periodic Boundary Condition

One difference between experiment and simulation is that we use periodic boundary condition in simulation. This leads to extra computation when we try to find the Voronoi cellss and Voronoi neighbors of particles. Particles near the boundary have neighbors crossing the boundary so that we need to create extra boxes.We create a 3×3 grids and put copies of the simulation box into each cell of this grid. Therefore, there are 18,000 particles in total and each particle has a unique index. The central cell contains particles indexed from 0 to 1999 and we identify Voronoi neighbors of boundary particle including the surrounding 8 cells. The indices of these neighbors are calculated as by finding the index-modulo-2000, the total number of particles in the original simulation box. This is a brute force method to handle the boundary condition and it is possible that more efficient methods exist.

4.6.4 Data storage

When we initialize the system, we give each particle an unique ID ranging from 0 to 1999. The IDs are kept unchanged in the simulation. To save a snapshot of the system, we save the position (x, y) and orientation γ of each particle ordered by their ID. If we save configurations at all time-steps, the data will be quite big($\sim$ GB). Therefore, we save the data separated by time gap t_g, which follows the rule:

$$t_g = \begin{cases} 10, & t < 1000 \\ 20, & t < 10,000 \\ 100, & t < 50,000 \\ 250, & t < 100,000 \\ 500, & t <= 200,000 \end{cases} \tag{4.7}$$

As a result, the saved data is around 60MB per run.

4.6.5 Results and Analysis

We run simulations in which the persistence length l_p of the particle, and the area fraction ϕ are varied. Simulations enable more ways to control the value of l_p. As $l_p = v_0 a/D_R$, we can tune it independently by v_0, D_R or both of them. We find that with fixed l_p if we scale both v_0 and D_R with a constant factor they have different phase behavior. We explore these results at the end of this section. However, in the first part of this section, to compare better with the phase diagram in the experiment, we choose to vary l_p by fixing v_0 and changing D_R. This is because D_R is dominant factor in controlling the activity in our experiment. We set $v_0 = 0.063$, $D_R = 0.283$ and explore six different values of l_p i.e. $10D_R \rightarrow 0.1l_p$, $2D_R \rightarrow 0.5l_p$, $D_R \rightarrow l_p$, $0.5D_R \rightarrow 2l_p$, $0.25D_R \rightarrow 4l_p$ and $0.1D_R \rightarrow 10l_p$.

In the simulation, we know the orientation of each particle with high precision. Therefore, we identify particles in the ordered phase by their degree of local orientational order ($\Phi_4 \geq 0.85$) instead of relying on the dynamics as the identifier of phase as in the experiment. The definition of interfacial particles is identical to that in experiment.

Snapshots of several configurations placed in a grid of l_p versus area fraction, ϕ, are shown in Fig 4.16. The simulation shows the same qualitative progression of phases as in the experiment. For fixed $l_p = 2.29$ (as in one of our experiments and y-axis $= 1$ in Fig 4.16), as the area fraction is increased phase coexistence develops beyond around $\phi = 0.28$. Likewise, for a fixed area fraction, phase coexistence appears when l_p is increased.

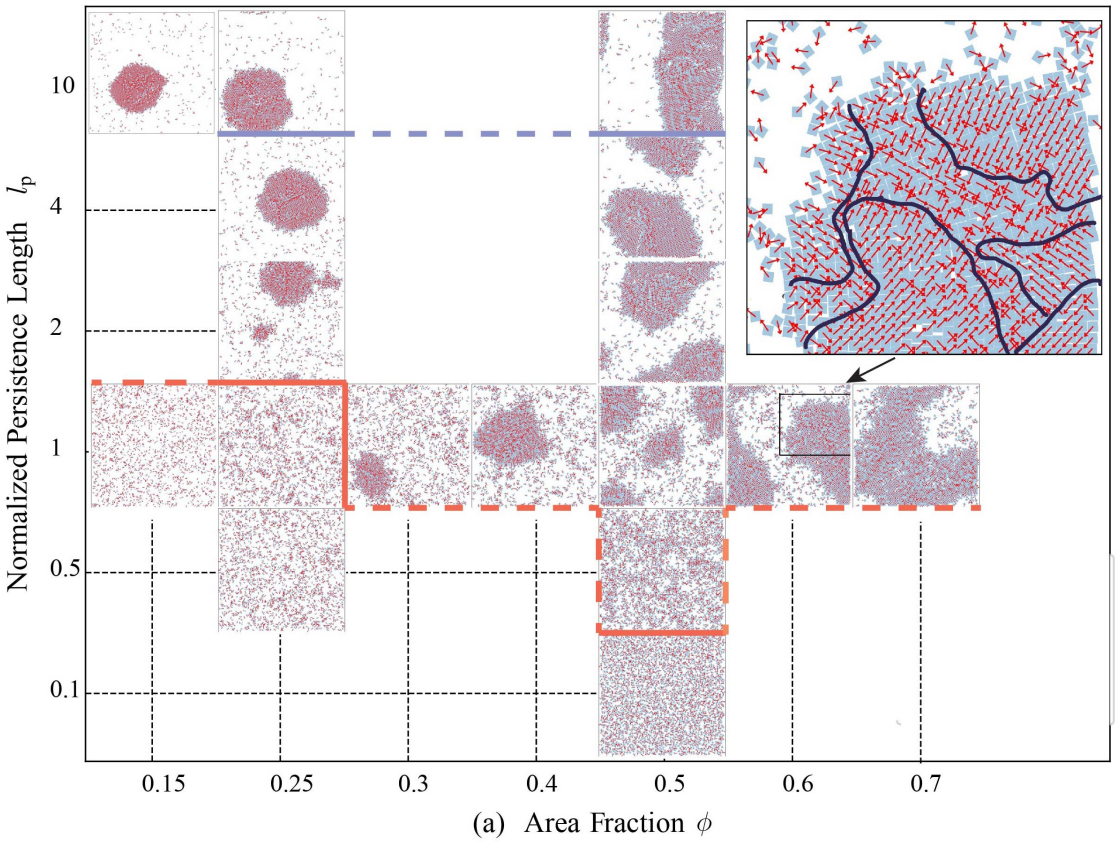

Figure 4.16: Steady state configurations from the simulation. The axis are not on a linear scale, but each snapshot is connected to the ϕ by a vertical dashed line. The vertical axis is the persistence length relative ratio to a baseline value of $l_p = 2.29$. The inset shows part of ordered state when $\phi = 0.6$. The ordered state is composed of large polarized domains whose boundaries are marked by the dark curve.

A further qualitative feature is illustrated in the inset of Fig 4.16 and Fig 4.17 where it can be seen that the ordered phase nucleates around linear chains of counter-posed particles of opposite mobility that kinetically trap each other. Once a few extended structures of these "antiferromagnetic" structures are created, they form a backbone on which large ferromagnetically polarized domains grow. The size of these fully polarized grains increases with activity. The resultant multidomain droplet of the ordered phase has nearly net zero polarization. To our knowledge, this phenomenon has not previously been noted.

Each phase is defined by the ratio of number of ordered particles to total number of particles $n_O = N_0/N$. We use lines to indicate the likely phase boundaries in Fig 4.16. Solid lines separate configurations in different states and indicate a possible phase boundary. Dashed lines indicate the existence of a phase boundary but that we are not sure of the location of the boundary. One challenge is how to effectively define a fully ordered state since we adopt criterion-dependent definition. Examples are shown in Fig 4.17(b),(c) and (d). We choose $n_0 > 0.95$ as an ordered state which makes (b) and (c) phase coexistence state and (d) fully ordered state. One distinction brought about by the absence of bounding walls, is that unlike in the experiment we did not observe a jammed system with immobile particles .

We explore phase density, phase number fraction, molecular orientational order Φ_4 and bond order Ψ_4 along two different cuts of the phase diagram: (i) We fix the activity at $l_p = 2.29$ and vary area fraction ϕ; and (ii) we fix the area fraction at $\phi = 0.5$ and vary the activity l_p. The results are plotted in Fig 4.18 and Fig 4.19, respectively.

For fixed $l_p = 2.29$ (as in one of our experiments), as the area fraction is increased, phase coexistence develops beyond around $\phi = 0.28$. While the partial fractions of the ordered and fluid phase both change with ϕ, the fluid and ordered phase density fluctuate about fixed values. The density of the ordered state is similar to that

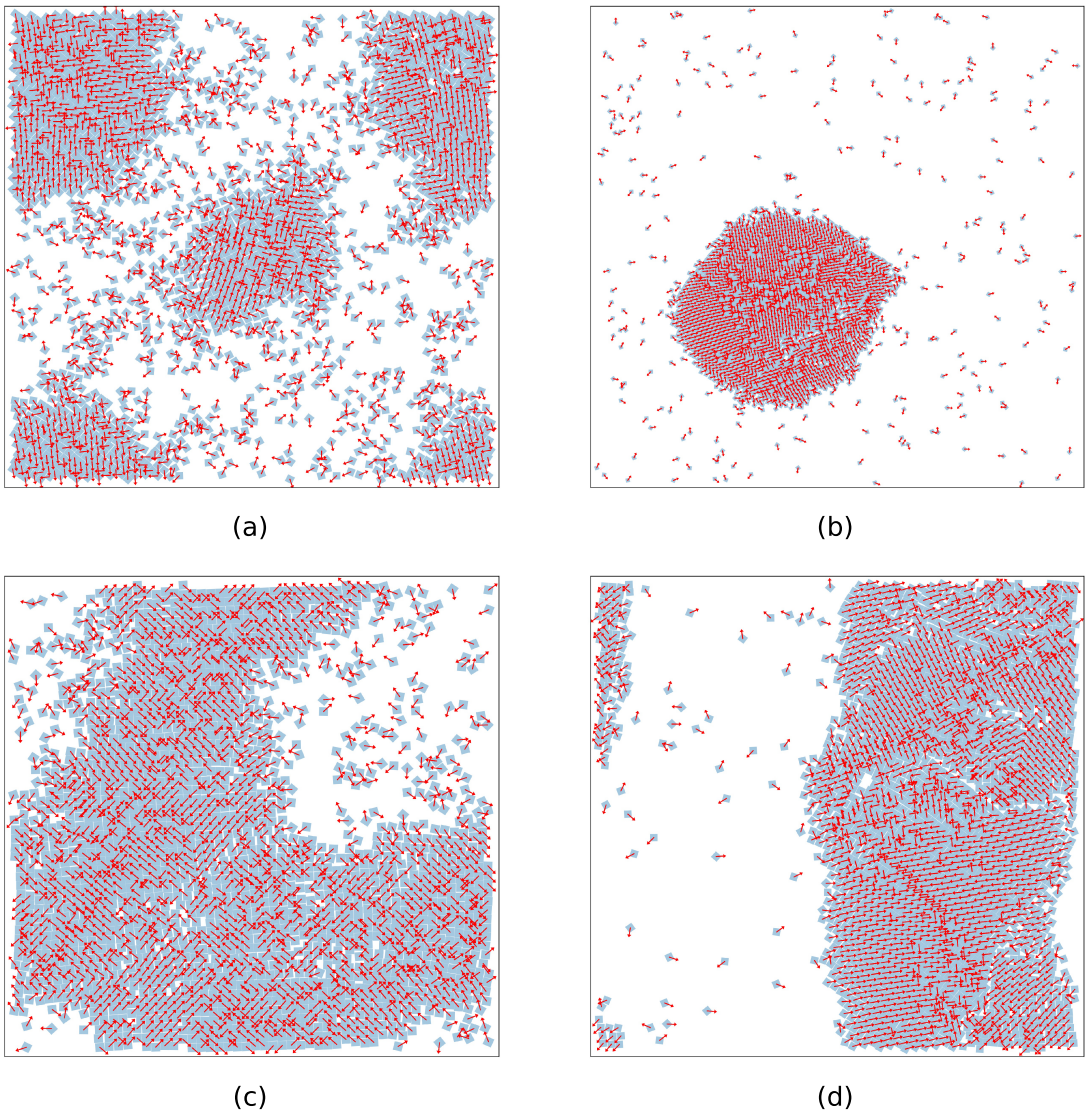

Figure 4.17: Zoomed-in snapshots of phase coexistence and fully ordered state. All four snapshots indicate that there are polarized regions inside the ordered state. The net polarization of a cluster is close to zero. As persistence length increased, area of polarized region also increases. The defects in the ordered state are also observed in experiment. (a) Phase coexistence state with l_p and $\phi = 0.5$. Fully polarized region is observed in the ordered state. (b) Phase coexistence state with $10l_p$ and $\phi = 0.15$. We define state of particles based on the number fraction of ordered state particles n_o. When $n_o > 0.95$, system is in fully ordered state. The number dependent criteria makes this case($n_o \approx 0.92$) phase coexistence. (c) Phase coexistence when l_p and $\phi = 0.7$. (d) Fully ordered state with $10l_p$ and $\phi = 0.5$. Not all 2000 particles are part of the cluster since a few particles(< 100) can move freely. However, there are big fully polarized chunks in the ordered state when compared to lower l_p (a) and (c). The boundary shape of ordered state in this fully ordered state is rough.

in experiment. However, the fluid density is lower than that in experiment which is consistent with the earlier starting point of phase coexistence in the simulation. Orientational order Φ_4 and bond order Ψ_4 have big fluctuations at the onset of phase coexistence ($\phi = 0.28$), then quickly jump to 1.0 and 0.8 respectively and finally fluctuate about those values. The value of bond order is higher than that in experiment. One possible reason that the circular boundary of experiment is incompatible with global four-fold order.

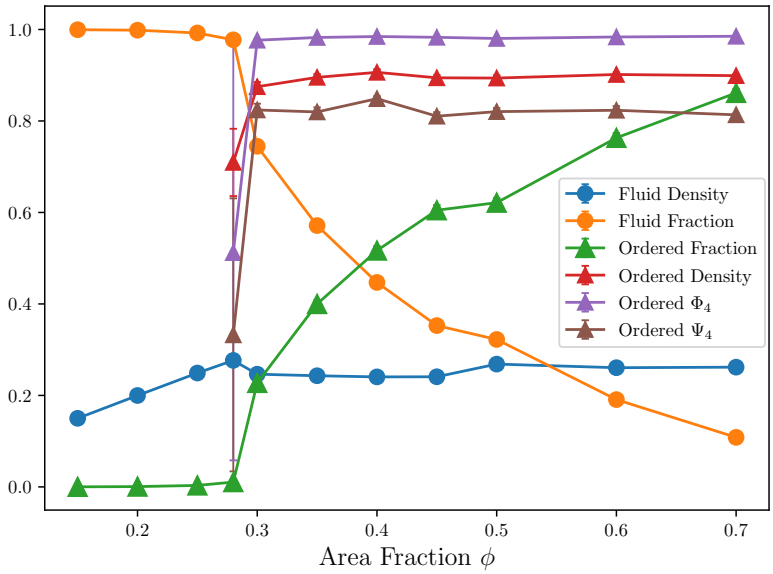

Figure 4.18: Phase number fraction, phase density and order parameters when $l_p = 2.29$. These curves qualitatively agree with our experiment.

For fixed $\phi = 0.25$, when scaled $l_p \leq 1$, the whole system is fluid. As the persistence length is increased, phase coexistence starts at scaled $l_p = 2$ and finally develops to a fully ordered state when scaled $l_p = 10$. The orientational order ϕ_4 and ordered density are small and noisy at $l_p \leq 1$, which indicate there is no stable ordered state. The ordered state is not found in all 200 configurations and the ordered state contains very few particles(≤ 10) in this case. ϕ_4 is close to 1 when phase coexistence starts, and saturates at that value. The tetratic bond order Ψ_4 increases at first (2 to 4) and then decreases(4 to 10). The trend of Ψ_4 is different from what we observed in

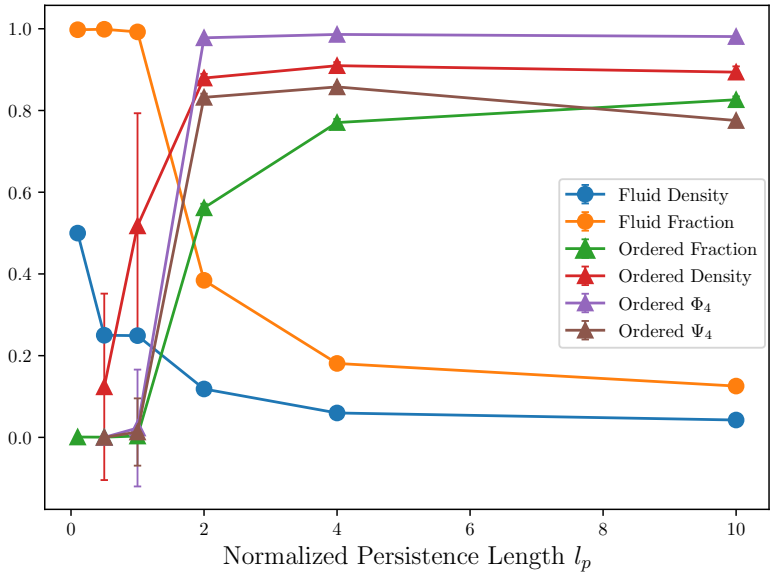

Figure 4.19: Phase number fraction, phase density and order parameter when $\phi = 0.5$. The scale base activity 1 is $l_p = 2.29$.

experiment Fig 4.10 where Ψ_4 gradually increases with l_p. The possible reason is that simulation realizes high activity that is not achievable in experiment. When activity gradually increases, particles get more closed packed so that Ψ_4 also increases. When activity is high enough(only achievable in simulation), particles get trapped by the nearby particles before they can reorganize themselves to fit into free space. Therefore more defects exist when compared to lower activity particles which leads to lower Ψ_4.

Our qualitative conclusion is that all significant experimentally observed phenomena can be seen in the absence of a hard boundary. However, the absence of a circular boundary makes some additional features much more evident in the simulation: the morphology of the condensed droplets vary substantially over the phase diagram. Drops formed at low ϕ are rounder and have smooth boundaries, whereas at higher ϕ, these regions are rougher and more ramified.

As mentioned earlier, fully polarized clusters are clearly observed in simulation(Fig 4.17), and are more easily identified than in the experiment, where close-packed clusters have

to curve along circular boundaries. We investigated the size of the four largest fully polarized region in the ordered state as we did in experiment. (Again, the choice of four regions is motivated by the four-fold symmetry of the particles). In experiment, we cannot capture the evolution from random initial configuration to stable state due to the competing constraints of capturing dynamics at a high frame rate and the limitations placed on long-time runs by the finite on-board memory in the high speed camera. However, this is not a problem in simulation where we can save all the needed data. We implemented the same depth-first search algorithm as in section 4.5. The only difference is that we need to construct neighbor dictionary with periodic boundary condition. Some snapshots of detected clusters are plotted in Fig 4.20. Comparing to experiment, polarized clusters are more easily seen in most ordered states. We argue that in addition to orientational order Φ_4, and bond order Ψ_4, there also exists polar order in ordered state. This is only observed in experiment under some limited conditions at the high density and high activity limit of our experiments. This is possibly due to the circular boundary of experiment.

We investigated the size of the largest four clusters to understand the growth and emergence of polar order in the system. We plot their evolution in Fig 4.21 when $\phi = 0.5, l_p = 2.23$ and $\phi = 0.5, l_p = 4.46$. Clusters grow gradually at early times, and then saturates at long times, following which the size of cluster fluctuates. The saturation time varies but it usually takes more than half the total simulation time (160000 steps).

In Fig 4.21(b), there are large fluctuations in a single curve. This comes from the time-independent detection algorithm that is sensitive to the fluctuation of orientation of a single or a few particle. We illustrate the idea in Fig 4.22. Both (a) and (b) are detected with same orientation threshold $\alpha_t = 0.08$ in different time step when $\phi = 0.5$ and $l_p = 8.92$. The top four clusters are quite different between the two snapshots. The largest blue cluster at $t = 106000$ separates into two different clusters(blue and

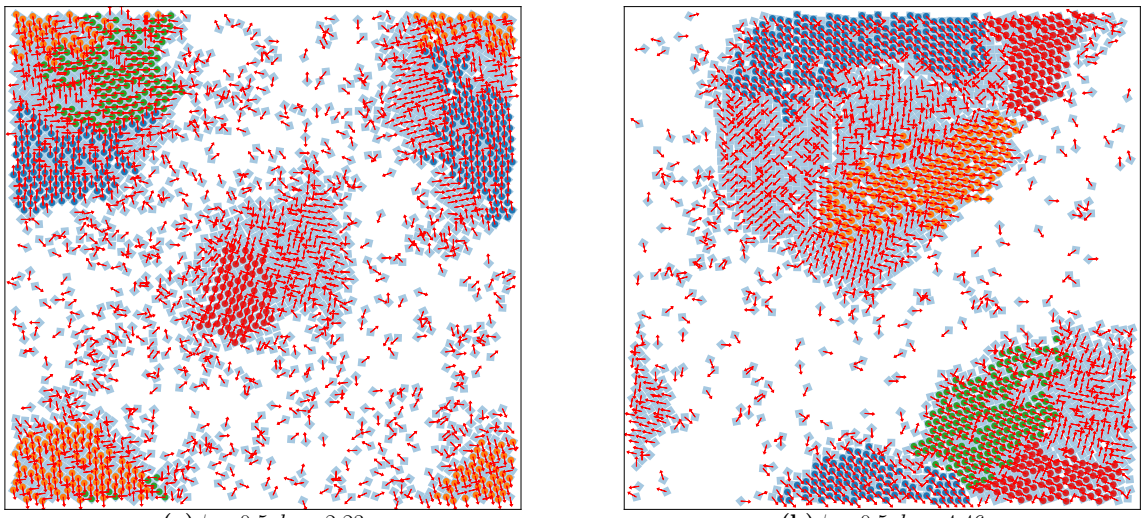

(a) $\phi = 0.5, l_p = 2.23$ **(b)** $\phi = 0.5, l_p = 4.46$

Figure 4.20: Illustration of clusters. Blue central dots represent largest cluster, followed by orange central dots and green dots, red central dots are the smallest cluster. (a) Top four clusters when $\phi = 0.5$ and $l_p = 2.23$. Particles with same color belong to the same cluster. (b) Top four clusters when $\phi = 0.5$ and $l_p = 4.46$. Fully polarized clusters are observed in lower area fraction and lower persistence length as in the experiment.

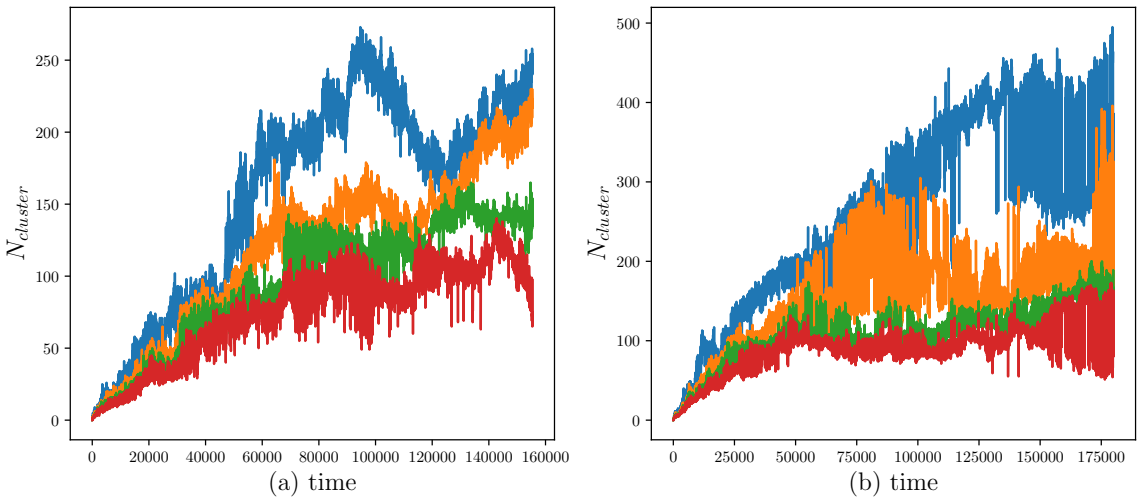

Figure 4.21: Size of top four cluster as function of simulation time steps. (a) $\phi = 0.5$ and $l_p = 2.23$ (b) $\phi = 0.5$ and $l_p = 4.46$. There are big fluctuations in blue and orange curves after $t = 50000$. This comes from the detection inconsistency in the detection algorithm as shown in Fig 4.22.

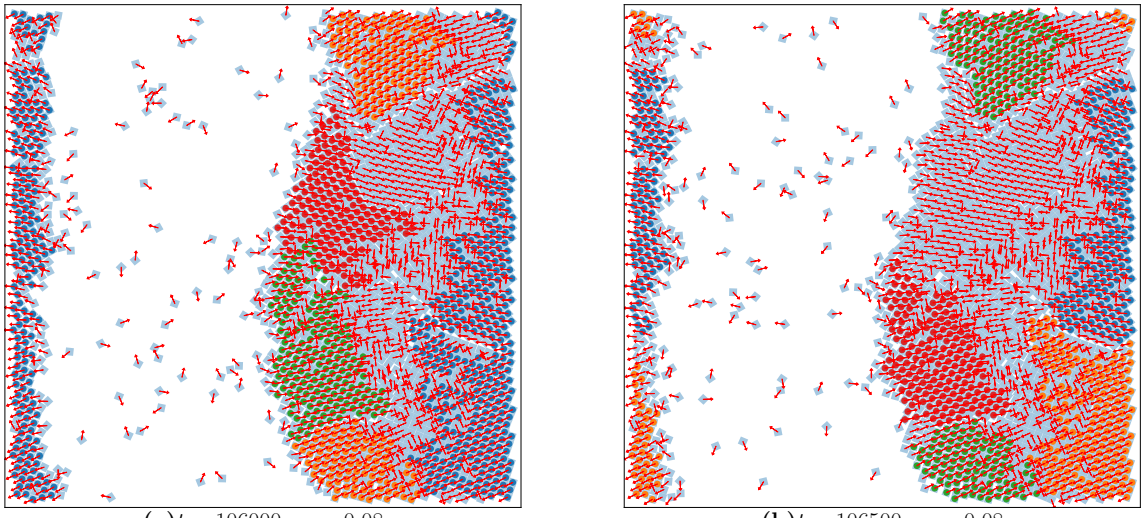

(a) $t = 106000, \alpha_t = 0.08$ **(b)** $t = 106500, \alpha_t = 0.08$

Figure 4.22: Snapshots of the four largest clusters at two different time steps when $\phi = 0.5$ and $l_p = 8.92$. Particles within the same cluster have same color. (a) The largest cluster has 550 particles and is colored in blue. (b) The largest cluster separate into two clusters in blue(300) and orange(250). Fluctuations of orientation of interfacial particle cause the separation.

orange) at $t = 106500$. The reason is there only exists two interfacial particles between the blue and orange clusters at $t = 106500$. Both of them have a larger orientation difference between their neighbors than threshold α_t. However they are within the threshold at $t = 106000$. Therefore, tiny orientation fluctuation leads could lead to quite different cluster assignment result. The origin of big cluster size fluctuations in a short time period is due to splitting and merging of a big cluster at a small neck.

Since our detection algorithm is time-independent, this kind of detection noise is inevitable. One possibility for future improvement is to dynamically track the cluster size and check for consistency in consecutive time steps.

We further compare evolution of quantities, at fixed area fraction $\phi = 0.5$ and different activity, like ordered fraction n_O, tetratic bond order Ψ_4, the largest cluster size $N_{largest}$ and average of top four cluster size $\langle N_{cluster} \rangle$ in Fig 4.23. We didn't use orientational order Φ_4 since ordered particles are defined based on it(≥ 0.85). Once

there exist Φ_4 larger than the threshold, the curve jumps to a high value and keep unchanged which leads to identical curves in all five different persistence lengths.

Fig 4.23 shows the evolution of various indicators of ordering developing as a function of time for many values of activity, at a fixed area fraction of ϕ =??. The data indicate that the system develops into an ordered state (high orientational order and bond order) within $\sim$ 30000 steps. Surprisingly, the time scale over which order develops does not show a marked dependence on activity. The lower two panels, which show different markers of polarization, show that they take much longer to form polar order ($\sim$ 100000 steps). Ordered fraction n_O increase quickly and converges to a constant value. The curves of n_O don't show a strong systematic dependence with l_p ($4l_p$ and $5l_p$ are counter-example). We argue that stable system with high activity has a larger proportion of ordered particles. Tetratic bond order Ψ_4 has same trend as n_O. It jumps to 0.6 once particle form ordered state. Before it converges, particle with higher activity has larger Ψ_4. After converges, the magnitude is independent of the activity. Size of largest polarized cluster is independent of particle's activity. We have ran simulation of particles with $4l_p$ in two different ensembles(one is labeled as $4l_p$ new in Fig 4.23). The size of largest polarized cluster is quiet different. Other quantities are similar in these two different simulations. Finally, we study the mean value of largest four clusters $\langle N_{cluster} \rangle$. This value is also independent of particle's activity. We argue that the size of cluster is not predictable given area fraction ϕ and persistence length of single particle l_p.

4.7 Conclusion

In this chapter we have for the first time experimentally explored the phase diagram of self-propelled particles in the density-activity (ϕ vs l_p plane. We also have simulations in the same regime that qualitatively agree with the experiment. The example we have explored is that of hard squares with polar activity along the diagonal.

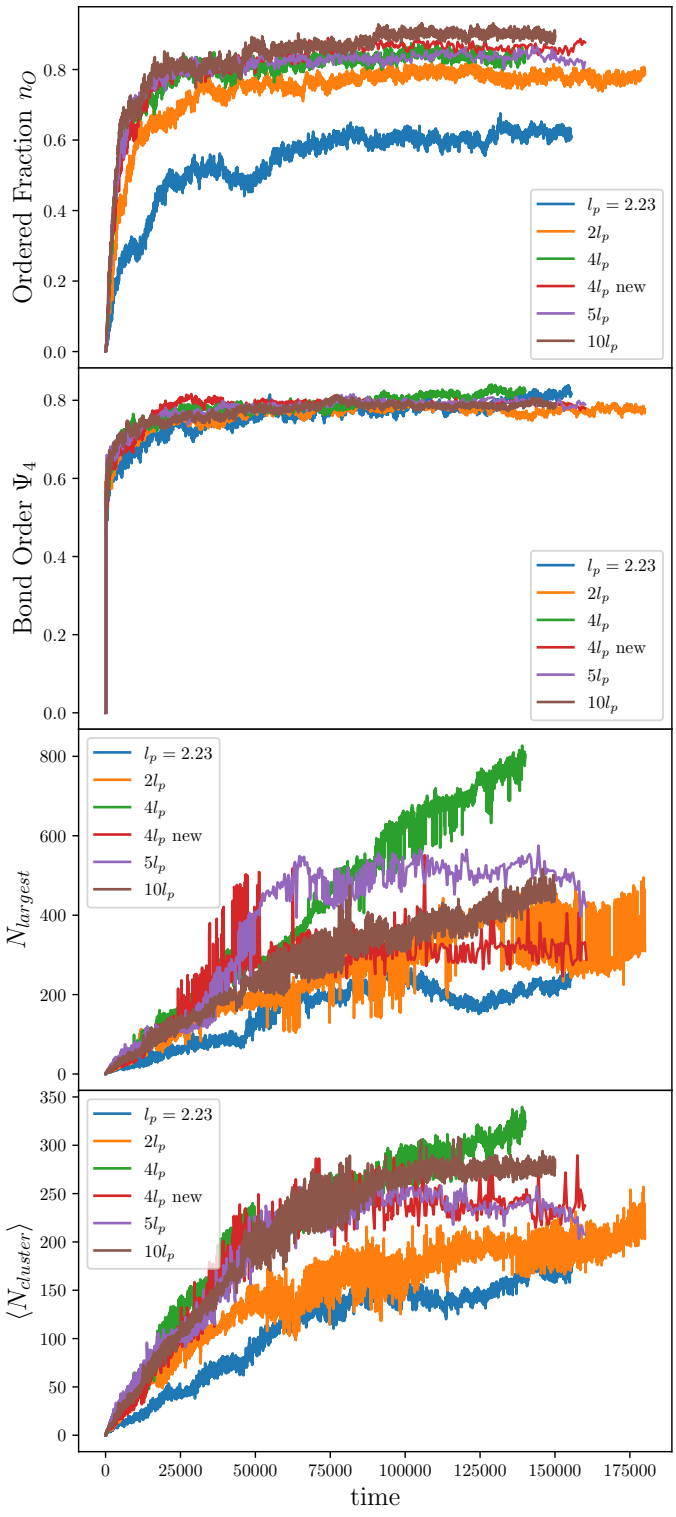

Figure 4.23: Time-evolution of order parameters for various values of persistence length. The systems quickly form an ordered state based on ordered fraction and tetratic bond order order. However the development of large polarized regions grows much slower.

In order to study the phase diagram, we have successfully tuned rotational diffusion of particles, so that they are not trapped on arrival at a boundary. Our results show that nonequilibrium activity profoundly alters the equilibrium phase diagram, in this case leading to the opening of a phase coexistence region between ordered phase and isotropic fluid. More generically, our work is an example of how the interplay between the symmetry of the interaction and the symmetry of the particle mobility can alter the onset of ordered phases. Granular systems are especially amenable to separating these two local symmetries, as the projected 2D particle shape dictates interactions while features in the other dimension can be tuned to change mobility.

CHAPTER 5

SYMMETRY OF ACTIVITY

In previous chapter, we show that adding activity to isotropic squares brings new phase behavior by both experiment and simulation. We study the phase diagram by changing the magnitude of activity or persistence length l_p. In this chapter, we further explore the effects of activity beyond merely tuning the magnitude of the mobility via the Peclet number. Here, we study by simulation how the *symmetry* of activity changes the phase behavior.

Activities can have various symmetries: in previous parts of this thesis we worked with polar symmetry, however, as discussed in this chapter, other types of mobility are possible. Furthermore, these symmetries need not be the same as the symmetry of the interaction potential between particles. In this work, we maintain the four-fold hard square interactions between particles. However, we study three different symmetries of activity, which are sketched in Fig 5.1. Each row corresponds to one symmetry of activity: polar, bipolar and chiral. Furthermore, the symmetry axes of the mobility need not to align with the axes of the interaction potential. This is distinct from the biological case where mobility axes align with interaction. This also differs from wet system where interactions are hydrodynamics.If particle moves in certain direction, it doesn't matter what the shape is, it induce flows that interact with other objects in the the direction of motion. This makes granular systems different.

Indeed, for a given symmetry of activity and a given symmetry of interaction, there can be any angle between the symmetry axes. With each class of symmetry, we choose two different activity directions relative to the square shape of particle.

Therefore we have six different kinds of particle: polar along diagonal, polar along edge, bipolar along diagonal, bipolar along edge, left chiral and right chiral.

In this work, we explore phase behavior by simulation. Experimental realizations of some of these types of particle mobility have previously been successfully achieved by my colleague Lee Walsh. The idea was to once again modify surface features of squares to impart the desired mobility.The experimental challenge here is to quantitatively control the activity efficiently and to explore what activity can bring interesting phase behavior. These difficulties can be more easily addressed in simulation, and suitable choices may then guide future experiments. For each kind of activity, we change the magnitude of activity l_p at certain fixed area fraction ϕ and vary the area fraction ϕ at fixed activity l_p.

5.1 Activity Model

In this section, we introduce the detailed realization of each kind of activity in simulation.

5.1.1 Polar Symmetry

Polar symmetry of activity indicate particle tends to move along one certain body axis. Based on the square shape, the polar activity has four-fold tetratic symmetry. We pick two activity axes, one perpendicular to the edge, and the other along diagonal. These are inclined at 0 and $\pi/4$ angle, respectively, to the body axis of square.

The polar diagonal particle is identical to what we have in Chapter 4. We simply adjust the parameters to compare it with other activity symmetry. As we introduced in section 4.6.3.1, vertices of edge particle are located at $(0.5, 0.5)$, $(0.5, -0.5)$, $(-0.5, 0.5)$ and $(-0.5, -0.5)$. The algorithm of overlap checking is same as that of polar diagonal ones. However, this is some difference in dynamic model. When we propose a possible move of an polar edge particle, if it causes overlaps with any

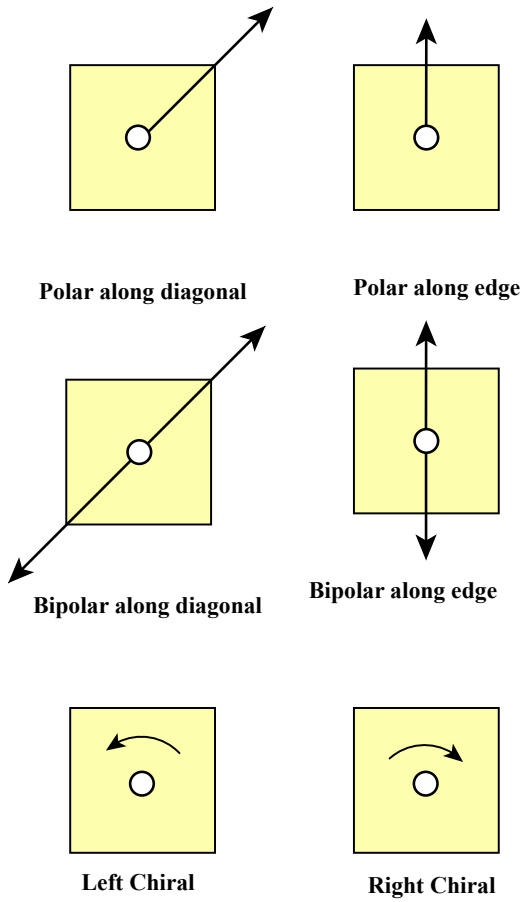

Figure 5.1: Illustrations of particles with different types of activity. Each row corresponds to one kind of symmetry and contains two types of particles with different directions.

other particles, we reject the move, and do not attempt moves decomposed into two independent components along edges.

5.1.2 Bipolar Symmetry

Bipolar, or nematic, symmetry of activity indicates that the particle tends to move along a body axis without a preferred sign of motion. To make a comparison to polar particle, here too, we choose motion perpendicular to the edge and along the diagonal direction. The bipolar particles have 0.5 probability moving along either longitudinal direction $\vec{v_l}$ or inverse longitudinal direction $-\vec{v_l}$ direction. We keep

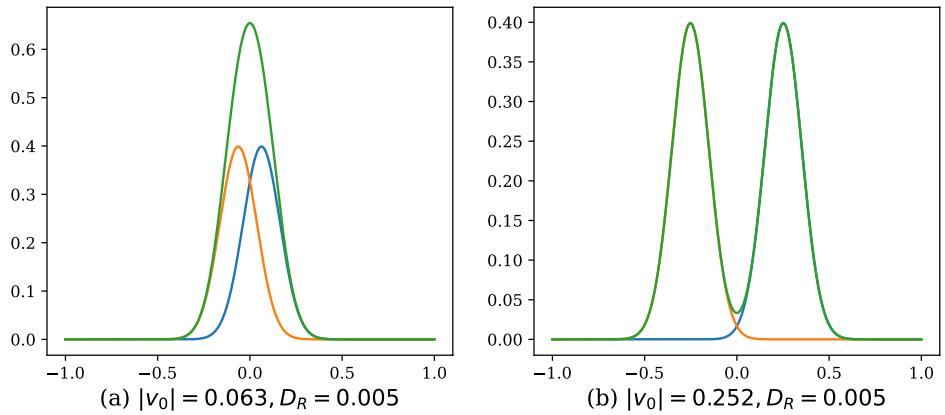

Figure 5.2: Illustration of longitudinal velocity distribution of bipolar particles. Please note that the curves are not normalized. (a) Using the same parameters that we found in experiment for a polar particle leads to a Gaussian distribution without distinct peaks, so the particle effectively becomes isotropic. (b) We increase the mobility to $v_0 = 0.252$ as $2|v_0| > \sqrt{2D_0}$, which makes a double peak Gaussian distribution that more accurately represents a bipolar particle.

the rotational velocity v_ω subject to symmetric noise as we did previously. The probability distribution of longitudinal velocity equals to $p(v_l) = 0.5 \times \mathcal{N}(v_0, 2D_0) + 0.5 \times \mathcal{N}(-v_0, 2D_0)$. Here $\mathcal{N}$ is Gaussian distribution with mean value v_0 and variance $2D_0$. To achieve noticeable effects of bipolar activity, $p(v_l)$ needs to be a double-peaked Gaussian distribution. The magnitude of $|v_0|$ and D_0 controls the shape of distribution. If we keep the same parameters as we had for polar particles in the experiment($v_0 = 0.063, D_0 = 0.005$), $p(v_l)$ the two gaussian peaks overlap strongly, Fig 5.2(a) so that particle dynamics are indistinguishable from an isotropic particle. In order to separate these peaks, we keep D_0 unchanged and make $v_0 = 0.252$ to make particle bipolar as shown in Fig 5.2(b). Here, bipolar diagonal particles still have three potential moving directions and bipolar edge particles have one potential moving direction.

5.1.3 Chiral

In the ABP model for polar particles, rotational velocity v_ω follows a Gaussian distribution $\mathcal{N}(0, 2D_R)$ with zero mean. For chiral particles, we simply shift the mean value of v_ω to a non-zero value. We tested $|v_\omega|$ from $\pi/3/step$ and decrease to 0 gradually with smaller gaps. We study chiral particles on both passive particle with $v_0 = 0$ as well as particles with translational activity $v_0 = 0.01575, 0.0315, 0.063, 0.126$ and 0.252. We won't report all results here but only show

5.2 Results and Analysis

We ran the simulation in a square simulation box. The simulation box contains 2000 identical particles with the same symmetry and direction of activity . Instead of getting a full phase diagram, we hold activity fixed and vary area fraction, or hold area fraction fixed and vary activity, to study the phase behavior. This gives us two orthogonal cuts along the phase diagram. The statistical results presented here are taken from 200 configurations collected after the system has reached steady state. We compare the results with different types of activity in the following section.

5.2.1 Changing density at fixed activity

We first study the phase behavior when we move along the area fraction axis. The results are shown in Fig 5.3. In each row, we illustrate type of activity, show a snapshot of the steady state of simulation box and plot statistical quantities. We calculated fluid density, fluid number fraction, ordered state density, ordered number fraction, ordered tetratic orientational Φ_4 and ordered tetratic bond order Ψ_4 for each type of particle as we did in last chapter on polar squares. All x-axes in the 3rd column in Fig 5.3 are area fractions ϕ.

We start by comparing polar diagonal and polar edge particles. The transition from a fluid state to phase coexistence are both observed in these two type of particles.

The snapshots(Fig 5.3) are taken when $l_p = 2.23$ and $\phi = 0.5$. These snapshots indicate that the ordered state in diagonal particles is more close packed than that in edge particles, possibly due to the difference of dynamic model. Specifically, the polar diagonal particle has more options when an attempt motion leads to overlap with other ones. In the polar edge particle system, there are more defects and voids within the ordered state. As a result, edge ordered state has lower density(~ 0.8) than diagonal ordered state(~ 0.9). Comparing the curves, the trends are similar between diagonal particles and edge particles, but the details are different. Edge particles start phase coexistence at a lower area fraction($\phi \sim 0.2$) than diagonal particles($\phi \sim 0.28$). The fraction of ordered and fluid edge particles changes smoothly with volume fraction. Once phase coexistence starts, they increase/decrease linearly. On the contrary, for diagonal polar particles there is a kink when phase coexistence starts and then the curves change in a nonlinear pattern. The observation of a greater number of voids and defects from the snapshot of lower density ordered state in edge particle is borne out by the data for the density of the ordered state. When the ordered state forms, fluid and ordered phase density remain constant for the polar diagonal system. However, for the edge particle they both increase slowly with area fraction. To summarize, both diagonal and edge particles have qualitatively similar phase behavior but there are quantitative differences in details. The interesting fully polarized region in diagonal particle is not clearly observed in edge particle. It is because a pair of particles is enough to block each other. For the diagonals, it needs four vectors to add up to zero to block displacements.

By contrast, as we show below, bipolar (nematic) activity has only a modest effect on activity, regardless of how it is oriented relative to the axes of the square.

The double peak Gaussian velocity distribution of bipolar particle is decided by two parameters, mean value v_0(= 0.063 in experiment) and variance $2D_0$(= 0.005 in

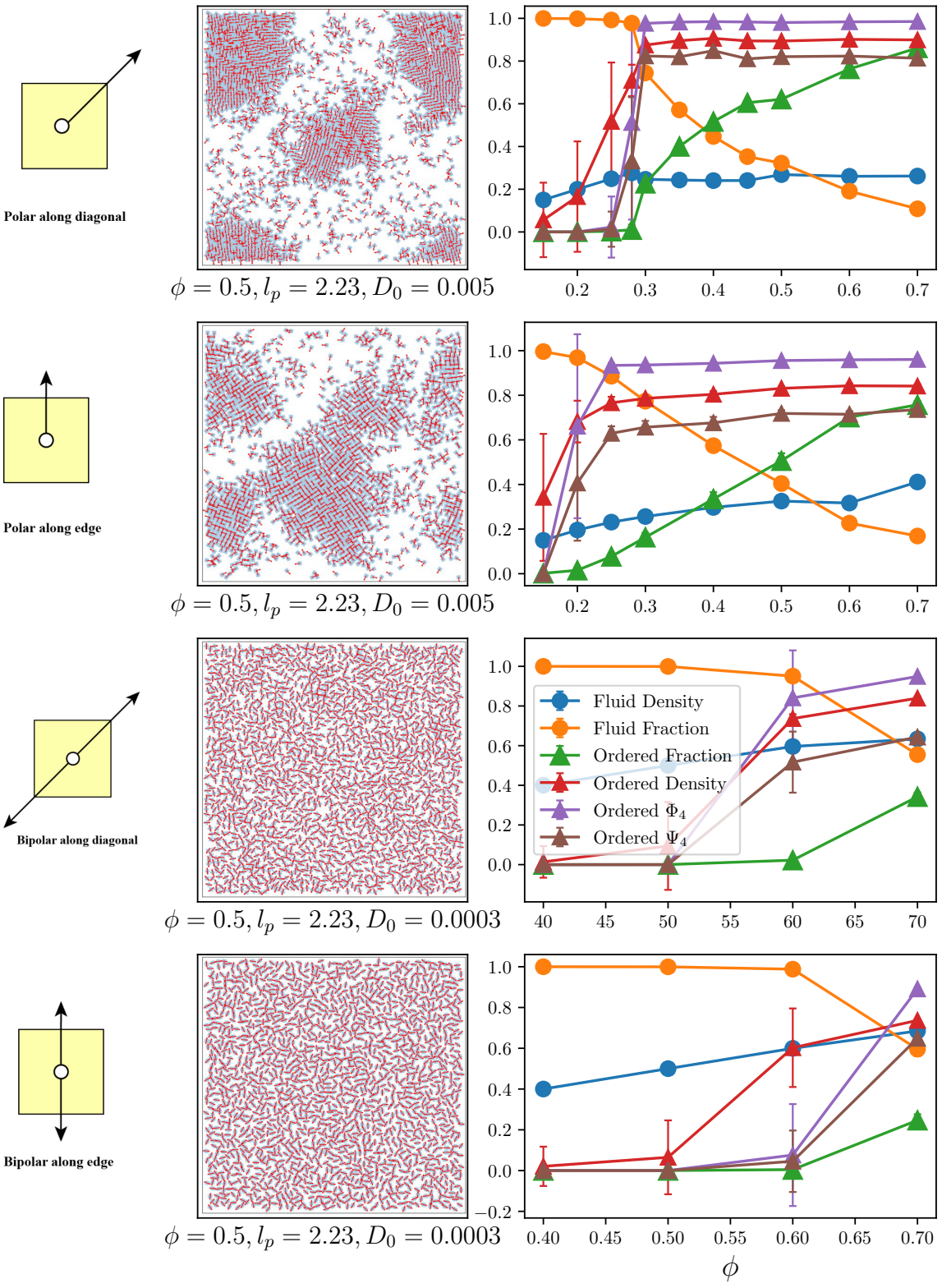

Figure 5.3: Snapshots (left column) and order parameters of polar and bipolar activities with fixed $l_p = 2.23$ as a function of area fraction, ϕ

experiment). To ensure $2|v_0| > 2\sqrt{2D_0}$, we could either increase v_0 or decrease D_0. We test both options and make the ratio $|v_0|/\sqrt{D_0}$ constant.

In the scenario of decreasing D_0 , we keep l_p constant and decrease D_0 by a factor of 16, $D_0 = 0.005/16 \approx= 0.0003$. We plot the results in Fig 5.3 as we can compare different type of activity with same magnitude l_p. The snapshots and curves show that bipolar symmetry significantly reduce the effect of activity. Bipolar diagonal particles do not show a sign of phase coexistence until a very area fraction of $\phi = 0.6$. At $\phi = 0.6$, edge bipolar particles remain in a fluid state with hardly any evidence of an ordered state. The fluid state density keeps increasing linearly with area fraction. Although there is the onset of an ordered state at $\phi = 0.7$, the continued increase in the fluid state density indicates that the whole system still remains in a fluid state.

Since we initialize particles on a square lattice when $\phi > 0.5$, our initial condition introduces some degree of bond order. We need to test at high ϕ that if the ordered state comes from the activity or just caused by the high area fraction. We plot the results of isotropic particles in Figure 5.4. It shows that isotropic particles keep fluid state until $\phi = 0.6$ and having orientational order at $\phi = 0.7$.These data demonstrate that bipolar edge particles are similar in phase behavior to the isotropic particles.

In increasing mean value scenario, We choose $v_0 = 0.252$ which makes $l_p = 8.92$ and keep $D_0 = 0.005$ unchanged. We plot the results in Fig 5.4. Bipolar symmetry significantly reduces the effect of activity on the phase behavior.

5.2.2 Changing Activity at fixed density

In this section, we discuss the data obtained from fixing the area fraction and varying persistence length. For polar activity, we increase l_p by decreasing D_R. For bipolar activity, we increase l_p by increasing v_0 since decreasing D_R make us change two parameters D_T and D_R. Increasing v_0 also causes another issue. When $\phi \leq$

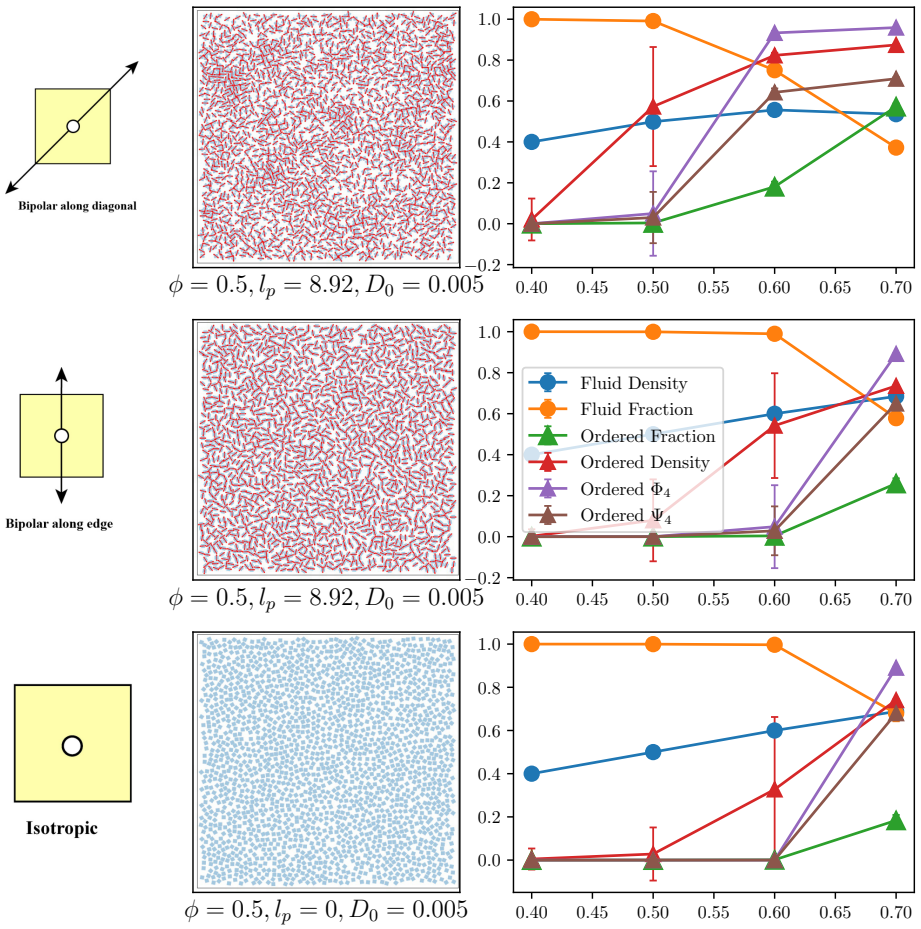

Figure 5.4: Phases of bipolar and isotropic particles as a function of area fraction for fixed activity $l_p = 8.92$. Here we decreased the diffusion constant D_0 to realize the double peak Gaussian velocity distribution. We also show isotropic particles as a baseline. Since the isotropic particle have no preferential mobility direction we don't add the red arrow on it.

0.7 and $v_0\delta t$ in a single simulation step is larger than the average spacing between particles, the system got frozen whatever the state is.

The two sets of data with differently oriented polar symmetry have similar trends, but with differences in detail. We keep the area fraction $\phi = 0.25$ fixed for both diagonal- and edge-polarity and study how phases change with persistence length l_p. We show the results in Fig 5.5. When activity is low, all particles are in fluid state. The system enters phase coexistence as l_p increases. We have not yet observed a fully ordered state at the maximum activity that we explored, $l_p = 22.3$. Polar edge particles starts phase coexistence at a lower l_p compared to polar diagonal ones. The ordered state in polar diagonal particles are more close-packed so that their ordered state density is higher, as is the tetratic bond order Ψ_4. Polarized clusters are observed in both diagonal and edge particles at highest l_p. The characteristics sizes of polarized cluster of diagonal particles is larger than that of edge ones.

We study bipolar symmetry particles at fixed area fraction $\phi = 0.5$. We choose a higher ϕ for bipolar particles than we did for the polar particles, as our previous observations showed that they do not condense as strongly, and will stay in the fluid state at low area fraction. A higher ϕ is more likely to show interesting phenomena. However, we found that the results at large enough v_0 are affected by an issue due to the interaction model we implemented. Bipolar edge particles got jammed at all interesting values of activity at this density. The spacing between particles is smaller than the velocity so that the majority of particle update attempts are blocked. Therefore, the orientational order ϕ_4 is low and particles remain in a fluid state. Bipolar diagonal particles show the sign of phase coexistence $l_p = 17.8$.

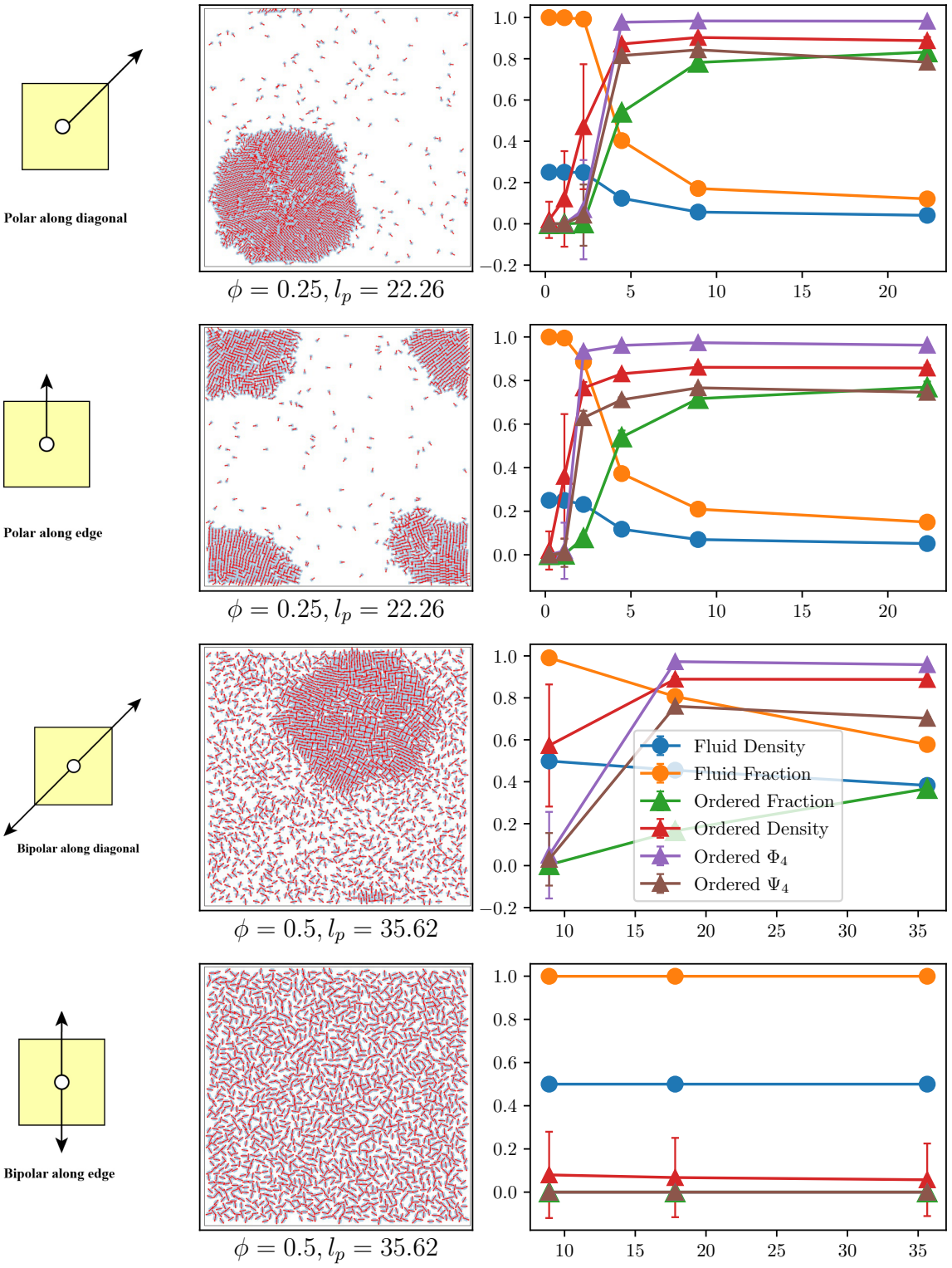

Figure 5.5: Two groups of snapshots and order parameters for particles with different symmetry of activity at fixed l_p and ϕ. All snapshots (second column) are the last data point with highest l_p at the third column. The result of last row does not make sense since the system got forzen at initial configuration.

5.2.3 Chiral Particles

In this section, we study how chiral activity affect the phase state. We have tested both left and right chiral activity. The results show that left and right chiralities are symmetric so that the phase behavior are similar. We study chirality on both active and passive particles.

We add chirality on polar diagonal particles when $\phi = 0.5$, $l_p = 2.23$, $v_0 = 0.063$ and $D_0 = 0.005$. We vary the mean rotational velocity ω_0 and plot the results in Fig 5.6. When $\omega_0 = 0$ particles are in the phase coexistence state described earlier. When we increase the rotational mobility, this ordered state melts and turns into fluid state whose density is 0.5. Therefore, chiral activity cancels out the effect brought by translation activity.

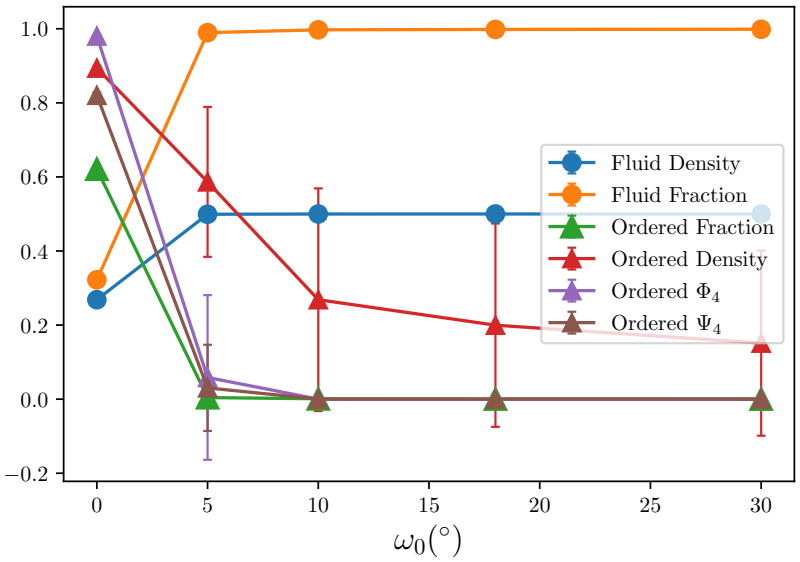

Figure 5.6: Order parameters against the mean value of rotational velocity ω_0 when $l_p = 2.23$ and $\phi = 0.5$. With increasing ω_0, system melts from phase coexistence state to isotropic fluid.

We also add chiral mobility on passive particles. The curves are almost identical to the isotropic one in Fig 5.4. Therefore it shows that chiral rotation has no effect on passive particles so that they have identical phase behavior.

The results are opposite to what we expected. We were expecting particles get locked since particles rotating along opposite direction would block each other so that they form a pair. This may come from the limitation of simulation model. In experiment, all particles can spin at the same time. However in one simulation step, we only sequentially propose motion of a single particle. This particle does not realize how its neighboring particles rotate. And thus, the simulation does not produce gear-like motions of particles spinning simultaneously. In other parallel-update simulations[39], this problem also exists. They split the simulation box into subgrids and propose motion of single particle within each subgrid to realize parallel computing. Therefore, it is impossible to achieve simultaneous motion of all particles in simulation. In the absence of a good simulation model, it may be best to test the chiral particles in experiment and then develop better interaction models.

5.3 Conclusion

We realize three different symmetries of activity: polar, bipolar and chiral in simulation and study how the symmetry and orientation of the mobility affect the phase behavior. The results show that various symmetry activities have quite different phase behaviors. Polar particles evolves from isotropic fluid state to phase coexistence between fluid and ordered state and finally to fully ordered state with increasing persistence length l_p. Bipolar activity also shows phase coexistence but this sets in only at nearly the large activity we used in the simulation. Our simulations do not reveal what happens after phase coexistence, as we are not able to reach extremely high l_p with our simulation model. Particles with chiral activity show phase behavior that is similar to isotropic particles. By itself, chiral symmetry does not bring any new phase behavior.

Furthermore, for each choice of symmetry of activity , we test also two orientations of the mobility axis. Our data shows that for a given symmetry, particles with different

mobiity orientation have similar trends in their phase behavior, and the differences are largely quantitative and not qualitative.

CHAPTER 6

FUTURE DIRECTIONS

The system of vibrated self-propelled polar hard squares are just a start pointing in the study of active phase diagrams. There are many possible areas to further explore of which I discuss some in this section.

6.1 Mixture of Passive and Active Particles

With currently available particles, we can explore systems of active and passive mixtures. Passive particles would have identical design used in our group's previous work[18] - these particles have a cylindrical knob on the top like Lego squares, so that their motion is isotropic even though they are square in their 2D projection. In this system, we can control the number ratio of active to passive particles and thus further extend a third axis on the phase diagram. This allows a different way to tuning a system from completely passive to completely active. At one limit, you can see how a dilute set of active particles moves in a passive background, and at the other limit, you can study how a small set of passive particles might disrupt activity-driven ordering.

The potential challenges are controlling the dynamic parameters of two different types of particles in the same cell. Ideally, we would wish to design particles with all the same diffusion parameters, but make only the mobility non-zero. There are practical hurdles to this, as adding features that confer mobility, also change the diffusion constants. Then, the first question is what is a good ratio of $D_R(active)/D_R(passive)$. If we change this ratio, will we have same result? Secondly, if we pick a particular

value of the D_R ratio to work with, how can we work particles with different persistence length? The rotational diffusion D_R of our particle is highly dependent on the ratio of particle height to gap between the upper plate and substrate of cell. If we increase the gap and try to keep the same D_R ratio, this might also affect the diffusion constants of passive particles. This idea could also be easily investigated in simulation as we just need to change the dynamical parameters in our code.

There is another possible practical challenge to solve in detection. If we use larger passive square particles (e.g. with sidelength 7.62mm, as in this thesis), it means we are able to use convolution detection techniques, rather than the CNN. As shown in Fig 4.2 [NM which figure are you citing here??], active and passive particles have the same design. Sizes of central dots have some difference so that it is difficult to use one parameter(width of Gaussian kernel) to find all the central points. One possibility is manufacturing new particles with same-sized central dots. Detection of corner dots do not have this issue since the corner sizes are similar in these two type of particles. Even if we find out all the position, we need to design a mechanism to differentiate the particles. One possible solution is printing one of the particles in white material and marked in black paint so that we can have two separate data. If we use particles with smaller particles, we could solve the detection issue with machine learning algorithm. One main drawback of the current algorithm is that it only works for square with fixed design. If we have a new particle shape, for example triangle, or have new marker design, we will need to reconstruct the training data set from scratch.

6.2 Phase Diagram of Other Possible Particles

We can change the property of single passive or active particles and explore phase diagram of that particle. There are several options in the types of new particles that are motivated by the results of our simulations.

1. Realization of all particles experimentally in what we described Chapter 5 and study the phase diagram. It will be a big project to design active particles that have nontrivial phase behavior. We could compare the results of experiments and simulations.

2. Change the footprint of particle. Possible options include triangle, pentagon and hexagon. The square, triangle and hexagon have ordered phases; the pentagon (or other shapes that do not tile the plane) might be particularly interesting. We could start from passive particles and compare how geometric shape affects the phase behavior of isotropic system. Ideally, the rotational noise, controlled by the gap height, should be consistent in all shapes of particles considered. Once we have studied the phase diagram of passive versions of these particles, we could further add activity to particles as we have done in this thesis with square shapes.

6.3 High Performance Simulation

Currently, all simulations are executed in a single core CPU. We could significantly improve the speed by parallelism using GPU. This work requires expertise in GPU calculation and high performance calculation. A good example and reference is the work by Anderson[39]. They provide an interface to work on passive hard particles.

BIBLIOGRAPHY

[1] M. C. Marchetti, J. F. Joanny, S. Ramaswamy, T. B. Liverpool, J. Prost, Madan Rao, and R. Aditi Simha. Hydrodynamics of soft active matter. *Rev. Mod. Phys.*, 85:1143–1189, Jul 2013.

[2] Julien Deseigne, Sébastien Léonard, Olivier Dauchot, and Hugues Chaté. Vibrated polar disks: spontaneous motion, binary collisions, and collective dynamics. *Soft Matter*, 8:5629–5639, 2012.

[3] Lee Walsh and Narayanan Menon. Ordering and dynamics of vibrated hard squares. *Journal of Statistical Mechanics: Theory and Experiment*, 2016(8):083302, aug 2016.

[4] Michael E. Cates and Julien Tailleur. Motility-induced phase separation. *Annual Review of Condensed Matter Physics*, 6(1):219–244, 2015.

[5] Clemens Bechinger, Roberto Di Leonardo, Hartmut Löwen, Charles Reichhardt, Giorgio Volpe, and Giovanni Volpe. Active particles in complex and crowded environments. *Rev. Mod. Phys.*, 88:045006, Nov 2016.

[6] Alison E. Patteson, Arvind Gopinath, and Paulo E. Arratia. Active colloids in complex fluids. *Current Opinion in Colloid Interface Science*, 21:86–96, 2016.

[7] Sriram Ramaswamy. Active matter. *Journal of Statistical Mechanics: Theory and Experiment*, 2017(5):054002, may 2017.

[8] Vijay Narayan, Sriram Ramaswamy, and Narayanan Menon. Long-lived giant number fluctuations in a swarming granular nematic. *Science*, 317(5834):105–108, 2007.

[9] Kun Zhao, Robijn Bruinsma, and Thomas G. Mason. Entropic crystal–crystal transitions of brownian squares. *Proceedings of the National Academy of Sciences*, 108(7):2684–2687, 2011.

[10] Walter F. Paxton, Kevin C. Kistler, Christine C. Olmeda, Ayusman Sen, Sarah K. St. Angelo, Yanyan Cao, Thomas E. Mallouk, Paul E. Lammert, and Vincent H. Crespi. Catalytic nanomotors: autonomous movement of striped nanorods. *Journal of the American Chemical Society*, 126(41):13424–13431, 2004. PMID: 15479099.

[11] R. Kemkemer, D. Kling, D. Kaufmann, and H. Gruler. Elastic properties of nematoid arrangements formed by amoeboid cells. *Eur. Phys. J. E*, 1(2), 2000.

[12] *Animal Groups in Three Dimensions: How Species Aggregate*. Cambridge University Press, 1997.

[13] Xavier Serra-Picamal, Vito Conte, Romaric Vincent, Ester Anon, Dhananjay T. Tambe, Elsa Bazellieres, James P. Butler, Jeffrey J. Fredberg, and Xavier Trepat. Mechanical waves during tissue expansion. *Nature Physics*, 8(8):628–634, August 2012.

[14] Arshad Kudrolli, Geoffroy Lumay, Dmitri Volfson, and Lev S. Tsimring. Swarming and swirling in self-propelled polar granular rods. *Phys. Rev. Lett.*, 100:058001, Feb 2008.

[15] Poul M. Bendix, Y Gijsje H. Koenderink, Z Damien Cuvelier, Zvonimir Dogic, Bernard N. Koeleman, William M. Brieher, K Christine M. Field, K L. Mahadevan, and David A. Weitz. A quantitative analysis of contractility in active cytoskeletal protein networks. *Biophys. J*, pages 3126–3136, 2008.

[16] Christopher Dombrowski, Luis Cisneros, Sunita Chatkaew, Raymond E. Goldstein, and John O. Kessler. Self-concentration and large-scale coherence in bacterial dynamics. *Phys. Rev. Lett.*, 93:098103, Aug 2004.

[17] Jérémie Palacci, Benjamin Abécassis, Cécile Cottin-Bizonne, Christophe Ybert, and Lydéric Bocquet. Colloidal motility and pattern formation under rectified diffusiophoresis. *Phys. Rev. Lett.*, 104:138302, Apr 2010.

[18] Lee Askew Walsh. *Vibrated Squares as Equilibrium and Active Matter*. PhD thesis, University of Massachusetts Amherst, 2018.

[19] Lee Walsh, Caleb G. Wagner, Sarah Schlossberg, Christopher Olson, Aparna Baskaran, and Narayanan Menon. Noise and diffusion of a vibrated self-propelled granular particle. *Soft Matter*, 13:8964–8968, 2017.

[20] John C. Crocker and David G. Grier. Methods of digital video microscopy for colloidal studies. *Journal of Colloid and Interface Science*, 179(1):298–310, 1996.

[21] Jon Louis Bentley. Multidimensional binary search trees used for associative searching. *Commun. ACM*, 18(9):509–517, sep 1975.

[22] Implementation of kdtree. `https://docs.scipy.org/doc/scipy/reference/generated/scipy.spatial.KDTree.html`. Post.

[23] Alex Krizhevsky, Ilya Sutskever, and Geoffrey E Hinton. Imagenet classification with deep convolutional neural networks. In F. Pereira, C. J. C. Burges, L. Bottou, and K. Q. Weinberger, editors, *Advances in Neural Information Processing Systems*, volume 25. Curran Associates, Inc., 2012.

[24] Compsci 682 neural networks: A modern introduction. `https://compsci682-fa20.github.io/notes/`. Lecture Note.

[25] P. Romanczuk, M. Bär, W. Ebeling, B. Lindner, and L. Schimansky-Geier. Active brownian particles. *The European Physical Journal Special Topics*, 202(1):1–162, 2012.

[26] Tamás Vicsek, András Czirók, Eshel Ben-Jacob, Inon Cohen, and Ofer Shochet. Novel type of phase transition in a system of self-driven particles. *Phys. Rev. Lett.*, 75:1226–1229, Aug 1995.

[27] M. Cristina Marchetti, Yaouen Fily, Silke Henkes, Adam Patch, and David Yllanes. Minimal model of active colloids highlights the role of mechanical interactions in controlling the emergent behavior of active matter. *Current Opinion in Colloid Interface Science*, 21:34–43, 2016.

[28] A. Deblais, T. Barois, T. Guerin, P. H. Delville, R. Vaudaine, J. S. Lintuvuori, J. F. Boudet, J. C. Baret, and H. Kellay. Boundaries control collective dynamics of inertial self-propelled robots. *Phys. Rev. Lett.*, 120:188002, May 2018.

[29] Bella Ilkanaiv, Daniel B. Kearns, Gil Ariel, and Avraham Be'er. Effect of cell aspect ratio on swarming bacteria. *Phys. Rev. Lett.*, 118:158002, Apr 2017.

[30] Christian Scholz and Thorsten Pöschel. Velocity distribution of a homogeneously driven two-dimensional granular gas. *Phys. Rev. Lett.*, 118:198003, May 2017.

[31] Julien Deseigne, Olivier Dauchot, and Hugues Chaté. Collective motion of vibrated polar disks. *Phys. Rev. Lett.*, 105:098001, Aug 2010.

[32] G. Briand and O. Dauchot. Crystallization of self-propelled hard discs. *Phys. Rev. Lett.*, 117:098004, Aug 2016.

[33] Krzysztof W Wojciechowski and Daan Frenkel. Tetratic phase in the planar hard square system. *Comput. Methods Sci. Technol*, 10(22):235–255, 2004.

[34] Carlos Avendaño and Fernando A. Escobedo. Phase behavior of rounded hard-squares. *Soft Matter*, 8:4675–4681, 2012.

[35] Vasileios Prymidis, Sela Samin, and Laura Filion. State behaviour and dynamics of self-propelled brownian squares: a simulation study. *Soft Matter*, 12:4309–4317, 2016.

[36] Thomas H. Cormen, Charles E. Leiserson, Ronald L. Rivest, and Clifford Stein. *Introduction to Algorithms, Third Edition*. The MIT Press, 3rd edition, 2009.

[37] Christer Ericson. Chapter 6 - bounding volume hierarchies. In Christer Ericson, editor, *Real-Time Collision Detection*, The Morgan Kaufmann Series in Interactive 3D Technology, pages 235–284. Morgan Kaufmann, San Francisco, 2005.

[38] Introductory guide to aabb tree collision detection. `https://www.azurefromthetrenches.com/introductory-guide-to-aabb-tree-collision-detection/`. Post.

[39] Joshua A. Anderson, M. Eric Irrgang, and Sharon C. Glotzer. Scalable metropolis monte carlo for simulation of hard shapes. *Computer Physics Communications*, 204:21–30, 2016.